

ENGINEERING HIGH PERFORMANCE INTERMEDIATE TEMPERATURE SOLID OXIDE
FUEL CELLS

By

JIN SOO AHN

A DISSERTATION PRESENTED TO THE GRADUATE SCHOOL
OF THE UNIVERSITY OF FLORIDA IN PARTIAL FULFILLMENT
OF THE REQUIREMENTS FOR THE DEGREE OF
DOCTOR OF PHILOSOPHY

UNIVERSITY OF FLORIDA

2009

© 2009 Jin Soo Ahn

To my loving wife, In Kyung

ACKNOWLEDGMENTS

I would like to thank my advisor, Professor Eric D. Wachsman, for giving me the opportunity, advice, and support for this work. His prudent guidance and deep understanding of electrochemistry and solid state ionics made the task of learning a new subject much easier. I am confident that I will draw on my experience under his guidance as I move forward. I am also grateful to other members of my supervisory committee, Dr. Juan Nino, Dr. Wolfgang M. Sigmund, Dr. Susan Sinnott, and Dr. Mark E. Orazem, for their time and thoughtful insight. I would like to thank Dr. Nino for inspiring my use of co-doped ceria systems, which consists of one chapter of this dissertation.

I gratefully acknowledge Dr. Heesung Yoon's kind help in setting up many of my experiments on electrochemical performance of solid oxide fuel cells. Without him, all the achievements and most results that I have made would have been impossible. I am grateful to Dr. Matthew Camaratta for the years of help and co-working alongside me. Also, I appreciate all the grammar corrections he has performed on my writing here at UF. I'd like to thank Dr. Jiho Yoo for kindly providing advice and counsel in research as well as in my personal life. It was also a great pleasure to work with Doh Won Jung, Dong Jo Oh, Kang Taek Lee, Matthew Barnett, Byung Wook Lee, Brian Blackburn, Dan Gostavic, Sean Bishop, Dr. Takkeun Oh, Eric Macam, Cynthia Kan, Eric Armstrong, Jianlin Lee and other group members. Their suggestions, cooperation, and comments were invaluable, and have helped me to improve my graduate research. I would also like to give a special thank you to Dr. Shobit Omar for his great help in the synthesis and characterization of a new material. Also, he provided many insightful discussions on the ceria systems. I appreciate Dr. Sejin Kim for his help setting up PLD deposition of ESB and Dr. Rajiv Singh for use of his PLD system. I thank Dr. Enrico Traversa and Dr. Daniele Pergolesi for their co-work on bilayered electrolytes. Their help enabled me to achieve an

extraordinary result in fuel cell performances. I would also acknowledge the Department of Defense (DOD) and Lynntech, Inc. for their funding (2007-NAV491-0001) of the projects I have been working on.

I thank my wife for years of support, love, and patience for bearing with me during my unexpectedly long study. Without her, studying for years would have been impossible. Finally, I would like to dedicate this dissertation to all my family members—my sister, father and mother. For years, they have supported my study. Without their unconditional sacrifice and endless love, I could have not achieved anything.

TABLE OF CONTENTS

	<u>page</u>
ACKNOWLEDGMENTS.....	4
LIST OF TABLES.....	9
LIST OF FIGURES	10
ABSTRACT	14
CHAPTER	
1 INTRODUCTION.....	16
1.1. Solid Oxide Fuel Cells.....	16
1.2. Anode Functional Layers	19
1.3. $\text{Sm}_{0.075}\text{Nd}_{0.075}\text{Ce}_{0.85}\text{O}_{2-\delta}$ as Alternative Electrolyte.....	22
1.4. ESB/GDC Bilayer Electrolytes for IT-SOFC	28
2 BACKGROUND.....	32
2.1. Fundamental Mechanisms of SOFC.....	32
2.2. Potential Losses of SOFC.....	34
2.2.1. Activation Polarization	36
2.2.2. Ohmic Polarization.....	37
2.2.3. Concentration Polarization	37
2.2.4. Internal Leakage Current	38
2.2.5. Combination of Each Polarization	39
3 EXPERIMENTAL PROCEDURES	41
3.1. SOFC Fabrication	41
3.1.1. Anode Tape casting.....	41
3.1.2. SNDC Electrolyte Deposition	41
3.1.3. GDC Electrolyte Deposition.....	43
3.1.4. LSCF Composite Cathode	43
3.1.5. AFL Deposition	44
3.2. Fabrication of ESB/GDC Bilayer Electrolytes	44
3.2.1. Co-pressing Procedure.....	45
3.2.2. Colloidal Route.....	46
3.2.3. Cold PLD	47
3.2.4. Hot PLD	49
3.3. Characterization	49

3.3.1. Microstructural Analysis.....	49
3.3.2. XRD	50
3.3.3. I-V Measurement.....	50
3.3.4. Impedance Spectroscopy	51
4 ANODE FUNCTIONAL LAYER FOR IT-SOFC	54
4.1. Homogeneous Functional Layers	54
4.1.1. Microstructural Analysis.....	54
4.1.2. Electrochemical Performance.....	58
4.2. Heterogeneous Functional Layers.....	66
4.2.1. Microstructural Analysis.....	66
4.2.2. Electrochemical Performance.....	67
5 CODOPED CERIA AS ALTERNATIVE ELECTROLYTES	73
5.1. XRD	73
5.2. Particle Size.....	73
5.3. Microstructural Analysis	75
5.4. Power Density	76
5.5. Impedance Analysis.....	78
6 ESB/GDC BILAYER ELECTROLYTE FOR IT-SOFC	81
6.1. Co-pressing Procedure.....	81
6.2. Colloidal Route	84
6.3. Cold PLD	88
6.4. Hot PLD.....	93
7 CONCLUSIONS	97
APPENDIX	
A STACK CELL APPLICATIONS	100
B Reproducibility and stability	106
1. Slow Progress toward High Performance.....	106
1.1 Electrolyte Particle Size Effect.....	107
1.2. Slurry Composition	109
1.3. Co-pressing	111
1.4. Spray Coating	113
1.5. Reproducibility	114
2. Future Work	115
2.1. Sealing and Leak	115
2.2. Long Term Stability	118
2.3. Critical Flaws.....	119

LIST OF REFERENCES 121
BIOGRAPHICAL SKETCH 126

LIST OF TABLES

<u>Table</u>		<u>page</u>
4-1	Details of No-AFL, Partial AFL and Full-AFL samples at 650 °C. The unit for ASR values is Ωcm^2	59
4-2	Summary of detailed ASR values 650 °C including Ni-GDC AFL and AFML sample.	69
5-1	Comparison between the total ASR obtained from I-V characteristic and impedance measurement.	80
6-1	Details of co-compressed cell.....	83
6-2	Details of tapecast cell without AFL.....	87
6-3	Details of tapecast cell with AFL.....	91
6-4	Summary of GDC single layer vs. ESB/GDC bilayer results.	96

LIST OF FIGURES

<u>Figure</u>	<u>page</u>
1-1 Schematic diagram of a SOFC with hydrogen fuel and oxygen.	16
1-2 SECA phase 1 requirement.....	18
1-3 Comparison of maximum power densities of thin film GDC of samaria doped ceria (SDC) electrolyte cells with various cathodes.	19
1-4 SOFC depending on operating temperatures.....	23
1-5 Ionic conductivities of various oxides including the conductivity values of GDC, SNDC and dysprosium and tungsten stabilized bismuth oxide (DWSB).....	25
1-6 Conductivity values of the ceria system with gadolinium single dopant and samarium and neodymium double dopant.	27
1-7 Bilayer electrolyte concept with relative thickness ratio to control interfacial oxygen partial pressure.	29
2-1 A typical current-voltage characteristics of a SOFC.	35
2-2 Separation of polarizations using a model developed by Yoon et al.	39
3-1 PLD system with KrF excimer laser.	48
3-2 Electrochemical measurement station.....	53
4-1 TEM images of raw powders of NiO (top) and GDC (bottom) used for tape casting of anode support.	54
4-2 Backscattered images showing change in anode surface porosity and roughness by GDC functional layer deposition.	56
4-3 SEM micrographs showing of the surface view of the GDC electrolyte deposited by spray coating on AFL coated anode.....	57
4-4 SEM micrograph showing the cross-sectional view of the SOFC with AFL after I-V testing.....	57
4-5 I-V characteristics of No-AFL, Partial-AFL and Full-AFL samples using 30 sccm of wet hydrogen and air at 650 °C.	58
4-6 The impedance spectra of No-AFL, Partial-AFL and Full-AFL samples at 650 °C under open circuit conditions.	60

4-7	I-V characteristics of Full-AFL sample at temperatures from 450 to 650 °C using 30 sccm of wet H ₂ and air.	61
4-8	The impedance spectra of Full-AFL sample at various temperatures under operating conditions.	62
4-9	The total, electrode and ohmic ASR values calculated from impedance spectra at temperatures from 450 to 650 °C.	63
4-10	The effect of the gas flow-rate on Partial-AFL sample at 650 °C.	64
4-11	The effect of gas flow rate and gas composition on the performance of Full-AFL sample at 650 °C.	65
4-12	Microstructure of Ni-GDC composite AFL on NiO-GDC anode.	66
4-13	The I-V curves for the sample with no AFL, GDC AFL and Ni-GDC AFL using 30 sccm wet hydrogen and dry air at 650 °C.	67
4-14	The impedance spectra under open circuit conditions at 650 °C.	68
4-15	Schematics for AFL structure for Multilayer approach.	69
4-16	I-V curves of the sample with Ni-GDC single layer AFL and multilayered AFL using 30 sccm wet hydrogen and dry air at 650 °C.	71
5-1	XRD pattern of Sm _{0.075} Nd _{0.075} Ce _{0.85} O _{2-δ} synthesized using co-precipitation technique.	73
5-2	Particle size distribution of Sm _{0.075} Nd _{0.075} Ce _{0.85} O _{2-δ} synthesized using co-precipitation technique and La _{0.6} Sr _{0.4} Co _{0.2} Fe _{0.8} O _{3-δ}	74
5-3	FE-SEM images of the cross-section view of the electrodes and electrolyte after operation.	75
5-4	FE-SEM image of the surface of the SNDC electrolyte after operation.	75
5-5	The I-V characteristics of the prototype SOFC sample with Sm _{0.075} Nd _{0.075} Ce _{0.85} O _{2-δ} electrolyte at various temperatures ranging from 500 to 650 °C in 90 sccm of both dry air and wet hydrogen.	77
5-6	Impedance spectrum of the SOFC cell measured at various temperatures ranging from 500 to 650 °C.	78
5-7	ASR values at various temperatures	79
6-1	Back scattered image showing the cross-section of the GDC (50 μm) and ESB (20 μm) bilayer electrolyte with BRO7-ESB composite cathode and Ni-GDC anode after cell testing.	81

6-2	I-V characteristics of three co-compressed samples at 650 °C using 30 sccm of wet hydrogen and dry air.	82
6-3	Backscatter image of the cross-section of the bilayer sample produced by colloidal deposition.	85
6-4	Backscatter images of bilayer samples showing the surface view of the ESB layer produced by colloidal deposition.	85
6-5	The I-V characteristics of the samples with GDC single layer and ESB/GDC bilayer electrolyte at 650 °C.	86
6-6	As-deposited ESB layer on the GDC electrolyte.	88
6-7	ESB layer after heat treatment at 700 °C for 4h. After heat treatment, the ESB wasn't fully densified.	88
6-8	Cross-section image of the cell with the ESB layer by cold PLD after heat treatment at 700 °C, 4h.	89
6-9	XRD patterns of bilayer samples depending on heat treatment conditions.	90
6-10	I-V characteristics of the samples with GDC single layer and ESB/GDC bilayer electrolyte at 650 °C using 90 sccm of air and wet hydrogen.	91
6-11	Impedance spectra of the samples with GDC single layer and ESB/GDC bilayer electrolyte at 650 °C using 90 sccm of air and wet hydrogen.	92
6-12	The bilayer microstructure with the ESB by Hot PLD.	93
6-13	XRD pattern of the bilayer sample.	93
6-14	I-V characteristics of the samples with GDC single layer and ESB/GDC bilayer electrolyte at 650 °C using 90 sccm of air and wet hydrogen.	94
6-15	Impedance spectra of the samples with GDC single layer and ESB/GDC bilayer electrolyte at 650 °C using 90 sccm of air and wet hydrogen.	95
A-1	SOFC Stack cell development in many countries.	100
A-2	Planar SOFC sample with 6 x 6 cm in size with possible active area of 30 cm ²	101
A-3	Microstructure of planar SOFC sample (a) surface view. (b) cross-section of GDC on NiO-GDC anode. (c) backscattered image of anode cross-section. (d) cross-section of the planar cell with brush painted LSCF-GDC composite cathode before test.	102
A-4	I-V characteristics (a) and impedance spectra(b) of a button cell taken from a large stack cell.	103

A-5	6 cm x 6cm SOFC planar cell with NiO-GDC anode, GDC electrolyte, GDC AFL, and 30 cm ² LSCF-GDC cathode.	103
B-1	I-V characteristics of the sample after 6 months of studying.	107
B-2	I-V characteristics of GDC powders from three different companies at 650 °C.	108
B-3	(a) SNDC synthesis by solid state route. (b) SNDC synthesis by co-precipitation route.	109
B-4	a) Surface of the GDC electrolyte. (b) Back-scattered cross-sectional image of the GDC electrolyte on NiO-GDC anode. (c) Surface of the GDC electrolyte with higher density. (d) Cross-sectional image of the GDC electrolyte with higher density.	110
B-5	A sample looking acceptable from visually inspection can have poor performance and porous microstructure.	111
B-6	I-V curves of the co-compressed sample at various temperatures using 90 sccm dry air and wet hydrogen.	112
B-7	(a) Change in the power density with increasing H ₂ flow-rate from 15 to 90 sccm with 30 sccm of air. (b) Change in the power density with increasing air flow-rate from 15 to 90 sccm with 30 sccm of H ₂	113
B-8	A custom made spray coating setup.	114
B-9	I-V curves from three consecutive three cells showing reproducibility of high performance at 650 °C.	115
B-10	Effect of ceramabond 1 (a) and ceramabond 2 (b) on the I-V characteristics.	117
B-11	Maximum power density of a SOFC without AFL for 700 hours at 550 °C.	118
B-12	(a) The OCP values and (b) the ASR values at 0.41 V for 700 hours.	118
B-13	Unusually porous region in the GDC electrolyte where other area is dense.	120

Abstract of Dissertation Presented to the Graduate School
of the University of Florida in Partial Fulfillment of the
Requirements for the Degree of Doctor of Philosophy

ENGINEERING HIGH PERFORMANCE INTERMEDIATE TEMPERATURE SOLID OXIDE
FUEL CELLS

By

Jin Soo Ahn

May 2009

Chair: Eric D. Wachsman

Major: Materials Science and Engineering

Solid oxide fuel cells (SOFCs) are an efficient, fuel flexible energy conversion device, capable of operating on fuels ranging from natural gas to gasoline, diesel, and biofuels, as well as hydrogen. However, to this point the marketability of SOFCs has been limited by their high operating temperatures. Achieving high power at intermediate temperatures (IT, 500 – 700 °C) would be a significant breakthrough, as low temperature operation would result in better stability and allow for a broader range of material options for the SOFC components as well as the balance of plant, such as stainless steel interconnects (which are only viable at <700 °C). Thus far, power densities on the order of 2 W/cm² have been limited to temperatures above 800 °C. This dissertation contains a series of works to realize exceptionally high power at IT ranges. First, improved fabrication techniques including anode tapecasting and electrolyte spray coating were developed, and a molecular approach to anode functional layer (AFL) was employed using precursor solutions. This newly developed AFL reduced the ASR of a SOFC sample by 60 % and increased the open circuit potential (OCP) by more than 0.1 V resulting in a 140 % increase in power. Further investigations into this molecular AFL showed that a multilayered AFL can further reduce the ASR and increase the maximum power density. Secondly, the potential use of Sm_{0.075}Nd_{0.075}Ce_{0.85}O_{2-δ} as an electrolyte has been investigated. The current-voltage (I-V)

performance of the cell exhibits a maximum power density reaching 1.38 W/cm^2 with an area specific resistance (ASR) of $0.087 \text{ } \Omega\text{cm}^2$ at $650 \text{ }^\circ\text{C}$ with 90 sccm of air and wet hydrogen. Also, the high OCP achieved at $500 \text{ }^\circ\text{C}$ (0.96 V) as well as the high performance confirmed the viability of $\text{Sm}_{0.075}\text{Nd}_{0.075}\text{Ce}_{0.85}\text{O}_{2-\delta}$ as an alternative electrolyte material. The cathode used for this study was $\text{La}_{0.6}\text{Sr}_{0.4}\text{Co}_{0.2}\text{Fe}_{0.8}\text{O}_3$ (LSCF) – $\text{Gd}_{0.1}\text{Ce}_{0.9}\text{O}_2$ (GDC) composite. Finally, $\text{Er}_{0.8}\text{Bi}_{1.2}\text{O}_3$ (ESB) / GDC bilayered electrolyte combined with recently developed ESB / $\text{Bi}_2\text{Ru}_2\text{O}_7$ (BRO) composite cathodes was tested. In this work a maximum power density of 2 W/cm^2 was achieved at $650 \text{ }^\circ\text{C}$ with the help of the novel AFL and tapecast anode supports. This is the highest power yet achieved in the IT range and I believe redefines the expectation level for maximum power under IT-SOFC operating conditions.

CHAPTER 1 INTRODUCTION

1.1. Solid Oxide Fuel Cells

Due to a variety of factors including heavily fluctuating energy costs and environmental concerns, next generation energy sources require a reduced reliance on simple combustion of fossil fuels. Greenhouse emissions from automobiles and power plants have long been believed of contributing to global climate change.¹ Particulate matter exhausted from buses and larger vehicles can penetrate into the lungs, causing respiratory and cardiac disease.² There has been a longstanding need to reduce the polluting byproducts of conventional energy generation. There is an expanding list of reasons to explore alternatives to conventional energy generation methods. SOFCs are expected to play a significant role in the future of energy technology. Development of SOFC technology is a major step towards reaching the goal of sustainable energy production. Due to its potential for high efficiency it not only conserves valuable natural resources but also assists in reducing pollution and greenhouse gas emissions.

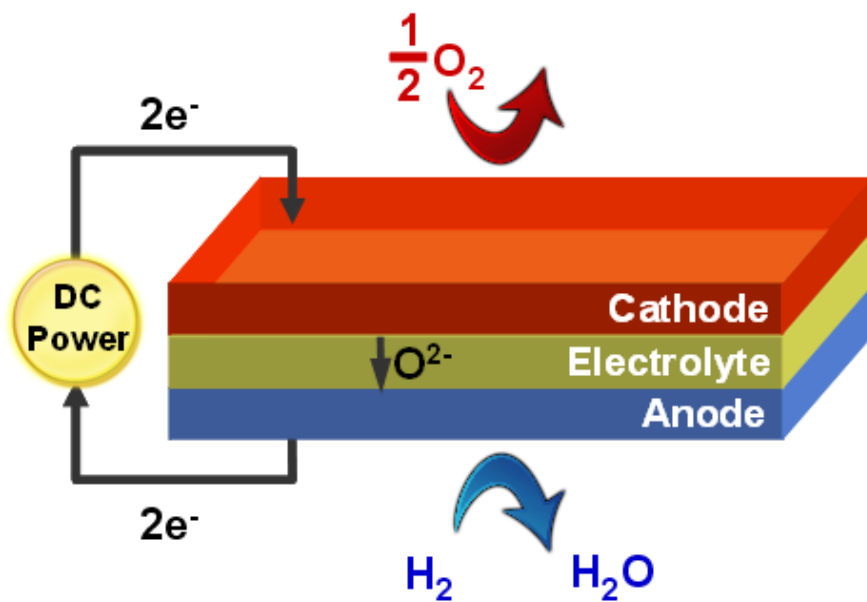


Figure 1-1. Schematic diagram of a SOFC with hydrogen fuel and oxygen.

A SOFC is a device that converts chemical energy to electrical energy at elevated temperature. The need for direct combustion is eliminated, giving fuel cells much higher conversion efficiencies than conventional thermo-mechanical methods. The main difference between SOFCs and other fuel cells, such as alkaline fuel cell (AFC), polymer electrolyte membrane fuel cell (PEMFC), phosphoric acid fuel cell (PAFC) and molten carbonate fuel cell (MCFC) is the material used for the electrolyte, and consequently the operating temperature ranges and thus plausible market applications. Due to the use of solid oxide electrolytes, higher operating temperatures are required for SOFCs than any other type of fuel cell. Since the SOFC concept was first introduced, much research has been conducted to realize stable and efficient SOFCs suitable for replacement of current energy generation technologies.

Generally SOFCs consists of three main parts: anode, electrolyte and cathode (Figure 1-1). The anode is where the oxidation of hydrogen ($2\text{H}_2 \rightarrow 4\text{H}^+ + 4\text{e}^-$) (or other fuels) occurs, and the cathode is where the reduction of oxygen ($2\text{O}^{2-} + 4\text{e}^- \rightarrow \text{O}_2$) takes place. Electrons provided from the anode move to cathode through the outer electrical circuit. The electrolyte is the component where oxygen ionic conduction takes place, and separates the cathode and the anode from electronic contact. Though most SOFCs currently use hydrogen as fuel,³ SOFCs can utilize deferent reactions depending on different fuels. Example reactions are the following:

- $2\text{O}^{2-} (\text{ion}) + \text{H}_2 (\text{gas}) \rightarrow 2\text{H}_2\text{O} + 4\text{e}^- (\text{electron})$
- $\text{CH}_4 (\text{gas}) + \text{O}^{2-} (\text{ion}) \rightarrow \text{CO}(\text{gas}) + 2\text{H}_2(\text{gas}) + 2\text{e}^- (\text{electron})$
- $\text{CH}_4 (\text{gas}) + 4\text{O}^{2-} (\text{ion}) \rightarrow \text{CO}_2(\text{gas}) + 2\text{H}_2\text{O}(\text{gas}) + 8\text{e}^- (\text{electron})$

Figure 1-2 shows the Solid State Energy Conversion Alliance (SECA) phase 1 requirement for SOFC operations. To fulfill the SECA requirement of 3 kW power output, highly efficient SOFC performance is needed.⁴ A simple calculation shows that 10000 cm² of active area with a power density of 0.3 W/cm² would be required to attain this power, which is considered

relatively high performance these days. This huge active area requires increased number of stacked SOFC panels, interconnectors and sealant materials, and this will subsequently increase the cost and undermine the viability of SOFC application. So, realizing highly efficient SOFC is one of the key technological issues in the SOFC field.

PARAMETER	PHASE I REQUIREMENTS
POWER RATING (net)	3Kw - 10 kW
COST	\$800/kW
EFFICIENCY (AC or DC/LHV)	Stationary-35%
STEADY STATE TEST @ NORMAL OPERATING CONDITIONS	1500 hrs 80% availability Delta Power = 2% degradation/500 hrs at a constant stack V with R >= 0.95
TRANSIENT TEST	10 cycles Delta Power = 1% degradation after 10 cycles at a constant stack voltage
TEST SEQUENCE	1) Steady state 1000 hours 2) Transient test 3) Steady state 500 hours
FUEL TYPE	Operate the prototype on either a commercial commodity, or a representative fuel. Utilize external or internal primary fuel reformation or oxidation
MAINTENANCE INTERVAL	> 1000 hours
DESIGN LIFETIME	Not less than 40,000 operating hours for stationary applications

Figure 1-2. SECA phase 1 requirement.⁴

It has been demonstrated that the combination of an yttria stabilized zirconia (YSZ) electrolyte and a $\text{La}_{0.8}\text{Sr}_{0.2}\text{Mn}_1\text{O}_3$ (LSM) cathode can generate a power density approaching 2 W/cm^2 above 800 °C.⁵ Achieving comparable power densities at the IT range (500 – 700 °C), where lower cost, better stability and broad materials choice, such as stainless steel interconnects are possible, would be a significant breakthrough for SOFCs. The benefits of IT operation will be discussed in depth in the following section. Combining a GDC electrolyte and LSCF cathode offers operation temperatures below 700 °C (Figure 1-3),⁶ but does not guarantee a high power output. A recently developed next generation cathode, $\text{Ba}_{0.5}\text{Sr}_{0.5}\text{Co}_{0.8}\text{Fe}_{0.2}\text{O}_3$ (BSCF), produced a power density of 1 W/cm^2 at IT ranges.^{6,7} However, thus far a power density of 2 W/cm^2 has been limited only to temperatures above 800 °C.⁵

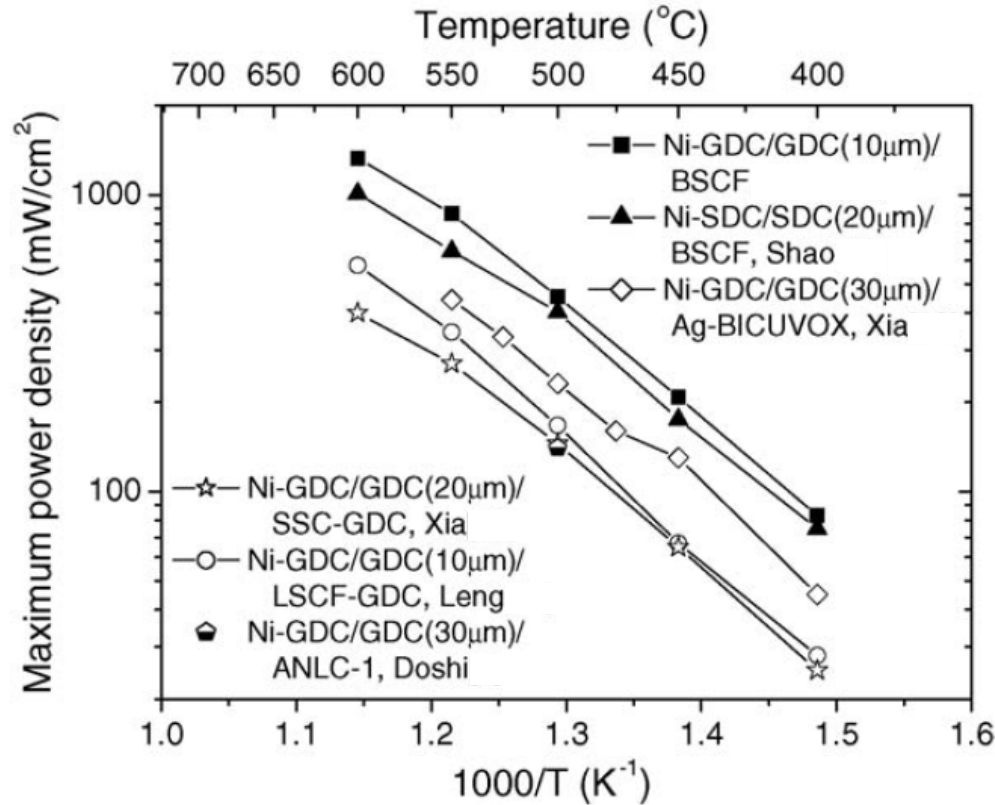


Figure 1-3. Comparison of maximum power densities of thin film GDC of samaria doped ceria (SDC) electrolyte cells with various cathodes.⁶

1.2. Anode Functional Layers

The need for higher efficiency and stability in SOFC performance changes simple cathode, electrolyte and anode layers into multilayered structures with functional gradients. An example of this is the ESB/GDC bilayer electrolyte where the ESB layer helps to increase cell OCP and improve ionic conductivity, while the GDC layer protects ESB from reducing atmospheres.⁸ Also, a GDC/YSZ bilayer electrolyte allows for use of LSCF cathodes as GDC as a protective layer between YSZ and Co from the cathode.⁹ The multiple functions of each SOFC compartment, a cathode, electrolyte and anode, can be shared by multilayers specializing in a designated function. These relatively new approaches allowed for high performance or better stability in SOFCs.¹⁰ It is likely that the future fuel cell will unlikely be a simple stack of three component layers—the cathode, electrolyte and anode.

One of the most important applications of these multilayer or interlayer approaches in SOFC field is the anode functional layer (AFL, sometimes called the anode inter layer).¹¹⁻¹³ Overall SOFC performance depends on the particle size of anode cermet because particle size dictates the porosity and the TPB length. Most SOFC electrode reactions take place at triple phase boundaries (TPB) between the gas phase, an electronic conducting phase, and an ionic conducting phase. Increasing the TPB length increases the number of active reaction sites and therefore enhances the performance of SOFCs. Deposited on an electrolyte of a given surface area, electrodes composed of smaller particles result in larger TPB lengths. Therefore, it is clear that use of smaller particles for the electrode will result in better SOFC performance. However, while smaller particles produce higher TPB lengths, they tend to increase density. It is difficult for a dense anode to provide fuel rapidly to the reaction sites and to remove water molecules efficiently.

Frequently sub micron-sized anode powder is mixed with pore former for the fabrication of anode supported SOFCs. To achieve a sufficient amount of gas channels, an extensive volume fraction of pore former is required. However, it has been reported that pore former additions result in porous anode surfaces and subsequently induces poor quality of the electrolyte deposited by colloidal methods.¹⁴ Also, large pores on the anode surface result in poor contact between the electrolyte and the anode.¹⁴

One approach to achieve both high open porosity and large TPB length is to deposit a thin anode interlayer using fine powders on an anode made of coarse particles¹⁵ prior to deposition of the electrolyte. In this configuration the anode can successfully satisfy the two distinctive roles of an anode: gas transport and electrochemical oxidation of hydrogen. Because an AFL removes abrupt change at the anode/electrolyte interface, it allows for gradual changes in properties such

as thermal expansion coefficient and interfacial resistance. Additionally the AFL reduces surface roughness, thus improving the quality of the electrolyte film deposited by colloidal methods.

Recently our study on IT-SOFCs has focused on fabrication of planar cells by colloidal deposition of the GDC electrolyte on tape cast Ni-GDC anodes without addition of pore formers. In order to fabricate stacked, large diameter planar SOFCs with doped ceria electrolytes, it is crucial to prepare a dense and thin ceria electrolyte layer on the anode. Tape casting is widely used for planar and multi-stacked ceramic devices because it is a reproducible and efficient ceramic fabrication process. Planar SOFCs have attractive geometries for simple stacking integration. Tape casting of anode supports combined with colloidal deposition of electrolytes is cost-effective and suitable for mass production.

To achieve sufficient anode porosity, the anodes were tape cast with large micron-sized NiO powder mixed with small sub micron-sized GDC powder. The images of NiO and GDC powder used for tapecasting were taken by TEM and present in Figure 4-1. Though sufficient porosity can be achieved by this method, greater anode polarization loss is expected due to the use of large NiO particles. The anode polarization can be reduced by applying an AFL on the anode surface. In this dissertation we propose a method to disperse a very fine anode functional layer at the interface of the GDC electrolyte and Ni-GDC anode tape using a GDC precursor solution. To the best of my knowledge, all AFL studies done so far have been limited to colloidal deposition of fine powder of the same composition as the anode bulk.^{12,13,16} Compared to the conventional AFLs, which utilize colloidal slurry, the precursor solution is advantageous in many ways. Deposition of an AFL with a precursor solution is based on the following assumptions. First, it is easier to form smaller particles at the interface using precursor solution.

Secondly, penetration depths of precursor solutions are deeper than that of colloidal slurries. The greater penetration depth of AFL expands TPB length and provides a better adhesion between the anode and the electrolyte. Additionally, it is easier to stabilize the solution as well as spray it onto the anode.

The effects of the AFL from GDC precursor on the electrochemical performance are presented in this dissertation. The effect of gas flow rate on the performance of the fuel cell is also presented. Also, further investigation on the composition effect of the molecular AFL by co-spraying Ni and GDC precursors were performed. It is well known that the Ni-GDC composite can extend the TPB length. Therefore, I believe the ideal composition of AFL should include Ni.

A component such as the anode, which has two main functions, is not necessarily limited to two layers. Holtappels et al.,¹⁷ demonstrated an anode with four distinct layers with gradually changing porosity. A series of experimental and modeling work on recently-developed functionally gradient electrodes (FGE),¹⁸⁻²² have demonstrated higher performance or better stability using porosity, particle size, or composition gradients. Also, Ni et al., demonstrated by modeling that composition gradient of the anode can expand TPB length and provide better stability due to removal of abrupt change at the interface.²¹ This dissertation demonstrates how to further improve these molecular approach AFLs by layer by layer approach. LSCF-GDC composites cathodes were used for this study.

1.3. $\text{Sm}_{0.075}\text{Nd}_{0.075}\text{Ce}_{0.85}\text{O}_{2-\delta}$ as Alternative Electrolyte

The long-term performance degradation as well as the high cost associated with high operating temperature (800 ~ 1000 °C) have been substantial obstacles to the widespread commercialization of SOFC technology.²³ Reducing cell operating temperatures to the IT range will extend its application domain to residential power and portable devices. However, with

current state-of-the-art SOFC materials, it is not possible to obtain sufficient power in the IT range. This is due to high ohmic losses and electrode polarization, which have a detrimental effect on device performance and efficiency. Thus, there is a need to develop materials that show improved properties in the IT range.



Figure 1-4. SOFC depending on operating temperatures. Automobile APU application (300 – 500 °C), Delphi. Residential power (500-650 °C). Stationary (800-1000 °C), Siemens-Westinghouse.

Due to the high operating temperature of SOFCs, they have been viewed primarily for stationary applications. However, the ability of SOFCs to run on gaseous and liquid hydrocarbons such as gasoline, diesel, and natural gas suggests great opportunity for use in portable energy source applications particularly for the automotive industry, given that the production, delivery and storage infrastructure of these fuels is already established. Figure 1-4 shows various applications for which a SOFC can be used depending on operating temperatures. For localized power plants, IT-SOFCs are more advantageous than high temperature SOFCs.²⁴

The leading candidate for automotive fuel cells is the polymer electrolyte membrane fuel cell (PEMFC) due to its low operating temperature (80 ~ 120°C). However a PEMFC requires extremely pure hydrogen fuel.²⁵ So, for example, in order to utilize hydrocarbon fuels for a car equipped with a stack of PEMFCs an autothermal/steam reformer, a high temperature shift reactor, a low temperature shift reactor, and a preferential oxidation system would be required in order to produce pure hydrogen from these largely carbon-based fuels.²⁶ By contrast, SOFCs can

directly utilize hydrocarbon fuels without additional devices to pre-process fuels. Fewer parts mean greater efficiency, lower costs and a smaller overall package.²⁶

There is one major drawback of SOFCs that has hurt their viability in this market—their high operating temperatures. This requires extended startup times—a period of fuel burning which is needed to reach these operating temperatures. High operating temperatures are also responsible for sealing problems and expensive interconnect and balance-of-plant materials for SOFC stacks. Additionally, high temperature operation can induce thermal stresses at electrolyte-electrode interfaces, as well as cause inter-diffusion between cell components. Most of these problems will be solved if the operating temperature can be lowered to around 500 °C.

The major benefits of IT-SOFCs are listed below:

- Low heat – low cost.
- Low thermo-mechanical stress in assembly resulting in longer service life.
- Performance stability due to reduced degradation of electrodes and electrolytes
- Increased range of materials that can be used including sealants.
- Fast start-up time

At these reduced temperatures, conventional SOFCs using YSZ electrolytes have very high ohmic polarization. Using an oxide with higher conductivity can reduce the ohmic polarization. One such electrolyte material is the doped ceria system, which has higher ionic conductivity than doped zirconia. Utilization of doped ceria electrolytes with thicknesses below 15 μm has significantly reduced ohmic polarization losses at temperatures between 500 °C and 600 °C.²⁷

According to Figure 1-5, GDC and ESB are the leading candidates for electrolyte materials at the IT ranges.²⁷ Higher conductivity of the electrolyte produces low ohmic polarization, and it can be understood by a simple equation;

$$\eta_{ohm.} = i * ASR = i * \rho * T_{Thickness} = (i / \sigma) * T_{Thickness} \quad (1-1)$$

where η , i , ASR, ρ , σ and $T_{\text{thickness}}$ correspond to the ohmic overpotential, current density, area specific resistance, resistivity, conductivity, and electrolyte thickness, respectively. In the equation above, the ohmic overpotential is inversely proportional to the conductivity.

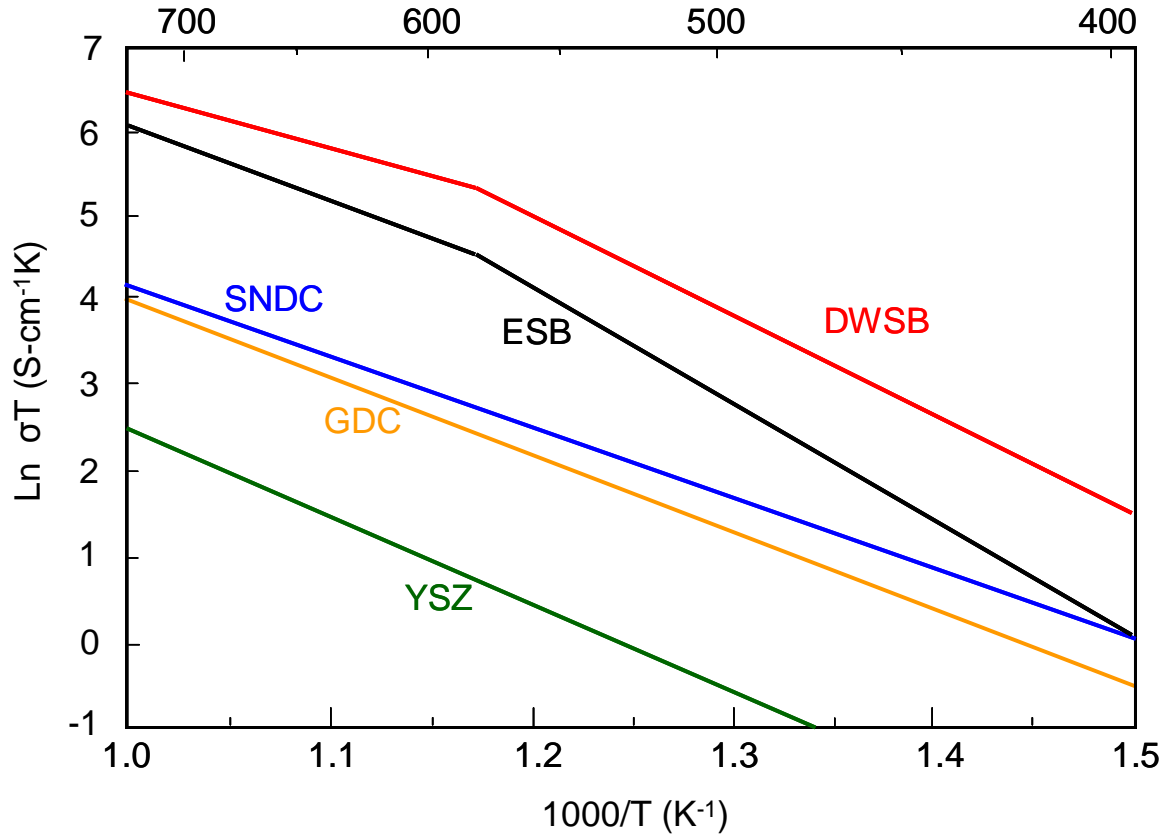


Figure 1-5. Ionic conductivities of various oxides including the conductivity values of YSZ,²⁷ GDC,²⁸ SNDC²⁹ and dysprosium and tungsten stabilized bismuth oxide (DWSB).²⁸

There is one other important advantage of using faster ionic conductors specifically when using hydrocarbon fuels. Faster ionic conductors can provide larger amounts of oxygen from the cathode to the anode reaction sites. This is an important aspect for the oxidation of heavy hydrocarbon fuels or liquid alcohol fuels as larger amount of oxygen can reduce coke formation. According to Wagner's theory, increased ionic conductivity increases oxygen flux.³⁰

$$j(O_2) = -\frac{RT}{16F^2d} \int_{\ln P_{O_2}'}^{\ln P_{O_2}''} \frac{\sigma_{el}\sigma_{ion}}{\sigma_{el} + \sigma_{ion}} d \ln P_{O_2} \quad (1-2)$$

where R is the gas constant, F is Faraday's constant, d is the electrolyte thickness, σ_{el} is electronic conductivity and σ_{ion} is ionic conductivity.

The use of faster an ionic conductor such as GDC in the composite anode and cathode is also beneficial. As will be discussed in Chapter 6, a cathode containing a faster ionic conductor exhibits smaller ASR compared to a similar cathode containing a slower ionic conductor.³¹ To date, the simple oxygen reduction reaction on a pure Pt cathode is not fully understood.³² This is true of fuel oxidation on the anode as well. One of the main obstacles of anode research is that the mechanism of fuel oxidation at the anode even for simple hydrogen fuel and conventional cermet anodes is not understood yet.³ The anode reaction is even less understood than the cathode reaction because of the higher level complexity (involving removal of the water by-product and mixed conductivity of certain ionic conductors in reducing atmosphere). The mechanistic complexity will dramatically increase for methane and heavier hydrocarbons. One of the most significant mechanistic studies on the anode was conducted by Mogensen, work but the model could not incorporate the fact that GDC can have electronic conductivity at reducing conditions and hence, reaction sites can exist at the GDC surface, and failed to explain the reported properties of the anode.³³

However, a simpler model exists relating the electrode polarization to the ionic conductivity of the ceramic phase of the electrode. Theoretical background and predictions in cathode design can be found in practical models developed for composite cathodes. Equation 1-3 is a simple model developed for the cathode that has both electronic and ionic conducting phases³⁴ and proved useful for electrode design.³⁵

$$R_i = \sqrt{\rho r k / 2} \coth \sqrt{2 t^2 \rho / k r} \quad (1-3)$$

where R_i is the cathode resistance, t is the electrode thickness, r is the ionic resistivity of the ionic conducting phase, k is an intrinsic interfacial resistance characteristic of the interfaces between the ionically and electronically conducting phases, and r is the pore radius. According to this model the interfacial resistance of the cathode and the anode with YSZ as an ionic conductor can be suppressed by replacing YSZ with GDC, which is a faster ionic conductor. The reduction in cathode polarization by replacing GDC with ESB will be discussed in Chapter 6.

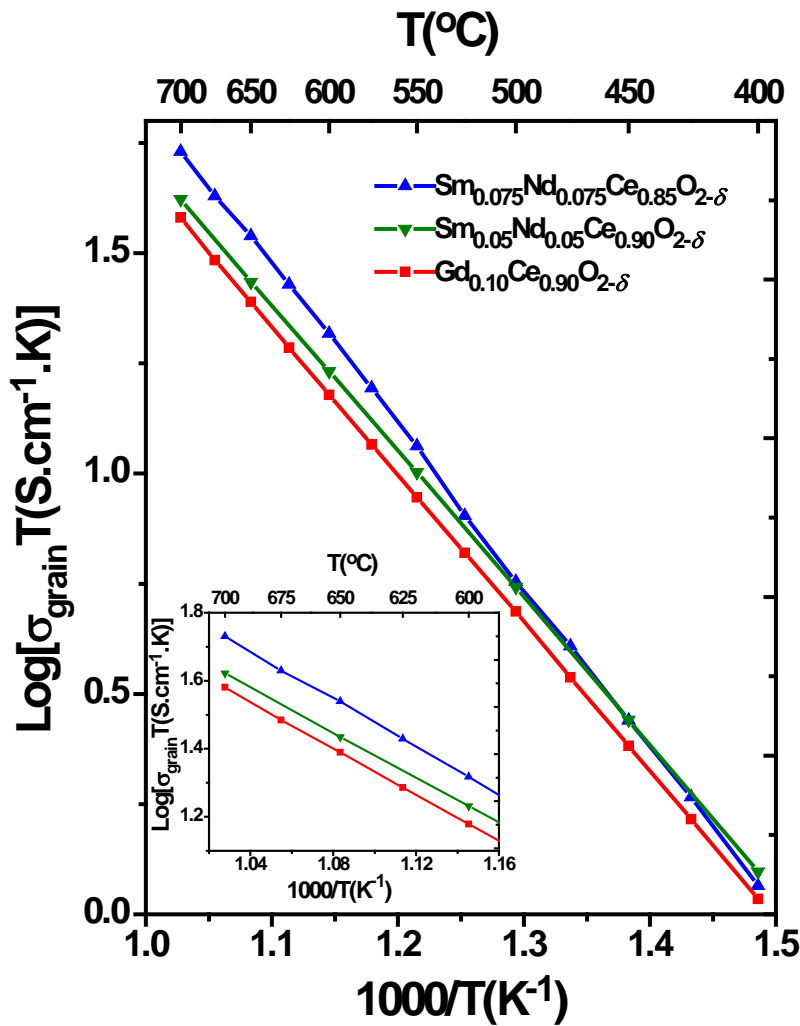


Figure 1-6. Conductivity values of the ceria system with gadolinium single dopant and samarium and neodymium double dopant.^{29,36}

Electrolytes with high ionic conductivity are critical for the development of SOFCs that can successfully generate reasonable power at IT range.³⁷ In recent years, doped ceria electrolytes have emerged as a potential electrolyte candidate material due to its high ionic conductivity.^{23,29} Among doped ceria materials, $Gd_{0.1}Ce_{0.9}O_{2-\delta}$ was widely accepted to exhibit the highest ionic conductivity.³⁶ However, Omar et al., have shown that co-doping based on Sm^{3+} and Nd^{3+} leads to further enhancement in the ionic conductivity in ceria systems.²⁹ Optimization of dopant concentration in $Sm_{x/2}Nd_{x/2}Ce_{1-x}O_{2-\delta}$ system resulted in the development of $Sm_{0.075}Nd_{0.075}Ce_{0.85}O_{2-\delta}$ which exhibits 30 % higher grain ionic conductivity than that of GDC at 550 °C in air (Figure 1-6). In the present work, the potential of $Sm_{0.075}Nd_{0.075}Ce_{0.85}O_{2-\delta}$ as an alternative electrolyte is further investigated by testing its performance in a SOFC. An anode-supported SOFC was fabricated, with $Sm_{0.075}Nd_{0.075}Ce_{0.85}O_{2-\delta}$ as the electrolyte. At this point, the effect of incorporating $Sm_{0.075}Nd_{0.075}Ce_{0.85}O_{2-\delta}$ into the anode and cathode will be relegated as future work. The performance of these SOFCs at IT is discussed in Chapter 5.

1.4. ESB/GDC Bilayer Electrolytes for IT-SOFC

Operating temperatures can be lowered by reducing the resistance of each cell component: the anode, the cathode, and the electrolyte. Reduced electrolyte resistance has been a topic of enduring study in the SOFC field. One method for reducing electrolyte resistance is to replace the conventional yttria-stabilized zirconia (YSZ) electrolyte with materials exhibiting higher ionic conductivity. Two of the leading candidates are gadolinia doped ceria (GDC) and erbium-stabilized bismuth oxide (ESB). Based on reported conductivity values, 10 μm thick electrolytes of YSZ, GDC and ESB have area specific resistances (ASR) of 1.259, 0.143 and 0.037 Ωcm^2 , respectively, at 500 °C,²⁸ that is, an order of magnitude drop in electrolyte ASR can be achieved by changing from YSZ to GDC and from GDC to ESB.

However, these new materials do have drawbacks. For ceria-based electrolytes, the reduction of Ce^{4+} cations into Ce^{3+} allows for electronic conduction via a small polaron hopping mechanism yielding a narrow electrolytic domain.³⁸ Thus, under reducing conditions (such as that found at the SOFC anode, $P_{O_2} \sim 10^{-26}$), GDC will exhibit a degree of electronic conduction, which is negligible below 500 °C, though.³⁹ This electronic conduction reduces the cell's ionic transference number and hence its Nernstian potential and maximum power output. Second, for ESB the weak metal-oxygen bonds, which make it one of the fastest ionic conductors known, ironically also lead to reduced thermodynamic stability at low P_{O_2} .⁴⁰

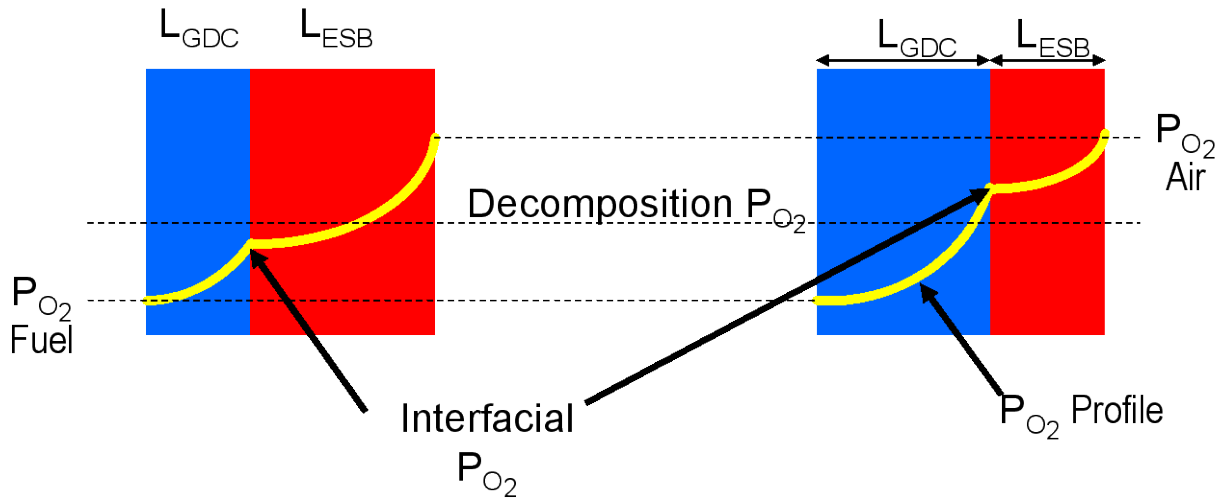


Figure 1-7. Bilayer electrolyte concept with relative thickness ratio to control interfacial oxygen partial pressure (P_{O_2}).^{40,41}

These issues can be resolved by utilizing a bilayer electrolyte with GDC on the fuel side and ESB on the air side. In this configuration, the ESB layer will block electronic conduction from the GDC layer, and a sufficiently thick GDC layer would prevent decomposition of ESB. The interfacial P_{O_2} can then be controlled by varying the thickness ratio of the component layers (Figure 1-7).

Previously it has been demonstrated that the OCP can be increased with a bilayer electrolyte over a wide range of temperatures, and that it has good long term stability.^{8,41,42} It should be noted that the increase in OCP is a function of the ESB layer density and thickness.^{41,42} Fabrication of a thin and dense ESB and GDC layers is key for increasing OCP.

In addition to increasing cell OCP, the bilayer electrolyte can reduce the effective total electrolyte ASR. By modeling the bilayer electrolyte as two resistors in series, electrolyte ASR can be described as equation (1-4), where τ is the thickness ratio of ESB to GDC and σ_i is the ionic conductivity of each material. Park et al., demonstrated that the ASR can be decreased by utilizing a bilayer electrolyte.⁴³

$$ASR_{Electrolyte} = L_{GDC} * \left(\frac{\tau}{\sigma_{ESB}} + \frac{1}{\sigma_{GDC}} \right) \quad (1-4)$$

An additional advantage of having an ESB layer on the air side of the cell is that, as frequently reported, the surface of bismuth oxide-based electrolytes is active for the adsorption of oxygen species. It is believed that bismuth strongly enhances the surface oxygen exchange rate.⁴⁴⁻⁴⁶ This is evidenced by the factor of 10^3 larger surface oxygen exchange rate for bismuth oxide based solids compared to YSZ solids. In addition, bismuth-based electrolytes have been reported to be catalytically active towards oxygen dissociation and charge transfer.^{47,48} It is thus possible that the use of ESB at the cathode/electrolyte interface may result in reduced cathode activation overpotentials. This phenomenon is discussed further in chapter 6.

However, because of their weak metal-oxide bonds, bismuth oxide based electrolytes are highly reactive towards many conventional cathode systems. Recently, some composite systems which are chemically compatible with bismuth oxide based electrolytes have been developed. Ag-bismuth oxide show significantly lower values of ASR compared with other frequently studied cathode systems such as LSCF-GDC, and have been modified to show relatively good

long-term performance.^{49,50} Even lower ASR values were achieved from microstructurally optimized composites of Bi₂Ru₂O₇ (BRO7) and ESB.^{51,52}

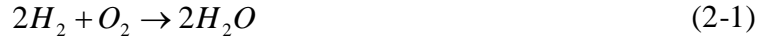
While the bilayer electrolyte concept has proven sound, bilayer cells exhibiting high performance have not been reported to this point. The previous results with ~ 800 μm thick ESB/samaria doped ceria (SDC) electrolyte, Pt anode and Au cathode achieved a higher OCP and lower ASR resulting in a 33% increase in power density over a single layer SDC electrolyte under the same conditions.⁴¹ However, the power density achieved was only 50 mW/cm² at 800 °C. Similarly, Leng et al., fabricated SOFCs utilizing yttria-stabilized bismuth oxide (YSB) / GDC bilayer electrolytes with total thicknesses above ~ 800 μm and Pt electrodes.⁵³ Their bilayer study also demonstrated higher OCP and power density than with a single layer GDC electrolyte, but the power density did not exceed 20 mW/cm² at 600 °C. The poor performance is due in part to the difficulty in depositing thin and dense ESB layers. In addition, low-resistance ESB-compatible cathodes have only recently been developed.

The SOFCs utilizing single layer GDC electrolytes have made much progress toward achieving high power densities.^{54,55} This dissertation demonstrates that a bilayer ESB/GDC electrolyte can achieve exceptionally high power densities when combined with high performance GDC electrolytes as well as recently-developed BRO7-ESB composite cathodes. Various fabrications were employed for deposition of dense ESB including pulsed laser deposition (PLD).

CHAPTER 2 BACKGROUND

2.1. Fundamental Mechanisms of SOFC

The simplest way of conceptualizing an SOFC operating with hydrogen and oxygen is that the cell burns hydrogen and converts the energy generated from this process into useful work.



The main difference between a SOFC and a conventional combustion engines is that in SOFCs, hydrogen molecules are burned by electrochemical oxidation reactions. So, instead of generating heat, a SOFC generates electrical energy. The benefit of electrochemical oxidation of fuel is that the efficiency in energy conversion is not limited by the Carnot efficiency limit where there is a heat loss.⁵⁶

When an SOFC is at equilibrium, in other words at zero current, its potential is called open circuit potential (OCP). The OCP can be determined by Nernst potential (E).

$$OCP = t_i \times E \quad (2-2)$$

where, t_i is the transference number for ionic conduction. The following is a derivation of Nernstian potential relevant for SOFC systems.

$$\Delta G = \Delta G^\circ - RT \ln K_e \quad (2-3)$$

where G is Gibbs free energy, G° is Gibbs free energy at standard state, R is the gas constant, T is the absolute temperature and K_e is equilibrium constant. Since,

$$\Delta G = -nFE \quad (2-4)$$

where n is number of electrons per mole of oxygen molecules, F is Faraday's constant and E is potential, the potential of the cell can be described by,

$$E = E^\circ + \frac{RT}{4F} \ln \left(\frac{P_{O_2}^{cathode}}{P_{O_2}^{anode}} \right) \quad (2-5)$$

Here, ΔG° or E° should be regarded as zero for SOFC reactions since the driving force for a SOFC is the chemical potential difference of oxygen molecules across the electrolyte. At standard state, chemical potential of oxygen molecules at the cathode and anode can be treated as unity. So, the potential of the SOFC is now,

$$E = \frac{RT}{4F} \ln \left(\frac{P_{O_2}^{cathode}}{P_{O_2}^{anode}} \right) \quad (2-6)$$

Equation (2-6) shows that the potential is a function of temperature and chemical potential (partial pressure difference) of oxygen molecules. Using this equation one can easily calculate the theoretical potential. The following is a calculation of the theoretical potential of a SOFC operating at 650 °C with the anode partial pressure of oxygen set by a bubbler at room temperature. When H_2O_{liq} and H_2O_{vap} is at equilibrium,⁵⁷

$$\log P_{H_2O} = \frac{-2900}{T} - 4.65 \times \log T + 19.732 \quad (2-7)$$

According to this equation, at room temperature, a bubbler is sending humidified hydrogen gas to the anode with $P_{H_2O} = 0.03$ and we can assume that P_{H_2} is close to 1 for simplicity of the calculation since P_{O_2} is negligible. The P_{O_2} can then be calculated using the equilibrium constant and the Gibbs free energy of a water forming reaction. The water forming reaction used for this calculation, the equilibrium constant for the reaction, and the Gibbs free energy in terms of temperature are as follows,⁵⁷



$$K_e = \frac{P_{H_2O}}{P_{H_2} \times P_{O_2}^{1/2}} \quad (2-9)$$

Since $\Delta G^\circ = -247500 + 55.85T$ (J) for Equation (2-8), and $\Delta G^\circ = -RT \ln K_e$,⁵⁷

$$\ln K_e = \frac{247500}{8.3144 \times T} - \frac{55.85}{8.3144} \quad (2-10)$$

Since P_{H_2} is close to 1,

$$K_e = \frac{P_{H_2O}}{P_{O_2}^{1/2}} \quad (2-11)$$

$$P_{O_2} = \left(\frac{P_{H_2O}}{K_e} \right)^2 \quad (2-12)$$

If the operating temperature of a SOFC is 650 °C,

$$\ln K_e = \frac{247500}{8.3144 \times 923} - \frac{55.85}{8.3144} = 1.2278 \times 10^{11} \quad (2-13)$$

Since K_e is calculated, we can calculate the anode P_{O_2} ,

$$P_{O_2} = 5.9697 \times 10^{-26} \quad (2-14)$$

The Nernst potential at 650 °C is then,

$$E = \frac{RT}{4F} \ln \left(\frac{P_{O_2}^{cathode}}{P_{O_2}^{anode}} \right) = \frac{8.3144}{4 \times 96485.3399} \ln \left(\frac{0.21}{5.9697 \times 10^{-26}} \right) = 1.1239V \quad (2-14)$$

This equation shows how increases in operating temperature can decrease the OCP. As T increases, the RT term increases, but the anode P_{O_2} rapidly increases and the overall OCP decreases.

2.2. Potential Losses of SOFC

The Nernstian potential above assumes no change in potential as a function of current drawn. However, the performance of a SOFC can be measured by the voltage output as a function of current density drawn, and thermodynamics can no longer predict the potential in this case. If current is drawn from a SOFC, the voltage output will deviate from the equilibrium potential predicted by thermodynamics. The voltage will be lowered by various mechanisms

depending on the amount of current drawn. Figure 2-1 shows a typical I-V and a power density curve (which is a voltage multiplied by current density). The measured voltage, V , can be written as,

$$V = E_o - IR_{act.} - IR_{ohm.} - IR_{conc.} = E_o - \eta_{act.} - \eta_{ohm.} - \eta_{conc.} \quad (2-15)$$

where $R_{act.}$, $R_{ohm.}$ and $R_{conc.}$ stand for activation, ohmic and concentration polarization resistances, respectively and η stands for overpotential which can be described as a potential loss due to each polarization mechanism.

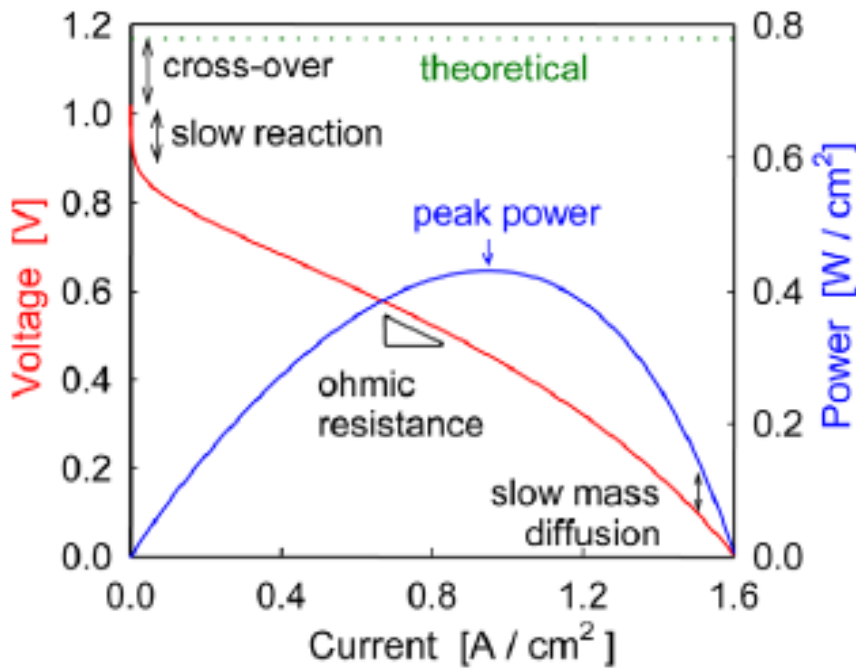


Figure 2-1. A typical current-voltage characteristics of a SOFC.²⁵

Activation polarization ensues whenever reacting chemical (including electrochemical) species are involved. An activation energy barrier must be overcome in order for the reaction to proceed. This results in a potential drop which may be regarded as the extra potential necessary to overcome the energy barrier of the rate-determining step of the reaction, and is related to the current passing through the cell by the phenomenological Butler-Volmer relation.⁵⁸ Ohmic

polarization is caused by resistance to the flow of ions in ionic conductors and electrons in electronic conductors, and by contact resistances between cell components. Concentration polarization occurs when reacting species are supplied to reaction sites slower than they are consumed, or when reaction products are not removed fast enough so that they block the reaction sites. Note that the slope of current density vs. voltage curve is the ASR.

2.2.1. Activation Polarization

The energy necessary to overcome a reaction at an electrode increases exponentially with current. This was first observed by Tafel in 1905.⁵⁹ The relationship between activation polarization and activation energy is not yet understood, but an empirical equation was developed and used in the form of the Butler-Volmer equation.

$$i = i_o \exp\left(\frac{\alpha_a n \eta_{act} F}{RT}\right) - i_o \exp\left(\frac{-\alpha_c n \eta_{act} F}{RT}\right) \quad (2-16)$$

where i_o is the exchange current density, α the apparent transfer coefficient, n the number of electrons transferred, and F is Faraday's constant. For hydrogen electrodes, the apparent transfer coefficient, $\alpha \sim 0.5$. For oxygen electrodes, α varies from 0.1 to 0.5. However, for SOFC reactions, α can be treated as 0.5 assuming change in α makes little impact.⁶⁰ Interestingly, for SOFCs, when the number of electrons, n , is 1, good fits to the Butler-Volmer equation are obtained,⁶¹ while most SOFC reactions obviously show n values of either 2 or 4 depending on the convention used for writing the chemical equations involved.

The Tafel equation can be used to look at the electrochemical reaction at an electrode with overpotential, η , in terms of current.⁵⁶ The Tafel equation can be viewed as another expression of the Butler-Volmer equation using the constant A .

$$\eta = A \log\left(\frac{i}{i_o}\right) = \frac{RT}{n\alpha F} \log\left(\frac{i}{i_o}\right) \quad (2-17)$$

The constant A is higher for an electrochemical reaction which is slower. The exchange current density, i_o , is higher if the reaction is faster. Now with the Tafel equation, one can derive the actual cell voltage, with respect to E and η .

$$V = E - A \log\left(\frac{i}{i_o}\right) \quad (2-18)$$

Thus, reductions in activation polarization (that is, reductions in V in the equation), can only be achieved by increasing the exchange current density or by increasing T . Therefore, increasing the actual number of reactions sites (since i_o is normalized with area) and using catalytically more active materials can reduce the activation polarization.

2.2.2. Ohmic Polarization

The ohmic polarization was already described in Chapter 1. Here, note that the equation only deals with the resistance caused by ionic migration through electrolytes, but the anode and cathode can also exhibit substantial ohmic polarization.⁶²

$$\eta_{ohm.} = i \times ASR = i \times \rho \times T_{Thickness} = \left(\frac{i}{\sigma}\right) \times T_{Thickness} \quad (1-1)$$

Ohmic polarization is simplest type of loss to understand and it is clear that the deposition of a thin electrolyte or the use of materials exhibiting higher ionic conductivity can reduce the ohmic polarization. Additionally, to reduce the ohmic resistance from electrodes, deposition of thick electrodes to remove sheet resistance, or use of current collectors is necessary.⁵²

2.2.3. Concentration Polarization

When current is drawn from a SOFC, consumption of gas at electrodes causes a decrease in partial pressure of that gas. This phenomenon changes the potential across the electrolyte. By modifying the equation for Nernst potential, one can express the change in potential as a function of the change in partial pressure,

$$\Delta V = \frac{RT}{4F} \ln\left(\frac{P_2}{P_1}\right) \quad (2-19)$$

The limiting current, i_l , is the current at which fuel is being consumed as quickly as it is being supplied. At this point, the cell voltage will be zero. Rewriting the equation (2-19) gives,

$$P_2 = P_1 \left(1 - \frac{i}{i_l}\right) \quad (2-20)$$

Substituting the equation (2-20) into equation (2-19),

$$\Delta V = \frac{RT}{4F} \ln\left(\frac{i}{i_l}\right) \quad (2-21)$$

Equation (2-21) represents the potential losses due to mass transport phenomena. A more rigorous concentration polarization model for the anode and cathode were developed by Kim et al.,⁶³ and Zhu et al.⁶¹

2.2.4. Internal Leakage Current

The use of a mixed ionic electronic conducting (MIEC) electrolyte such as GDC will additionally lower the potential by internal leakage currents through the electrolyte. The potential across a MIEC electrolyte is given by the following equation,

$$OCP = t_i \times \frac{RT}{4F} \ln\left(\frac{P_{O_2}^{cathode}}{P_{O_2}^{anode}}\right) \quad (2-22)$$

where t_i is the ionic transference number.

It is often mentioned that the potential drop caused by internal leakage currents leads to total efficiency drops. This point of view arises from calculating the efficiency of a SOFC using the following equation:

$$Efficiency = \frac{\Delta G}{\Delta H} \times 100 \quad (2-23)$$

where, ΔH is enthalpy of formation of the fuel and ΔG is Gibbs free energy of the fuel oxidation reaction. ΔG is a function of the potential of the cell ($\Delta G = -nEF$). However, using this equation for measuring the overall SOFC efficiency can be misleading, since according to the equation above, the maximum efficiency of a SOFC using hydrogen fuel and oxygen can go above 80%.⁵⁶ In other words, the efficiency loss predicted by thermodynamics is only 20%. However, overall performance of SOFC is strongly affected by irreversibility, such as polarization mechanisms. An electrolyte with larger amount of leakage current can still be considered for use as an electrolyte if it has a very high ionic conductivity which can compensate voltage losses caused by internal currents.

2.2.5. Combination of Each Polarization

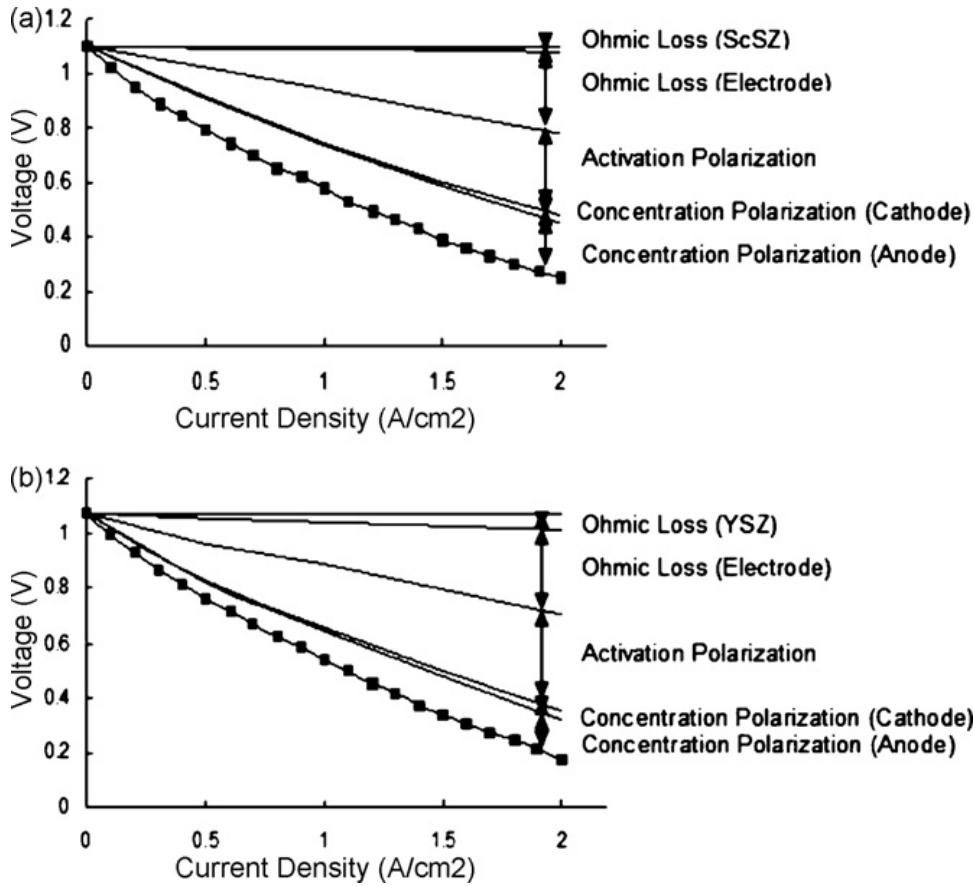


Figure 2-2. Separation of polarizations using a model developed by Yoon et al.⁶⁴ (a) Sc stabilized zirconia (ScSZ) electrolyte based SOFC. (b) YSZ electrolyte based SOFC.

In this section, a combination of each polarization mechanism is presented to better understand the I-V behavior of a SOFC, which is a main characterization tool of this dissertation. As seen in Figure 2-2, the I-V curve represents a potential drop from the theoretical OCP by various mechanisms. For an electrolyte with t_i approaching unity, such as YSZ, combining equations developed for each polarization mechanism is relatively easy compared to MIEC electrolytes. A simple way of expressing potential drop is to combine simple equations above in this dissertation.

$$V = E - (i + i_n)ASR - A \ln\left(\frac{i + i_n}{i_o}\right) + B \ln\left(1 - \frac{i + i_n}{i_l}\right) \quad (2-23)$$

where, i_n is the internal leakage current density, A is the constant in Equation (2-17), and B is the constant in Equation (2-21). A better expression for potential drop in YSZ based SOFCs, which can be used for fitting to an actual I-V curve, were demonstrated by Yoon et al.⁶⁴ They demonstrated a simple mathematic conversions of each equation lead to a equation where cell voltage is a function of applied current.⁶⁴ It should be noted here that their work is only valid for pure ionic conductors.

A more rigorous performance modeling study has been discussed by Amphlett.^{65,66} The most advanced and sophisticated equation, which can predict the I-V behavior of MIEC electrolyte-based SOFCs, was developed by Duncan et al., where the cathode and anode activation polarizations and the cathode and anode ohmic polarizations were separated.⁶² The I-V characteristic of the Full GDC AFL sample at 650 °C in Figure 4-5 was analyzed using his model and it can be found in his publication.⁶²

CHAPTER 3 EXPERIMENTAL PROCEDURES

3.1. SOFC Fabrication

3.1.1. Anode Tapecasting

The Ni - GDC anode supports were synthesized by tape casting a mixture of NiO (Alfa Aesar, 99% purity, CAS 1313) and GDC (Rhodia, LOT H-050708) powders. The powder mixture contains 65 weight % of NiO. Both raw oxide powders were weighed (to obtain 150 g batch of powder mixture), and were mixed in toluene (Fisher Scientific) (13.6 wt %) and ethanol (Fisher Scientific) (11.3 wt %). A 1 wt % of Solsperse (Air Products and Chemicals) was added to the slurry as dispersant. Further, a mixture of di-n butyl phthalate (DBP, Alfa Aesar) (4.3 wt %), and polyethylene glycol (PEG, Fisher Scientific) (0.8 wt %) was added as plasticizer, while polyvinyl butyral (PVB, Acros Organics) (8.4 wt %) was added to the slurry as binder. Mixing was performed using ball milling using zirconia ball media for 24 h. The resulting slurry was then transferred to a vacuum chamber, for de-airing. During this process, the slurry was constantly magnetically stirred to avoid any solidification. The slurry was then tape-cast using a tape-caster (Procast from DHI, Inc.) on G10JRM Silicone coated Mylar (R. E. Mistler, Inc.), with a caster speed of 10 cm/min. The substrate temperature was maintained at 80 °C during this process with a doctor blade gap was 800 µm. The NiO - GDC tape was subsequently dried at 100 °C for 2 h in an oven (~ 500 µm after drying). Circular green tapes with 32 mm diameter were then punched out from the tape, and partially sintered at 900 °C for 2 h.

3.1.2. SNDC Electrolyte Deposition

The co-precipitation technique was used to synthesize phase pure powder of $\text{Sm}_{0.075}\text{Nd}_{0.075}\text{Ce}_{0.85}\text{O}_{2-\delta}$. One of the main objectives of using wet chemical routes is to obtain fine particle size powder to enhance the sintering kinetics so that highly dense electrolytes can be

synthesized at lower sintering temperature and time. Highly pure cerium nitrate ($\text{Ce}(\text{NO}_3)_3 \cdot 6\text{H}_2\text{O}$, Alfa Aesar, 99.99%), samarium nitrate ($\text{Sm}(\text{NO}_3)_3 \cdot 6\text{H}_2\text{O}$, Aldrich, 99.999%), and neodymium nitrate ($\text{Nd}(\text{NO}_3)_3 \cdot 6\text{H}_2\text{O}$ Alfa Aesar, 99.9%) were used as starting raw materials. They were weighed in the stoichiometric proportions and dissolved in de-ionized water to produce an aqueous solution. Excess ammonia solution (Acros Organics, 28-30% of NH_3 solution in water) was added to the stirred solution by 5 ml with 30 minutes time interval. The pH was stabilized at 12 to make sure all the cations are precipitated. The addition of ammonia solution resulted in the formation of yellowish brown color precipitate. The precipitate was filtered, and then subsequently dried at 80 °C for 12 h. The agglomerated powder was then ground to fine particles using mortar and pestle. The powder was then calcined at 900 °C for 10 h in air. After calcination the agglomerated powder was ground using mortar and pestle to fine size particles which were then sieved (212 μm aperture opening). An Intel CPS 120 diffractometer was used to obtain the X-ray diffraction (XRD) pattern of the $\text{Sm}_{0.075}\text{Nd}_{0.075}\text{Ce}_{0.85}\text{O}_{2-\delta}$ using $\text{Cu K}\alpha$ radiation. A monochromator crystal was used to separate out $\text{Cu K}\alpha_1$ from the incident X-ray beam.

For the deposition of the SNDC electrolyte on the anode support, the $\text{Sm}_{0.075}\text{Nd}_{0.075}\text{Ce}_{0.85}\text{O}_{2-\delta}$ powder was ball milled for 24 h using zirconia ball media, in ethanol medium with Solsperse as a dispersing agent. For a typical 10 g batch of $\text{Sm}_{0.075}\text{Nd}_{0.075}\text{Ce}_{0.85}\text{O}_{2-\delta}$ powder, 26.3 wt % of ethanol and 1 wt % of Solsperse were used. After 24 h of ball milling, 10 wt % of PVB and 3 wt % of DBP were added into the slurry. The ceramic slurry was again ball-milled for another 24 h using the same ball media. Before the deposition, ceramic slurry was sonicated for 10 minutes. The ceramic slurry of $\text{Sm}_{0.075}\text{Nd}_{0.075}\text{Ce}_{0.85}\text{O}_{2-\delta}$ was then deposited twice onto the anode (NiO-GDC) surface using a pipette. In between coats 30 minutes of drying

step was applied. The electrolyte deposited anode samples were subsequently, heat-treated at 120 °C for 5 h in an oven. The bi-layered structure of the electrolyte and anode was then co-sintered at 1550 °C for 4 h using a 3 °C/min ramp rate in air.

3.1.3. GDC Electrolyte Deposition

For deposition of the GDC electrolyte, the GDC powder from Anan was ball milled for 24 h with Solspere in ethanol. PVB and DBP were added after the first ball-milling step and ball-milled using zirconia ball media for another 24 h. For deposition of the GDC electrolyte, the GDC slurry was sprayed onto the anode surface using a paint spray gun (Excell). The setup for spray coating can be found in APPENDIX B. The samples were moved to a vacuum oven and heat-treated at 120 °C for 5 h. The bilayered structure of the electrolyte and anode was co-sintered at 1450 °C for 4 h using a 3 °C /min ramp rate in air.

3.1.4. LSCF Composite Cathode

The cathode ink was prepared by mixing $\text{La}_{0.6}\text{Sr}_{0.4}\text{Co}_{0.2}\text{Fe}_{0.8}\text{O}_{3-\delta}$ (Praxair Specialty Ceramics, 99.9% purity) and the GDC powder in a 1:1 weight ratio, using mortar and pestle. Alpha-terpinol (40 wt % of the powder) was added as a solvent, and DBP (6.7 wt % of the powder) was used as a plasticizer. Further, PVB (2.3 wt % of the powder) dissolved in ethanol (21 wt % of the powder) was added as a binder. After mixing and grinding the cathode ink in mortar and pestle for 1 h, the ink was brush-painted evenly onto the electrolyte (deposited on NiO/GDC tape). The first layer of cathode ink was dried in an oven at 120 °C for 1 h. The second layer of the same cathode ink was then evenly brush painted on top of the first layer. After applying the cathode on top of the electrolyte, samples were then fired at 1100 °C for 1 h. As a current collector, Pt paste (CL11- 5349, Heraeus) was brush-painted onto both electrodes

along with a Pt mesh and Au connecting wires. Samples with current collectors and connecting wires were then finally heat-treated at 900 °C for 1 h.

3.1.5. AFL Deposition

For the GDC functional layer, 1 M of GDC precursor solution was prepared in an ethanol solvent. Upon complete dissolution of the precursors, the solution was transferred to a paint spray gun (Excell), sprayed onto the anode substrate, and heat-treated at 900 °C for 1 h.

For the Ni-GDC functional layer, Ni precursor solution was prepared with same concentration as GDC solution. Ni precursor solution and GDC precursor solution was sprayed in turns to deposit composite Ni-GDC composite AFL. Deposition rate was controlled by spray time which was maintained to be same to deposit same amount of Ni and GDC. The composite AFL was heat treated at 900 °C for 1 h.

For the multilayered AFL, firstly, the same procedures for Ni-GDC composite AFL was done, and the sample was placed on a hot plate (Corning). Upon desired amount of GDC precursor was deposited, the sample was heat treated at 900 °C for 1 h. To quantify deposition rate, mass change after spraying and heat-treatment was measured for all three AFL samples.

3.2. Fabrication of ESB/GDC Bilayer Electrolytes

The fabrication of SOFCs with single GDC electrolyte is improved sequentially starting from a co-pressing procedure, to tapecasting anode support, to anode functional layer (AFL) on tapecast anode. Various ESB depositions on sintered GDC are evaluated to form a dense ESB layer, from screen printing, to colloidal drop coating, to cold PLD, to hot PLD. Note that there is no terminology as cold PLD and hot PLD. In this study these terms were used to distinguish PLD without substrate heating (cold PLD) and with substrate heating (hot PLD).

3.2.1. Co-pressing Procedure

The first method used to fabricate bilayer cells involved co-pressing fine GDC powders onto composite NiO-GDC anode supports. The anode supports were prepared by uniaxial pressing a well-mixed powder of NiO (Alfa Aesar), a very fine GDC (Rhodia), and a PVB (Alfa Aesar) binder (3 wt%) in a 1 1/8" cylindrical die at ~14 MPa. Next, ~0.35 g de-agglomerated GDC powder was added to the die, carefully and uniformly spread across the anode substrate surface, and pressed at ~42 MPa. The pellets were then pressed isostatically at 250 MPa, and fired at 1450 °C for 4 h using a 3 °C/min heating rate and a 400 °C, 1 h binder burnout step. The resulting electrolytes were relatively thick (~50 µm).

An ESB layer was then screen printed on top of the sintered GDC surface of one cell. The ESB powder used in the screen printing ink was prepared by the solid state technique. Erbium oxide (Alfa Aesar) and bismuth oxide (Alfa Aesar) powders were weighed in stoichiometric amounts, ball milled for 24 h and calcined at 800 °C for 10 h to yield $\text{Er}_{0.4}\text{Bi}_{1.6}\text{O}_3$. ESB inks were then prepared by mixing ~1 g of the prepared ESB powder (slightly wetted with an ethanol solvent) with alpha-terpineol (Alfa Aesar), DBP (Alfa Aesar), and a solution of 10 wt% PVB in ethanol using a 3:1:2 volume ratio in a mortar and pestle until the ink reached a honey-like consistency. The ink was then screen printed onto the GDC side of the cell and fired at 890 °C for 4 h.

For cathoding, two different composite materials were used: $\text{La}_{0.6}\text{Sr}_{0.4}\text{Co}_{0.2}\text{Fe}_{0.8}\text{O}_{3-\delta}$ (Praxair)-GDC and a low ASR BRO7-ESB. Synthesis of BRO7 powders and optimization of BRO7-ESB composite cathodes have been described previously,⁵² and involve sedimentation to narrow the size and distribution of particles which were prepared by solid state synthesis. Cathode inks for both materials were prepared in a similar manner to that described above for the ESB bilayer electrolyte screen printing ink. For LSCF-GDC composites, a 1:1 weight ratio was

used, and for BRO7-ESB, the optimized composition⁵² was used. The previous section describes application of LSCF-GDC composite cathode in details. BRO7-ESB cathodes were brush painted onto the electrolyte surface, dried at 120 °C, and a second layer was applied. BRO7-ESB cathodes were fired at 800 °C for 2 h. A Pt current collector (Heraeus) was paint brushed onto both electrodes of cells utilizing LSCF-GDC composite cathodes, while a pure BRO7 current collector (also prepared from the ink synthesis method described above) was applied to both electrodes of cells utilizing BRO7-ESB cathodes. Finally, lead wires and meshes were attached to the electrodes (using Pt paste on the anode side and the same current collector ink used on the cathode side) and fired in-situ with the testing apparatus. Three types of samples were studied using the co-pressing technique: two utilizing a single-layer GDC electrolyte with either an LSCF-GDC cathode or a BRO7-ESB cathode, and one utilizing a bilayer ESB/GDC electrolyte with a BRO7-ESB cathode.

3.2.2. Colloidal Route

The second stage of SOFC fabrication involved GDC spray coating on tape-cast anodes followed by ESB colloidal drop coating. The anode support was prepared by tapecasting as previously described. Anode tapes were presintered at 900 °C for 2 h and GDC electrolytes were deposited by spray coating. Details on anode tapecasting and GDC spray coating were described by Ahn et al.,^{54,55,67} and previous section of this dissertation.

For colloidal ESB deposition, in order to increase the yield of fine ESB powders, a co-precipitation route was employed. Pure Ce-Nitrate and Er-Nitrate were used as starting raw materials. They were weighed in the stoichiometric proportions and dissolved in 70 % nitric acid to produce a solution. Excess ammonia solution (Acros Organics, 28-30 % of NH₃ solution in water) was added to the stirred solution to increase the pH value to 12. The addition of ammonia

solution resulted in the formation of yellowish brown color precipitate. The precipitate was filtered, and then subsequently dried at 80 °C for 12 h. The agglomerated powder was then ground to fine particles using mortar and pestle. The powder was then calcined at 900 °C for 10 h in air.

For the colloidal slurry, ESB powder was ball milled with Solsperse (Air Products and Chemicals), PVB, and DBP in ethanol for 24 h, and drop-coated onto the sintered GDC electrolyte surface. The drop coating was repeated until a desired thickness was achieved. The ESB layer was sintered at 890 °C for 4 h using a 400 °C 1h binder burnout step, and a 3 °C/min ramp-rate. The same BRO7-ESB composite cathode as described above was applied onto the ESB surface. A LSCF-GDC composite cathode was applied to a tape-cast cell utilizing a single GDC layer as a baseline. I-V measurements were carried out on the two different samples in the same way with a Solartron 1287. 30 sccm of dry air and 30 sccm of wet hydrogen were supplied to the cathode and anode side, respectively. For the bilayer sample 90 sccm of wet hydrogen was applied to examine the effect of gas flow-rate on I-V maintaining 30 sccm of air. ASR values were calculated from the initial slopes of the I-V curves due to their non-linear nature at most current regions.

3.2.3. Cold PLD

PLD is a thin film deposition technique using evaporation of plasma vapor from a solid target by impinging the target with high power pulsed laser. The evaporated plasma, which is referred as plume, migrates to the substrate and deposit an ultra thin layer. Use of plasma plume in PLD requires ultra high vacuum usually but oxygen filling is frequently used for deposition of fully oxidized oxide layers.

PLD of ESB on spray coated GDC was used in order to enhance ESB layer density. Figure 3-1 shows the schematics of the PLD system used. The anode support was prepared by tape

casting as described above. The important addition in this stage of fabrication is an AFL deposited between the GDC electrolyte and the Ni-GDC anode. The AFL was prepared by spraying GDC precursor onto a presintered anode and heat-treated at 900 °C, 1 h.

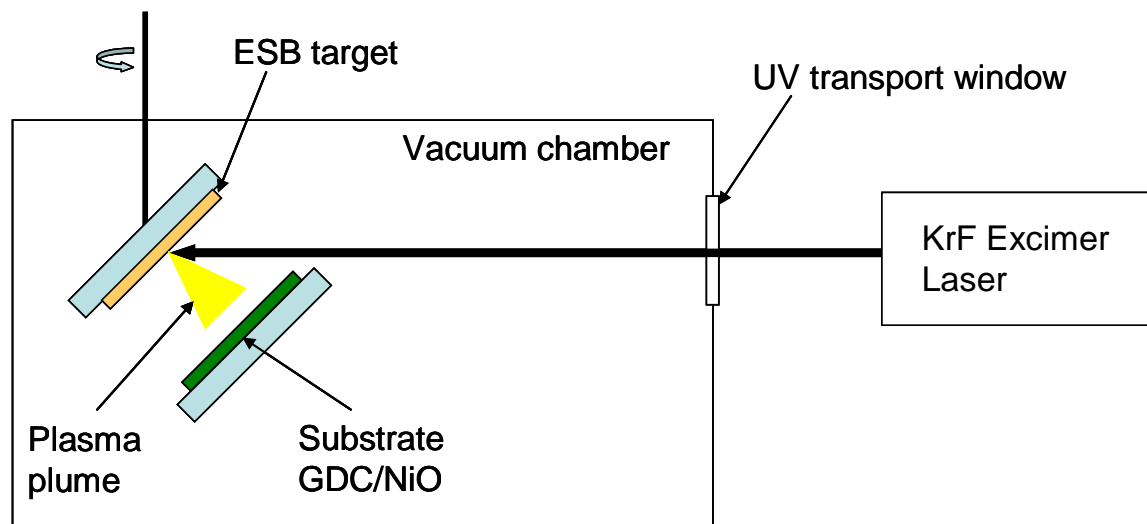


Figure 3-1. PLD system with KrF excimer laser.

For PLD deposition the target was made by uniaxial pressing of ESB powder and sintering at 890 °C for 4 h. ESB powder was prepared by solid state route as previously described in this manuscript. A KrF eximer ($\lambda = 248$ nm) laser was used with laser fluence of 3 J/cm², and a frequency was 5 Hz. The distance between target and substrate was 5 cm. O₂ filling was 0.3 Torr vacuum level. The substrate (GDC surface on a NiO-GDC anode) was maintained at room temperature. The deposition was made for 45 min. To achieve a pure ESB phase, an annealing step of 700 and 890 °C for 4h was used and the film was examined by XRD. The Crystallinity of heat-treated ESB layers was compared with the ESB layer without heat treatment. The thickness of the ESB layer by cold PLD was hard to measure because of severe roughness of the film (Figure 6-8).

3.2.4. Hot PLD

To further improve ESB layer quality PLD deposition was performed with substrate (GDC electrolyte and AFL on the Ni-GDC anode) heating to 630 °C. The target (ESB pellet) and substrate were the same as those used for Cold PLD. The parameters used for PLD were the same as with Cold PLD, but there was no heat treatment step after the deposition. XRD was employed to check crystallinity of the as-deposited ESB layer. I-V characteristics were carried out by a Solartron 1287 and the impedance analysis was performed by a Par-stat using 90 sccm of air and wet hydrogen. Again, ASR_{IV} and $ASR_{Impedance}$ were used to distinguish the total cell ASR obtained by the two different methods.

3.3. Characterization

3.3.1. Microstructural Analysis

Microstructures of each component of the SOFC before and after testing can be investigated by SEM. Porosity of the bulk of the anode and cathode can be determined. Also, SEM can easily measure other parameters that may be of interest such as anode thickness and pore sizes. Another important reason for SEM being one of the major characterization tools is that it can measure the penetration of unwanted impurity into the matrix by back-scattered imaging.

When images in high resolution (up to 100,000x) are required, field emission scanning electron microscope (FE-SEM) can be used to characterize the detailed microstructure of the fuel cell sample. In order to view the cross-section of all three layers (anode, electrolyte, and cathode) of the cell, the test sample was fractured, and some times, embedded in epoxy-resin, and mechanically polished.

3.3.2. XRD

XRD is a valuable tool for confirming acquisition of a designated phase. In addition, phase purity (both before and after electrochemical testing) can be judged based on the peak spectrum it produces. For use with a SOFC study, XRD can be used as a post analysis tool. The mean sizes of the crystallites are determined from the x-ray diffractograms, using the Scherer equation (3-1) and assuming that the particles are spherical;

$$L = 0.9\lambda / B_{2\theta} \cos \Theta_{\max} \quad (3-1)$$

L is the mean crystallite size, λ is the x-ray wavelength (0.154056 nm for the Cu K α radiation), $B_{2\theta}$ is the width of the diffraction peak at half-height, and θ_{\max} is the angle at the peak maximum position.

3.3.3. I-V Measurement

Key characteristics of SOFC can be measured using the plot of voltage output as a function of electrical current density recorded by a potentiostat. The theoretical background of the I-V characteristics are provided in chapter 2 of this dissertation. Measurable properties using potentiostat include I-V characteristics, power density as a function of current density, open circuit potential and degradation of voltage output depending on given current.

A sample with silver lead wires and platinum current collectors was placed on a zirconia tube in a custom-made testing apparatus. The sample leads were connected to gold leads from the air-side and fuel-side in the reactor. The fuel cell sample was sealed (anode side) using a two-part ceramabond sealant (a mixture of 517-powder and 517-liquid from Aremco). Ceramabond was applied around the edge of the sample as a sealant, and was cured inside the testing furnace. The sealing was completed while the furnace was ramped to the operation temperature. Once operating temperature was reached, hydrogen was flown through a bubbler as the fuel to the

anode and dry air gas was fed to the cathode. Flow rates were maintained using mass flow controllers. Depending on the chosen power generation level, 30 sccm or 90 sccm of dry air and wet hydrogen were supplied to the cathode and anode, respectively. Note that the flow rates should be maintained symmetric during all measurements, because the OCP can be lowered by asymmetric flow-rates due to external gas leakage. The cell OCP was monitored using a Solartron 1287 potentiostat until a stable value was reached, and the I-V measurements were taken with the same instrument.

As it was mentioned in chapter 2, the slope of the I-V curves gives the ASR. The ASR near the open circuit region can be compared with the ASR measured by the impedance spectroscopy under no bias. Taking the initial slope of the I-V curves, total cell ASR was estimated. Throughout this dissertation, the regions from 0 to 0.02 A/cm² in most I-V curves were used to measure the ASR_{IV} and the values were compared with ASR_{Impe}. Less discrepancy between ASR_{IV} and ASR_{Impe} means higher credibility of the data, since they were measured by different devices.

3.3.4. Impedance Spectroscopy

Impedance spectroscopy is a valuable tool for characterization of electrochemical processes. A small AC potential (across a range of frequencies) is applied to the sample, and the current response (impedance using Ohm's Law) through the sample is measured over a range of frequencies. This response is usually represented as a "Nyquist" or "Cole-Cole" plot where the real part of the impedance is the abscissa and the imaginary part of the impedance the ordinate. The response of the cell is usually modeled in terms of equivalent circuits, i.e., a group of electrical circuit elements (resistors, capacitors, inductors) that are connected in a way that would give the same response as the cell.

After the I-V measurement, impedance analysis was carried out at open circuit conditions using two-point probe (cathode and anode) measurements with a Par-stat 2273 (Princeton Applied Research) with a frequency range of 10 KHz to 0.01 Hz and an ac signal strength of 10 mV at various temperatures from 500 to 650 °C. Impedance spectra were used to calculate the total ASR. From the high frequency complex-plane intercepts of the impedance spectra with the real axis, the ohmic ASR values were calculated normalizing the resistance according to cathode area. Electrode ASR values were calculated from the difference between low and high frequency intercepts, also normalizing the difference according to cathode area.

From the IV characteristic measurements, electrolyte potential losses can be easily separated because electrolyte losses are purely ohmic. However, the cathodic polarization and anodic polarization are not easy to separate. So, three-point measurements are necessary. However, even in an impedance study, separating cathode and anode contributions is very difficult because of the reference electrode location on the thin electrolyte.^{68,69} The best way to measure the anode polarization is to use a thick electrolyte with an imbedded reference electrode. However, if we fabricate such a cell, it is different from the actual cell we are targeting, which has a thin electrolyte.

It is safe to assume that reported anodic polarizations using three-point measurements with a reference electrode placed on the thin electrolyte only measures the polarization for that specific cell geometry. This configuration should be used to measure the difference between polarization measurements depending on the research parameters, not to measure the actual anodic polarizations. Throughout this dissertation, all impedance measurements were done using the two-point probe method under open circuit conditions, which only separates ohmic and electrode polarizations. Knowing values of cathodic polarization losses of LSCF-GDC cathodes

on GDC electrolytes from previous measurements using a symmetry cell setup, the anodic polarization can be acquired by subtracting out the cathodic polarization from the overall electrode polarization. The calculated anodic polarizations may not be actual values, but will provide a standard to compare each sample to, assuming that the same cathode on both thin film and thick pellet GDC electrolytes will have similar cathodic polarizations. Figure 3-2 shows the measurement setup, where most samples discussed in this dissertation, were tested.

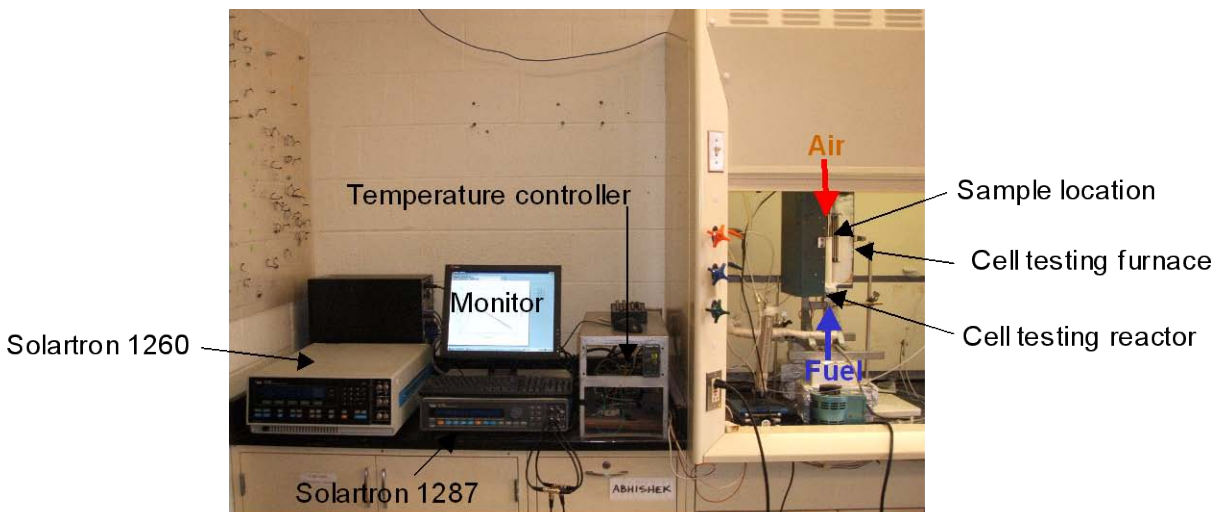


Figure 3-2. Electrochemical measurement station

CHAPTER 4
ANODE FUNCTIONAL LAYER FOR IT-SOFC

4.1. Homogeneous Functional Layers

4.1.1. Microstructural Analysis

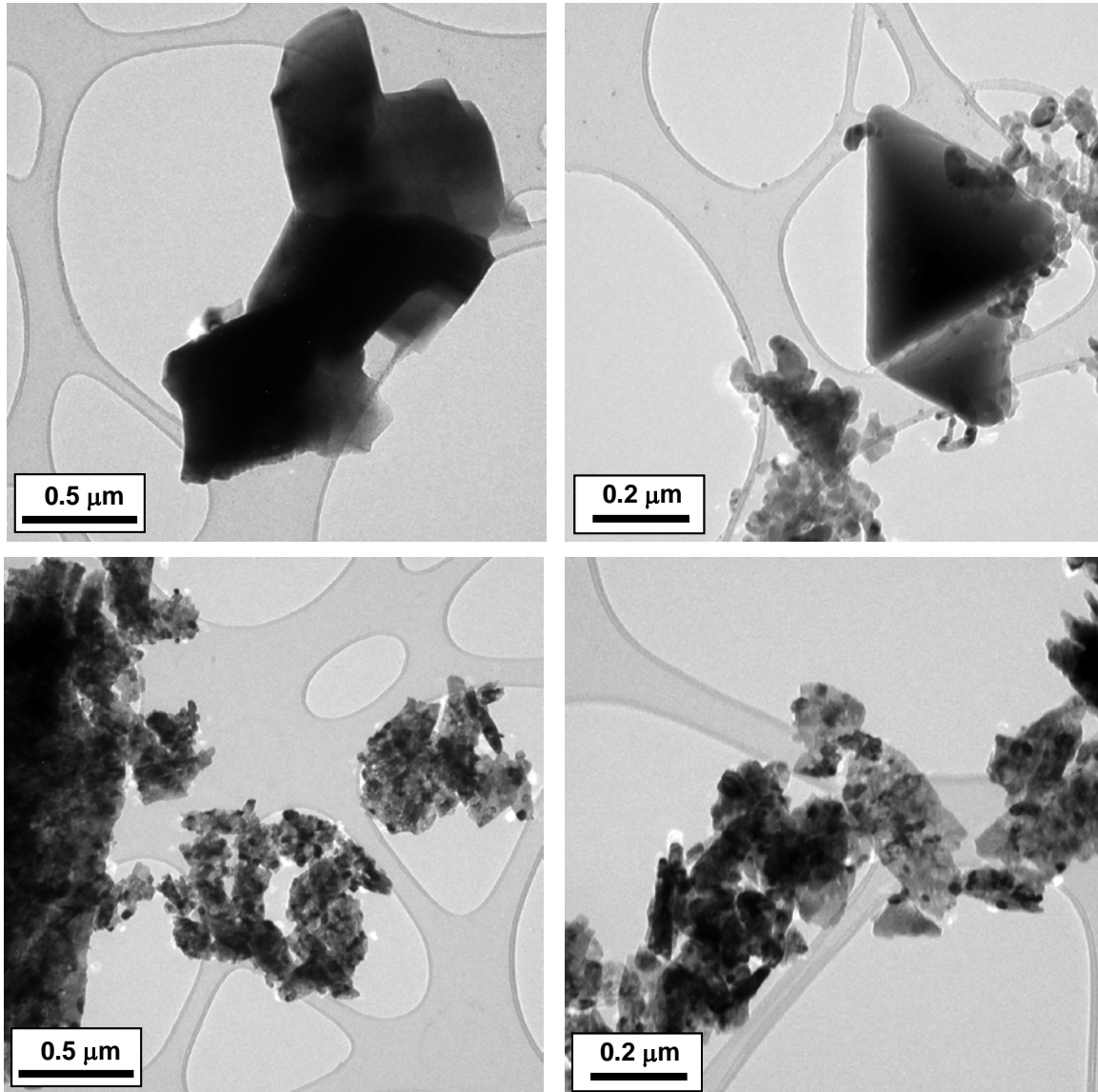


Figure 4-1. TEM images of raw powders of NiO (top) and GDC (bottom) used for tape casting of anode support.

Figure 4-1 shows TEM images to compare the relative particle sizes of NiO and GDC powders used for tape casting of the anode. NiO particles are mostly micron-sized, while GDC particles are less than 100 nm forming aggregates due to their high surface area. Large micron-

sized NiO powder was used for tape casting to achieve sufficient anode porosity without addition of pore formers. The use of large NiO powder, which will form nickel catalysts for hydrogen oxidation, can cause a large anodic polarization. Reducing the additional anode polarization by applying an AFL was the focus of this study.

Aggregates of GDC particles must be well dispersed especially for GDC electrolyte deposition as slurries with aggregated particle clusters form a porous film after sintering. As described in the experimental section, a polymeric dispersant, Solsperse, was used for this purpose. The microstructure of the GDC electrolyte prepared with Solsperse is shown in Figure 4-4.

Since the GDC functional layer is the same material as the electrolyte, after sintering, it is indistinguishable from the electrolyte in cross-sectional SEM images. Conclusive evidence of the AFL and its effect on the performance can be only acquired by electrochemical measurements, which will be discussed in this manuscript. However, to verify formation of the AFL visually, anode surface views with and without the AFL were taken before GDC electrolyte deposition. Figure 4-2 shows the change in anode surface porosity and roughness by introduction of a GDC functional layer. Images of the anode surface with AFL were taken after heat treatment at 900 °C for 1 h. As seen in Figure 4-2, the anode surface without a GDC functional layer is very porous and rough. On the anode surface it is easy to find large voids formed by use of large NiO particles. Formation of a dense membrane by colloidal deposition is difficult to achieve on this type of porous surface especially with materials that are difficult-to-sinter, such as ceria.

In Figure 4-2 a partially-sprayed GDC functional layer on the anode successfully blocks most large pores on the surface. It should be noted that a thick layer of GDC covering the entire

anode surface does not easily form unless a significant amount of GDC precursor is sprayed. Up to certain level of precursor spraying, the precursor solution is sucked into the pores and coagulates inside the pores filling the voids of anode surface. This results in bare nickel particles on the anode surface.

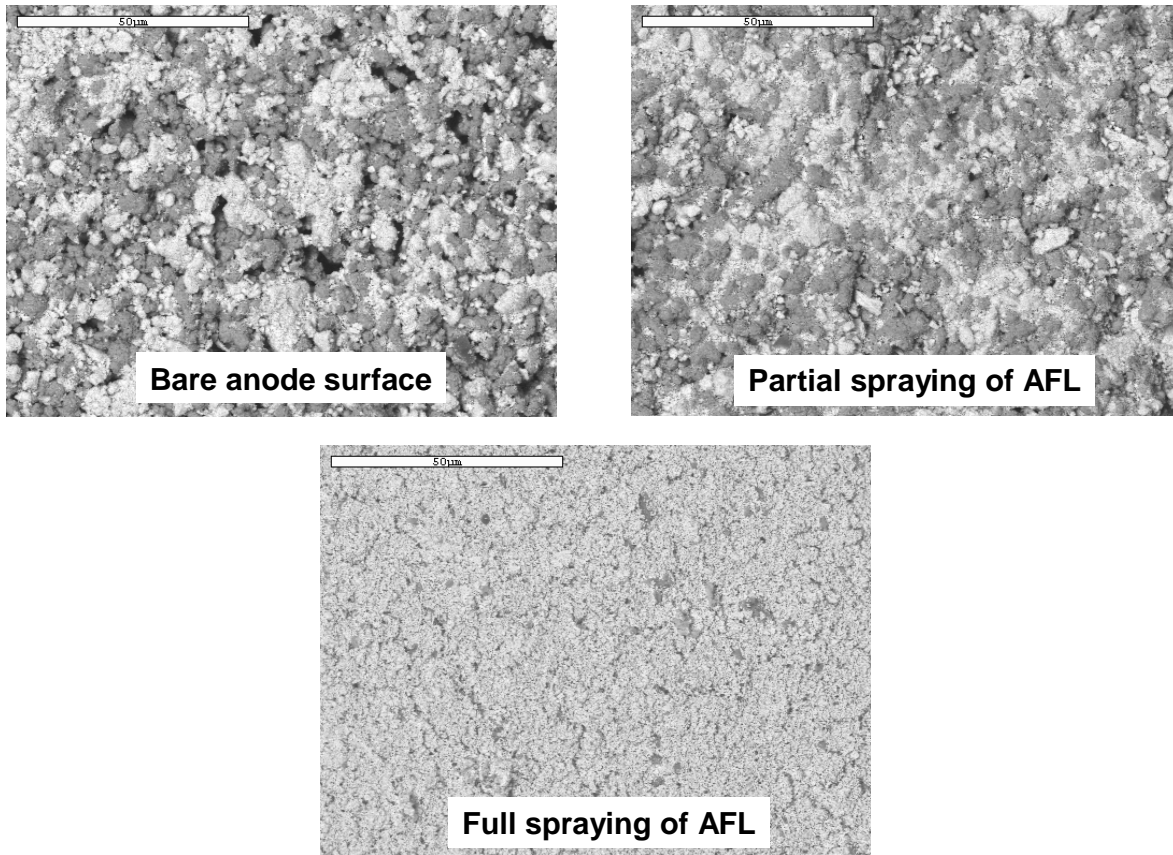


Figure 4-2. Backscattered images showing change in anode surface porosity and roughness by GDC functional layer deposition. Images were taken after pre-sintering the AFL at 900 °C for 1 h. The top left figure shows bare anode layer surface, the top right figure shows partial spray coating of the GDC functional layer, and bottom figure shows the fully sprayed GDC functional layer.

Figure 4-2 shows that the fully sprayed GDC functional layer covers the entire anode surface with GDC, creating a relatively smooth and uniform surface for high quality GDC electrolyte deposition. NiO particles on the anode surface are fully covered with GDC particles

when a functional layer is used. This GDC functional layer is expected to provide better adhesion between the anode and the electrolyte.

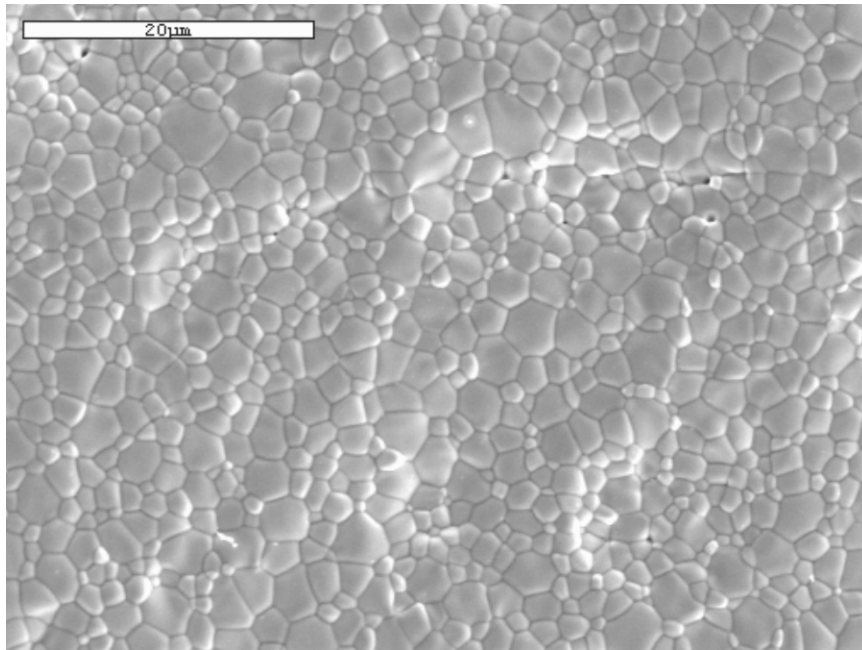


Figure 4-3. SEM micrographs showing of the surface view of the GDC electrolyte deposited by spray coating on AFL coated anode.

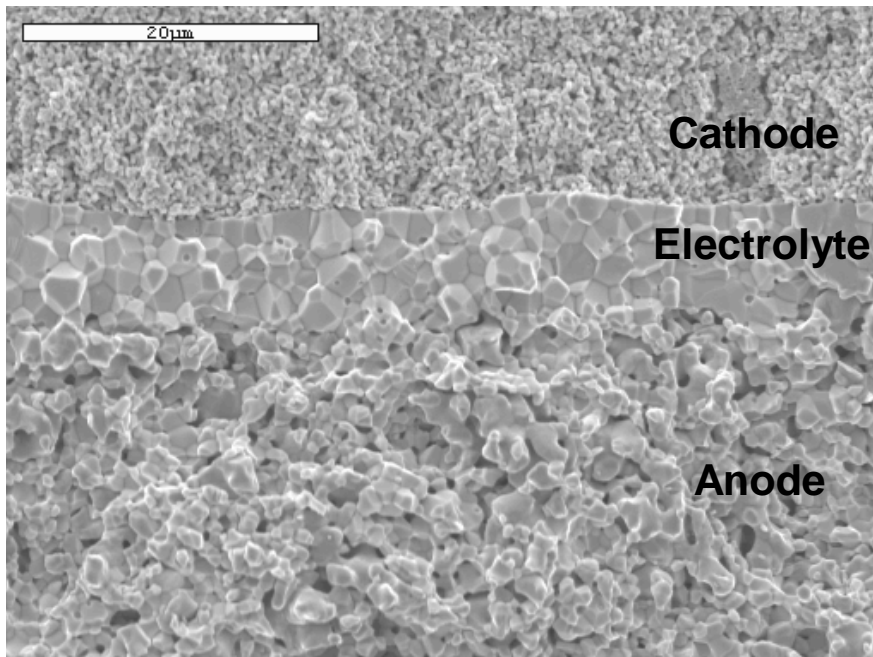


Figure 4-4. SEM micrograph showing the cross-sectional view of the SOFC with AFL after I-V testing.

Figure 4-3 shows the surface of the GDC electrolyte deposited by spray coating onto anode surface (fully covering GDC functional layer). The electrolyte deposition was followed by sintering at 1450 °C for 4 h. As seen in Figures 4-3 and 4-4, small pores are observed on the surface and in the bulk of the electrolyte. However, the cross-sectional view of GDC electrolyte (Figure 4-4) shows no open porosity. The thickness of the GDC electrolyte is estimated to be 10 μm from the SEM image. As seen in Figure 4-4, after reduction of NiO to Ni during operation, the anode became very porous, sufficient for gas transport.

4.1.2. Electrochemical Performance

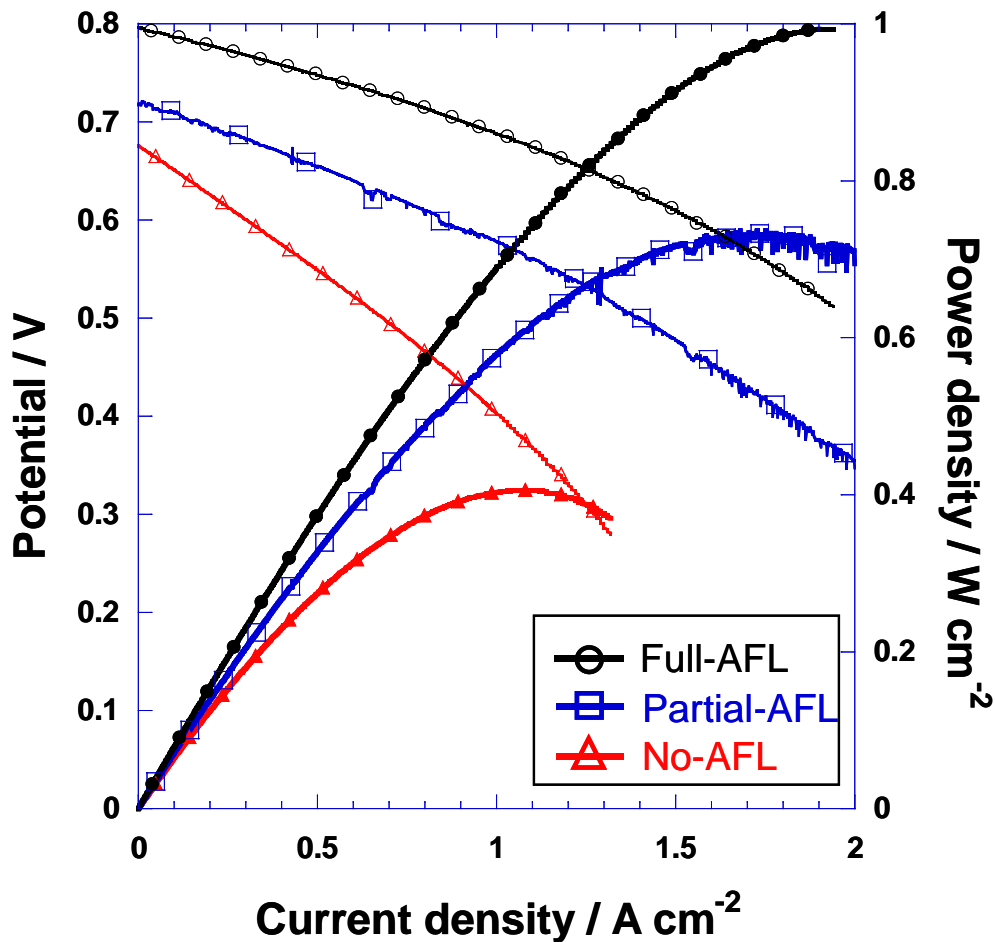


Figure 4-5. I-V characteristics of No-AFL, Partial-AFL and Full-AFL samples using 30 sccm of wet hydrogen and air at 650 °C.

Figure 4-5 shows the I-V characteristics of the No-AFL, Partial-AFL, and Full-AFL samples. All I-V measurements utilized 30 sccm of wet hydrogen on the anode side and 30 sccm of dry air on the cathode side. At 650 °C, the OCP and the maximum power density of the No-AFL sample were 0.677 V and 407 mW/cm², respectively. Despite the very low total ASR calculated from linear fit of this I-V curve (0.237 Ωcm²), the maximum power density was not high due to the low OCP value. For comparison, the total ASR from the impedance spectrum of the No-AFL sample in Figure 4-6 was 0.218 Ωcm². ASR values from both I-V and impedance measurements were comparable within 10 % for all samples.

The low OCP value of the sample without an AFL suggests that the 10 μm thick GDC fabricated by spray coating is not dense enough to block H₂ gas or electronic leakage currents. It is clear that the spray coating of the GDC electrolyte without an AFL needs improvement. However, without any changes to the spray-coated GDC, the OCP value was increased from 0.677 to 0.719 V by a partial AFL coverage at the interface, and dramatically increased from 0.677 to 0.796 V by a full AFL coverage. This gives strong evidence that the quality of the GDC electrolyte can be enhanced by using an AFL at the interface of the electrolyte and the anode. The Partial-AFL sample resulted in a maximum power density of 738 mW/cm² and the Full-AFL produced a maximum power density of 994 mW/cm² at the same temperature. This is an 81 % increase in the power density for Partial-AFL sample and a 144 % increase for Full-AFL sample. The dramatic increase in the maximum power density by application of the AFL is not only due to the increased OCP but also due to reduced total ASR.

Table 4-1. Details of No-AFL, Partial AFL and Full-AFL samples at 650 °C. The unit for ASR values is Ωcm².

	Total ASR (IV)	Total ASR (Impe.)	Ohmic ASR	Electrode ASR
No-AFL	0.237	0.218	0.104	0.114
Partial-AFL	0.130	0.128	0.062	0.066
Full-AFL	0.089	0.087	0.051	0.036

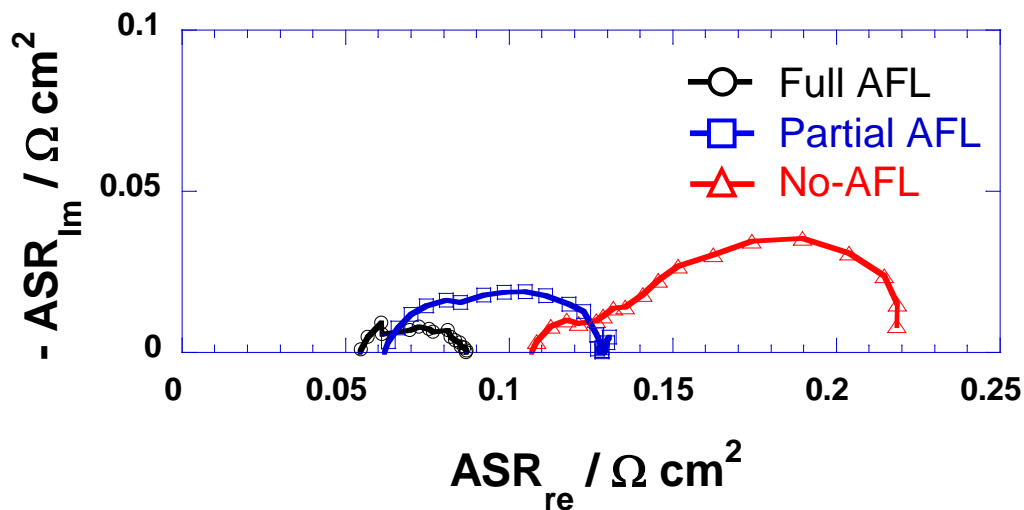


Figure 4-6. The impedance spectra of No-AFL, Partial-AFL and Full-AFL samples at 650 °C under open circuit conditions. The impedance spectra were obtained using two-point probe measurements.

The change in the ASR for the No-AFL, Partial-AFL and Full-AFL samples was further analyzed by impedance measurements (Figure 4-6). Table 4-1 shows the total, ohmic and electrode ASR values from the three samples. The No-AFL sample has a total ASR value of 0.218 Ωcm² at 650 °C. 48 % of the total ASR value is from the Ohmic ASR and 52 % is from the electrode ASR. The Partial-AFL sample had only 59% of the total ASR of No-AFL sample. This implies that a partially sprayed AFL successfully reduced the total cell ASR by 41 %. The reduction in the total ASR is due to a 41 % reduction in the Ohmic ASR and a 42 % reduction in the electrode ASR. At this point, the electrode ASR was not further separated into the cathodic and the anodic resistances due to an issue with reference electrode configurations for thin electrolytes.^{68,69} However, the difference in the electrode ASR by use of this AFL can be attributed to the difference in the anodic polarization, since an AFL will not affect the cathodic polarization.

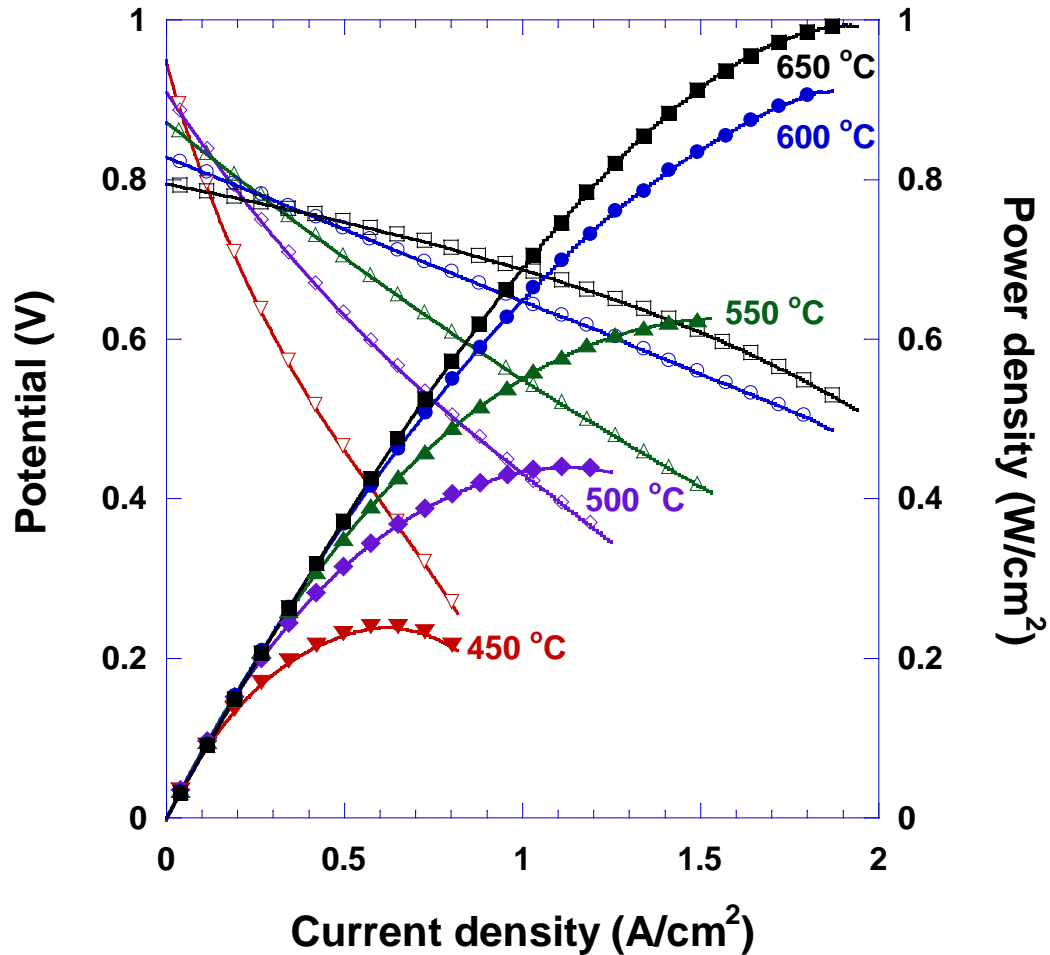


Figure 4-7. I-V characteristics of Full-AFL sample at temperatures from 450 to 650 °C using 30 sccm of wet H₂ and air.

The total ASR of No-AFL sample was reduced by 60.1 % for the sample with a fully sprayed AFL. The total ASR of Full-AFL sample was only 0.089 Ωcm² at 650 °C resulting in 994mW/cm² at the same temperature. The ohmic ASR values decreased by 51.0 % with this AFL, and the electrode ASR was reduced by 68.4 %. As expected, a large anodic polarization is occurring due to the use of large NiO particles for anode fabrication. In general the cathode polarization is considered to be the dominant contributor to the overall polarization in SOFCs. However, the fact that more than 60 % of the electrode resistance can be removed by the use of an AFL shows that depending on anode design the dominant electrode resistance can be the anode polarization for anode-supported cells.

Figure 4-7 shows the I-V behavior of Full-AFL sample at various temperatures from 450 °C to 650 °C. The OCP values are 0.796 V, 0.830 V, 0.874 V, 0.913 V and 0.950 V at 650 °C, 600 °C, 550 °C, 500 °C, and 450 °C, respectively. The maximum power densities are 994, 913, 627, 440, and 241 mW/cm² at 650 °C, 600 °C, 550 °C, 500 °C and 450 °C, respectively. The sample has a 0.49 cm² active area. In this measurement we limited gas flow-rates to 30 sccm and note that the I-V curve at 650 °C shows an increase in ASR with increasing current density. The anode shows concentration polarization at high currents even though large NiO particles were used to enhance anode porosity. The effect of gas flow-rate on the anode concentration polarization will be further discussed in this manuscript.

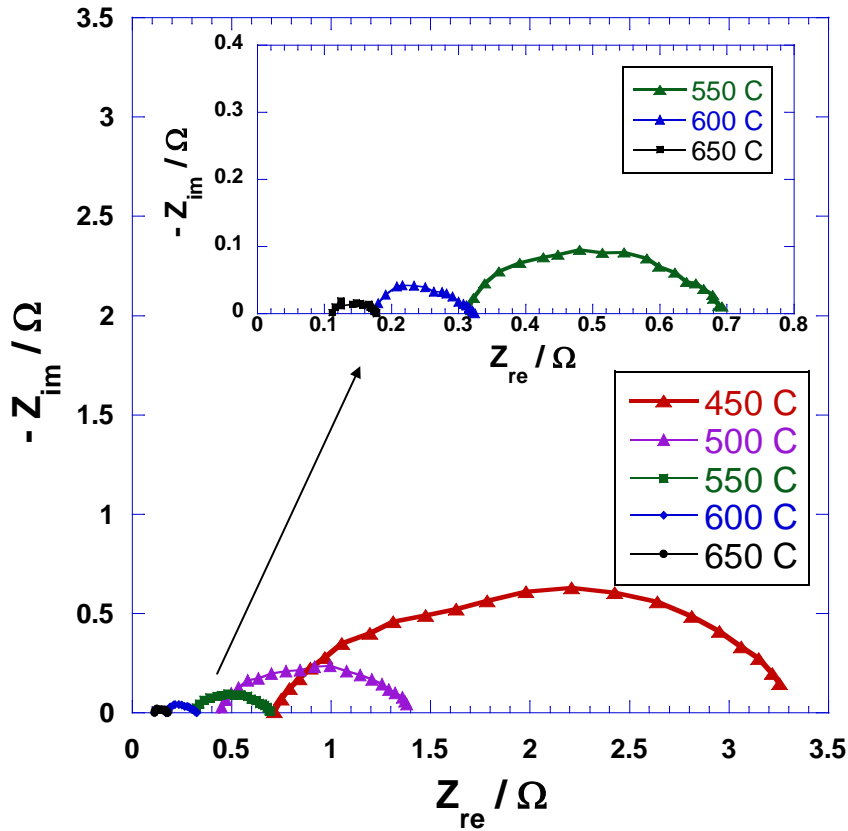


Figure 4-8. The impedance spectra of Full-AFL sample at various temperatures under operating conditions.

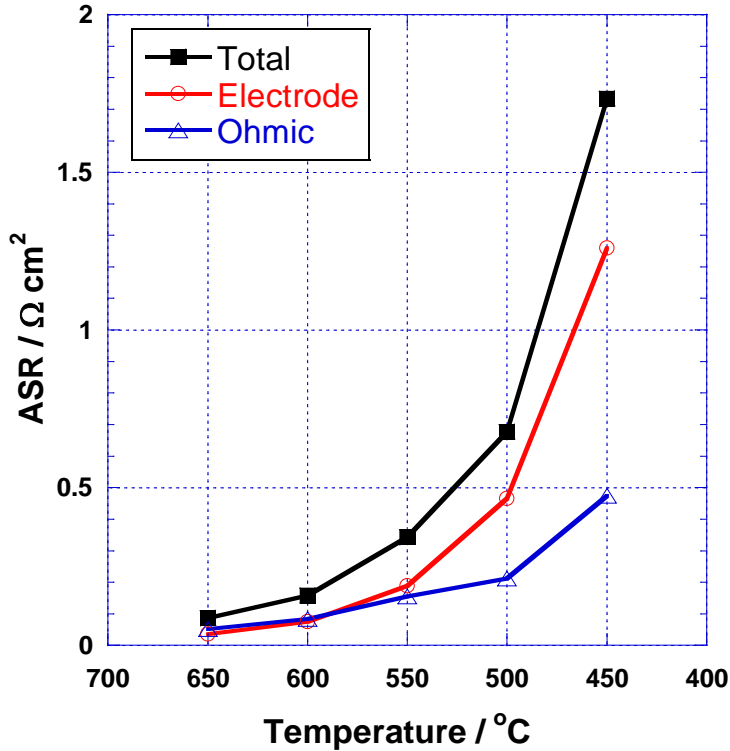


Figure 4-9. The total, electrode and ohmic ASR values calculated from impedance spectra at temperatures from 450 to 650 °C.

Figure 4-8 shows the impedance spectra at each temperature for which I-V was measured. Figure 4-9 shows the total, ohmic and electrode ASR values at various temperatures calculated from the impedance data. The ohmic and electrode ASR values were obtained from the low and high frequency intercepts of the spectra with the real axis, respectively. At 650 °C the major contributions to the total cell resistance are ohmic and electrode polarization losses. Electrode resistance from the anode and cathode constitutes 41.38 % of the total resistance. However, as temperature decreases, electrode resistance increases, and at 550 °C the electrode ASR is greater than the ohmic ASR. At 500 °C the electrode resistance is 68.79 % of the total ASR. However, the total ASR at 500 °C is still lower than 1 Ωcm², resulting in a maximum power density of 440 mW/cm². At 450 °C electrode resistance dramatically increases, constituting 72.64 % of the

total resistance of the cell. We believe this is due to the high activation energy of the oxygen reduction reaction causing higher resistance from the cathode at low temperatures.

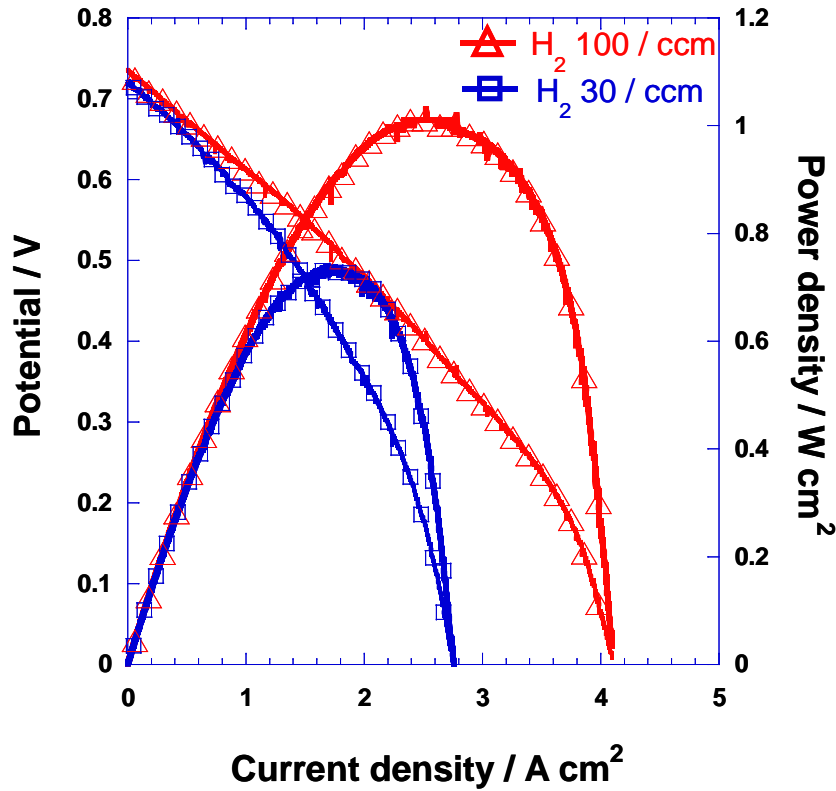


Figure 4-10. The effect of the gas flow-rate on Partial-AFL sample at 650 °C. The Partial-AFL produced 1.03 W/cm² when it is not limited to 30 sccm of gas flow-rate.

To investigate the effect of gas flow-rate on the cell performance, hydrogen and air gas flow-rates were varied from 30 to 100 sccm for Partial-AFL sample and 30 to 90 sccm for Full-AFL sample at 650 °C as shown in Figure 4-10. The Partial-AFL sample produced 738 mW/cm² at 650 °C using 30 sccm of wet hydrogen and dry air. The reason we limited gas flow-rate to 30 sccm is to compare the data with that of No-AFL sample, which was acquired using 30 sccm. Increasing wet hydrogen and dry air flow-rate to 100 sccm resulted in 1.01 W/cm² at the same temperature (Figure 4-10). Currently, many I-V results and impedance measurements from the literature are not limited to 30 sccm gas flow rates. The fact the power density and impedance

(ASR) can change by a large degree requires extra caution when comparing electrochemical properties between various cells.

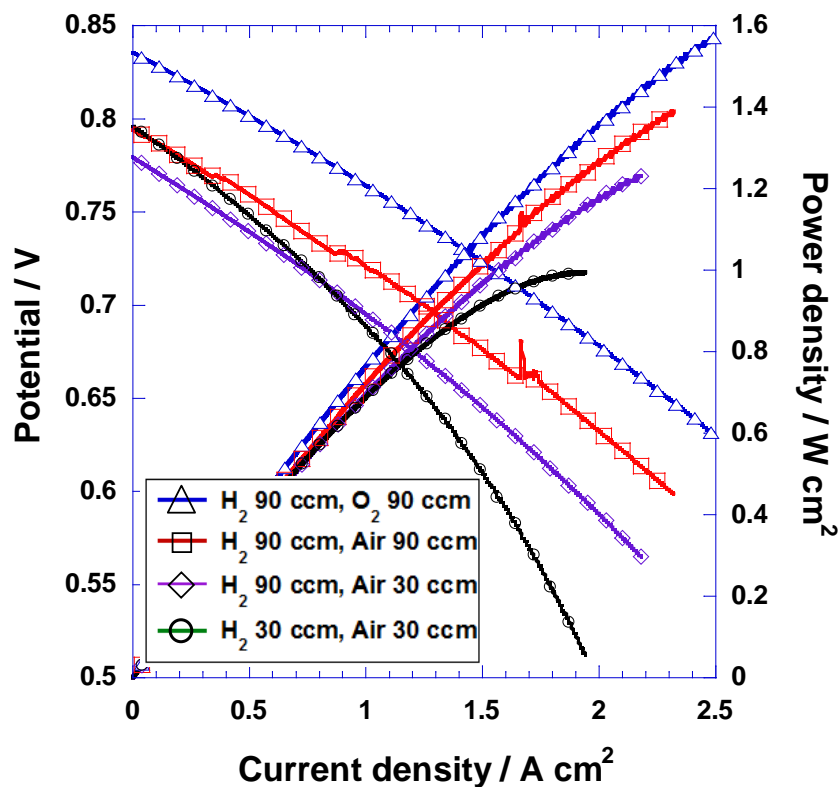


Figure 4-11. The effect of gas flow rate and gas composition on the performance of Full-AFL sample at 650 °C.

For Full-AFL sample, increasing the H₂ flow-rate to 90 sccm maintaining 30 sccm air flow led to a reduction in ASR at high currents but a decrease in open circuit potential from 0.796 to 0.779 V (Figure 4-11). The fact that asymmetric flow-rates cause a decrease in the OCP suggests that H₂ gas either leaks through the electrolyte or through the ceramabond sealant. An increase in the air flow-rate from 30 to 90 sccm increased the OCP value back to 0.796 V but did not change the slope significantly. Changing air to pure O₂ as the oxidant gas increased OCP to 0.836 V while ASR was not affected significantly. The maximum power density was increased up to 1.57 W/cm² using 90 sccm of H₂ and O₂.

4.2. Heterogeneous Functional Layers

4.2.1. Microstructural Analysis

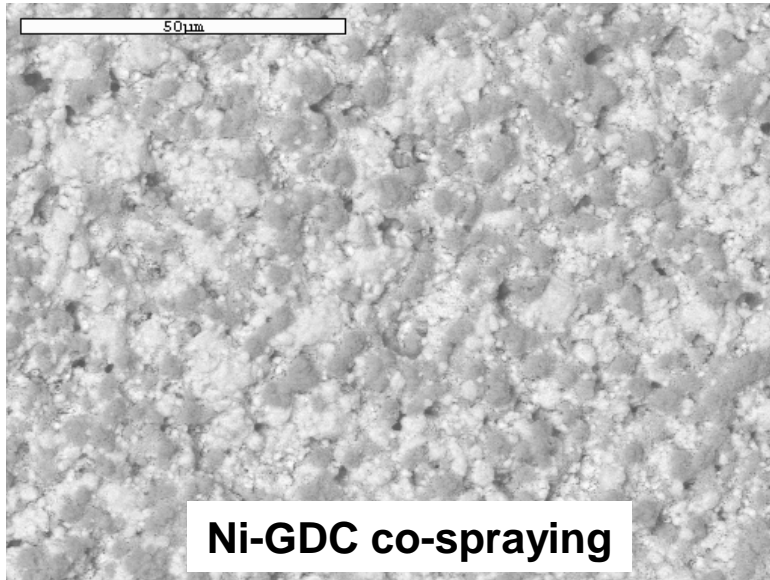


Figure 4-12. Microstructure of Ni-GDC composite AFL on NiO-GDC anode.

Three different AFLs were used in this study: a GDC functional layer (GDC AFL), a Ni-GDC functional layer (Ni-GDC AFL) and an anode functional multilayer (AFML), which is a bilayer of the GDC and Ni-GDC AFLs. Figure 4-12 shows the surface co-sprayed with Ni and GDC precursor solutions. The surface of the bare anode after presintering step and the anode surface fully covered with GDC AFL can be found in Figure 4-2. The cross section of a sample that has GDC AFL can be found in Figure 4-4. Compared to the bare anode surface, large voids on the GDC AFL sample surface are completely filled with GDC particles, providing smooth and homogeneous surface. Figure 4-12 shows that Ni-GDC AFL can provide smooth surface, but the contrast in color indicates the composition is not homogeneous.

The mass change after applying the GDC AFL was 3.4 mg/cm^2 and 2.1 mg/cm^2 for Ni-GDC AFL. A simple calculation predicts that 3.4 mg/cm^2 of GDC yields a film with $\sim 4.7 \text{ }\mu\text{m}$ thickness if 100 % dense. Though the entire surface is covered with GDC (Figure 4-2), the layer

is substantially thinner. In fact it is so thin that it is hard to estimate the thickness with cross-sectional SEM. This is because the GDC precursors penetrate the presintered anode through capillary action. Note that further spraying of the GDC precursor does not form a dense electrolyte-quality GDC layer. The data is not provided here but heavy spraying of GDC precursors only produces a porous, poor quality film. Forming a dense layer using precursor solution may provide a continuous process from an AFL to electrolyte deposition, but it is beyond the scope of this manuscript.

4.2.2. Electrochemical Performance

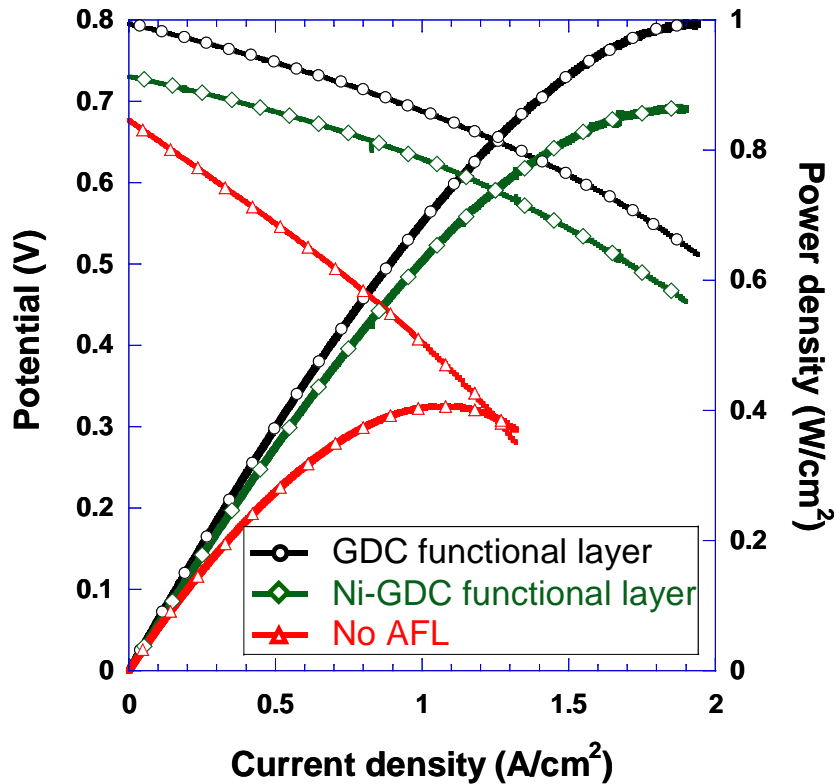


Figure 4-13. The I-V curves for the sample with no AFL, GDC AFL and Ni-GDC AFL using 30 sccm wet hydrogen and dry air at 650 °C.

Figure 4-13 shows I-V curves for samples with no AFL, GDC AFL and Ni-GDC AFL using 30 sccm wet hydrogen and dry air at 650 °C. The OCP and the maximum power density of the No-AFL sample were 0.677 V and 407 mW/cm², respectively. The OCP and the maximum

power density of the GDC AFL sample were 0.796 V and 994 mW/cm², respectively. The change in the ASR for the Ni-AFL and GDC AFL samples was further analyzed by impedance measurements.

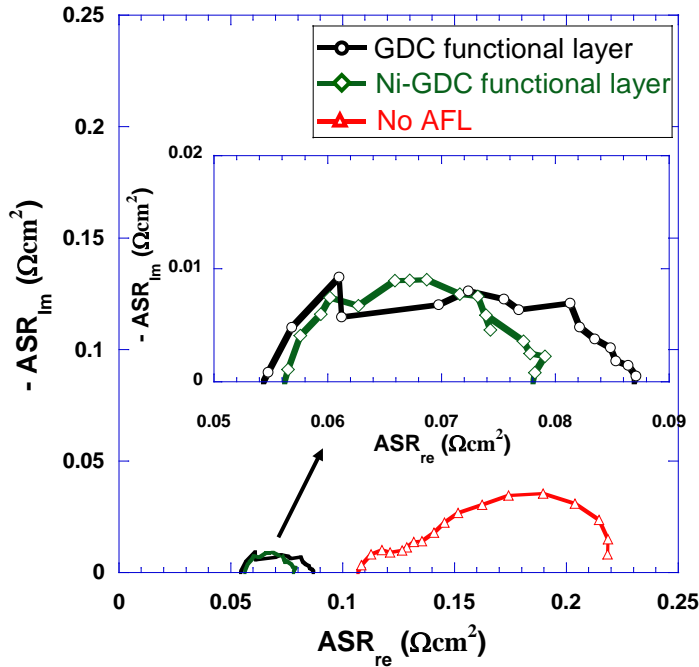


Figure 4-14. The impedance spectra under open circuit conditions at 650 °C.

Figure 4-14 shows the impedance spectra of the sample with no AFL, GDC AFL and Ni-GDC AFL under open circuit conditions at 650 °C, and Table 4-2 shows the total, ohmic and electrode ASR values calculated from the impedance data. The No-AFL sample has a total ASR value of 0.218 Ωcm². 48 % of the total ASR value of the No-AFL sample is from ohmic contributions and 52 % is from non-ohmic contributions (primarily electrode processes). The GDC AFL sample exhibited a total ASR of 0.087 Ωcm², which is 40 % of that of the No-AFL sample. This implies that the GDC AFL successfully reduced the total cell ASR by 60 %. The reduction in total ASR is due to a 51 % reduction in the ohmic ASR and a 68 % reduction in the electrode ASR. The details on GDC AFL performance can be discussed in the previous section of this dissertation, but it is notable that the GDC AFL reduces not only the electrode ASR but

also the ohmic ASR. We believe lower ohmic ASR due to an AFL support the idea of its ability to increase the OCP by improving the electrolyte quality.

Table 4-2. Summary of detailed ASR values 650 °C including Ni-GDC AFL and AFML sample.

	Total ASR _{IV}	Total ASR _{Impedance}	Ohmic ASR	Electrode ASR
No AFL	0.237	0.218	0.104	0.114
GDC AFL	0.089	0.087	0.051	0.036
Ni-GDC AFL	0.077	0.078	0.057	0.021
AFML	0.077	0.075	0.055	0.020

In theory, performance should be improved if the AFL were a composite. It is well known that the anode made with a mixture of Ni and GDC can provide larger TPB extending deeper into the bulk. However, Figure 4-14 shows the performance of the Ni-GDC composite AFL is lower than that of GDC AFL. This is not contradictory to conventional belief that the AFL should be a composite. As evidenced by the I-V curve, the lower performance was due to lower OCP value but note that in fact, the slope (the ASR) is lower for Ni-GDC AFLs. This is clear evidence that the mixture of Ni and GDC at the interface can extend TPB lengths and reduces ASR. At first this lower OCP was regarded as experimental error but repeated tests yielded reproducible results.

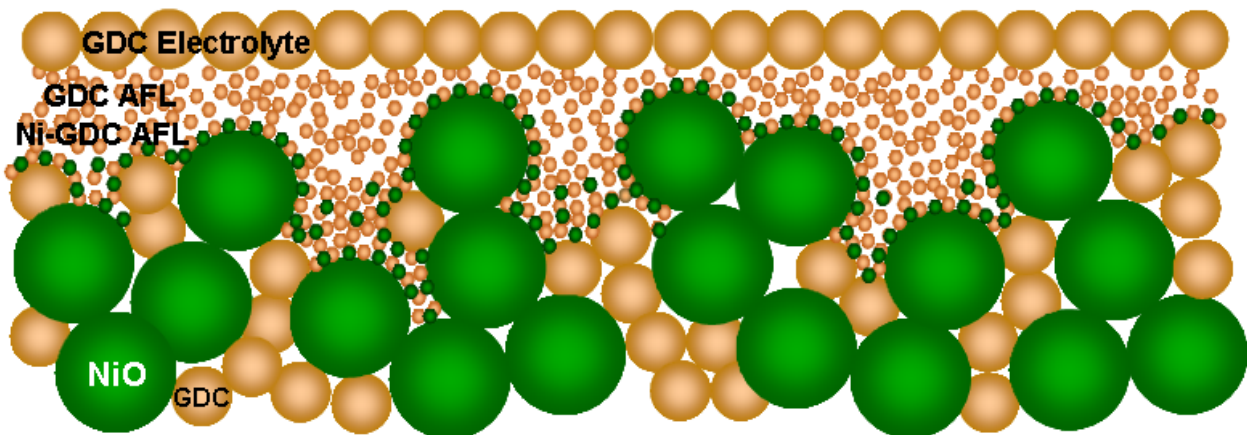


Figure 4-15. Schematics for AFL structure for Multilayer approach. Porous and rough anode surface was first covered with Ni-GDC composite AFL, followed by GDC AFL.

Impedance testing was also conducted to further investigate the ASR performance. The figure shows that the sample using a Ni-GDC AFL has a smaller total ASR mainly due to the small electrode ASR (high to low frequency intercepts). On the other hand, the difference in ohmic ASR values (high frequency intercept) for the two AFLs is relatively small. Detailed values are tabulated in Table 4-2. The composite AFL has a 42 % lower electrode ASR, while the ohmic difference is less than ~ 11 %. This means Ni-GDC AFL clearly provides a greater TPB length at the interface and therefore a lower ASR.

We believe that the GDC AFL provides a smooth and homogeneous surface for better quality GDC colloidal deposition. However, in terms of providing longer TPBs at the interface and reducing the electrode ASR, Ni-GDC composite AFL is better. One can easily infer that a combination of higher OCP of the GDC AFL and lower ASR of Ni-GDC AFL can generate even higher performance. In an effort to realize this assumption, a multilayered AFL was proposed with a Ni-GDC AFL on the anode side and a GDC AFL on the electrolyte side. In this configuration, GDC AFL provides a better surface for colloidal deposition of the electrolyte and the Ni-GDC AFL expands TPB length more at the anode surface. Figure 4-15 illustrates the idealized microstructure for this AFL near the anode/electrolyte interface. Since these precursor solutions yield nano-sized particles and very thin films, cross sectional SEM does not reveal any valuable information on the actual microstructure. However, the evidence of the bilayer existence is clear from the electrochemical performance.

Figure 4-16 shows the performance of the AFML (anode functional multilayer) in comparison with a Ni-GDC AFL sample. The I-V curves of AFML and Ni-GDC AFL samples are almost identical except for the OCP values. This indicates that the AFML sample produced a similar ASR value as the Ni-GDC AFL sample due to the TPB effect. Impedance was also

measured for the AFML sample but the semicircle is not present in this manuscript simply because it is superimposed on the semicircle of the Ni-GDC AFL sample. However, detailed ASR values calculated from the impedance data is shown in Table 4-2.

The OCP values for the GDC AFL, Ni-GDC AFL and AFML samples are 0.796 V, 0.731 V and 0.795 V respectively. The fact that the difference in OCP for the AFML sample and GDC AFL sample is negligible indicates that the ability of AFML to increase the OCP (provide better surface for colloidal coating) is comparable with that of the GDC AFL. Combining the high OCP and low ASR values, the AFML sample produced a maximum power density of 1.10 W/cm² at 650 °C. This is 10 % increase over the maximum power density of the GDC AFL sample.

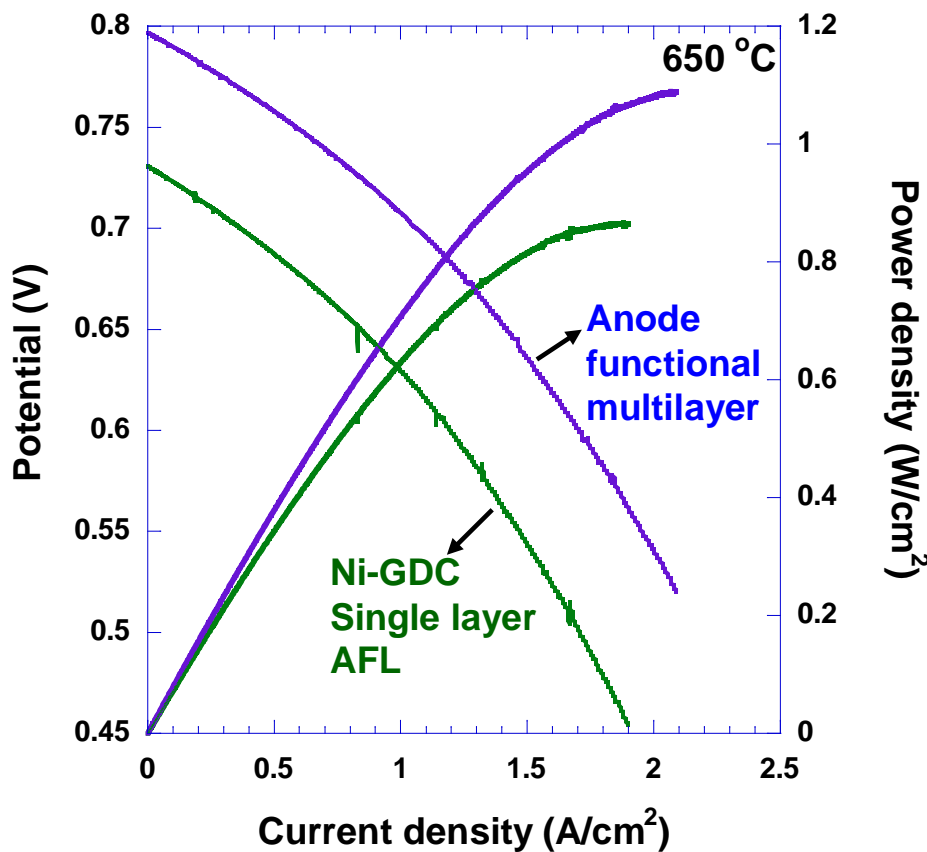


Figure 4-16. I-V curves of the sample with Ni-GDC single layer AFL and multilayered AFL using 30 sccm wet hydrogen and dry air at 650 °C.

Regarding with the fabrication of these precursor AFL, one important aspect should be noted. The pre-sintering of the AFL is crucial at this point, although it is an additional heat-treatment step. We were able to observe, during deposition of the electrolyte on the AFL without pre-sintering, the GDC slurry doesn't spread well. It seems that the GDC precursor layer without heat treatment makes the anode surface hydrophobic. The resulting GDC green body film contained large GDC aggregations scattered on surface, and remained porous after sintering. In order to eliminate the AFL pre-sintering step, further study on altering surface wettability is required.

The AFML deposition requires sequential deposition of Ni-GDC composite AFL and GDC AFL. This means 3 presintering steps are needed including anode presintering. In fact GDC AFL spray on Ni-GDC AFL without heat-treatment does not easily form a pure GDC layer covering the entire Ni-GDC surface. It seems that the hydrophobic surface caused by precursor spraying prohibits uniform spreading of another precursor solution. Fortunately, as described in the experimental section, for the AFML deposition, the Ni-GDC composite AFL was heated on a hot plate while the GDC AFL was sprayed, and that seemed to provide better GDC precursor spreading. For practical applications and reduced fabrication costs, additional heat treatment steps should be avoided, and it seems likely that precursor deposition on a precursor layer does not require high temperature heat treatment.

CHAPTER 5
CODOPED CERIA AS ALTERNATIVE ELECTROLYTES

5.1. XRD

Figure 5-1 shows the XRD profile of the calcined powder of $\text{Sm}_{0.075}\text{Nd}_{0.075}\text{Ce}_{0.85}\text{O}_{2-\delta}$ taken at room temperature. The powder is phase pure with cubic fluorite structure. The best estimate of the lattice constant (a_0) was calculated using the least-squares extrapolation method.⁷⁰ The lattice parameter of $\text{Sm}_{0.075}\text{Nd}_{0.075}\text{Ce}_{0.85}\text{O}_{2-\delta}$ synthesized using co-precipitation technique was $5.4340 \pm 0.0017 \text{ \AA}$. The estimated lattice parameter value is close to the value (5.4351 \AA) obtained from the lattice parameter (a) and dopant concentration (x) relationship for $\text{Sm}_x\text{Nd}_x\text{Ce}_{1-x}\text{O}_{2-\delta}$ presented elsewhere by Omar et al.³⁶

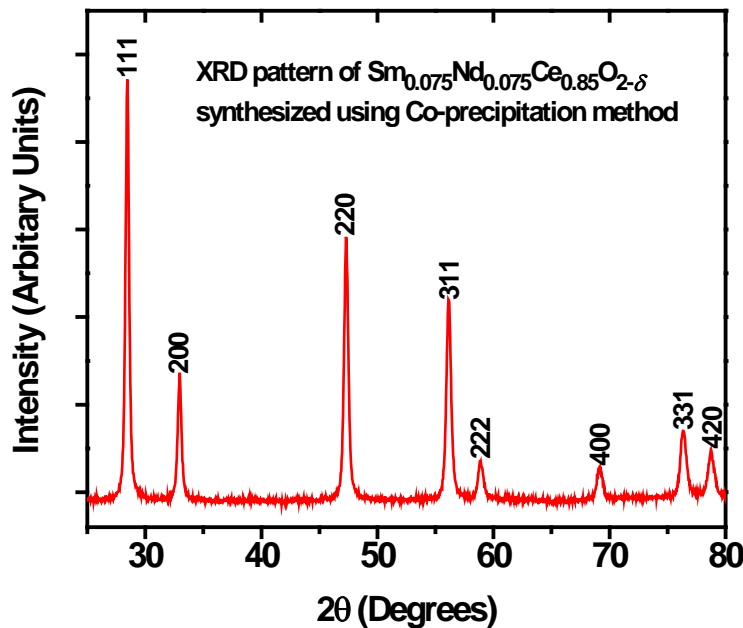


Figure 5-1. XRD pattern of $\text{Sm}_{0.075}\text{Nd}_{0.075}\text{Ce}_{0.85}\text{O}_{2-\delta}$ synthesized using co-precipitation technique.

5.2. Particle Size

Figure 5-2 shows the particle size distribution of the $\text{Sm}_{0.075}\text{Nd}_{0.075}\text{Ce}_{0.85}\text{O}_{2-\delta}$ and the commercially obtained LSCF powders. The particle size distribution of the phase pure $\text{Sm}_{0.075}\text{Nd}_{0.075}\text{Ce}_{0.85}\text{O}_{2-\delta}$ powder synthesized using co-precipitation technique was measured

using a Beckman Coulter LS13320 particle size analyzer. The particle size distribution of LSCF powder is provided by the company. In order to achieve high density ceramic electrolyte, it is desired that the particle size should be less than 1 μm with particle size distribution to be narrow and monodisperse. It can be seen that the $\text{Sm}_{0.075}\text{Nd}_{0.075}\text{Ce}_{0.85}\text{O}_{2-\delta}$ particles exhibit size less than 1 μm , with the mean size (d_{50}) of 0.095 μm . Further, the particle size distribution is also monodisperse.

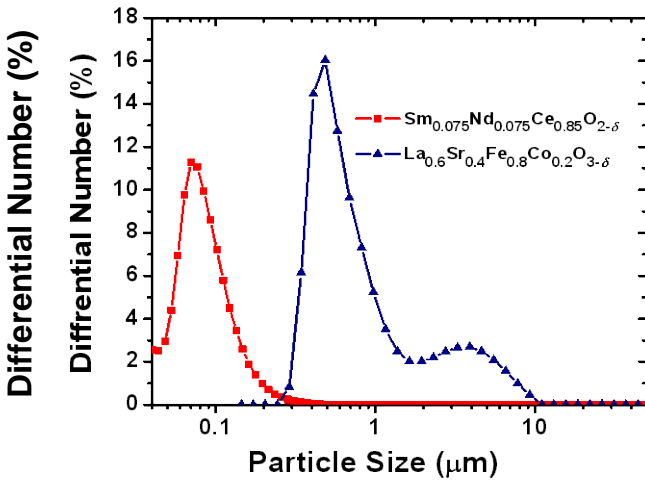


Figure 5-2. Particle size distribution of $\text{Sm}_{0.075}\text{Nd}_{0.075}\text{Ce}_{0.85}\text{O}_{2-\delta}$ synthesized using co-precipitation technique and $\text{La}_{0.6}\text{Sr}_{0.4}\text{Co}_{0.2}\text{Fe}_{0.8}\text{O}_{3-\delta}$ (obtained from Praxair Specialty Ceramics).

The GDC powder obtained from Rhodia comprised of very fine particles of size less than 100 nm.⁵⁴ On the other hand, the NiO particles are mostly micron-sized.⁵⁴ Large particles of NiO, after reduction in H_2 , results in the porous anode. This is essential for the rapid fuel delivery to the reaction sites (i.e., triple phase boundaries of electrolyte, electrode, and air), and efficient water molecule removal. The LSCF powder used for the cathode exhibit the number

particle size distribution which is bi-modal, with most of the particles around 1 μm in size (shown in Figure 5-2).

5.3. Microstructural Analysis

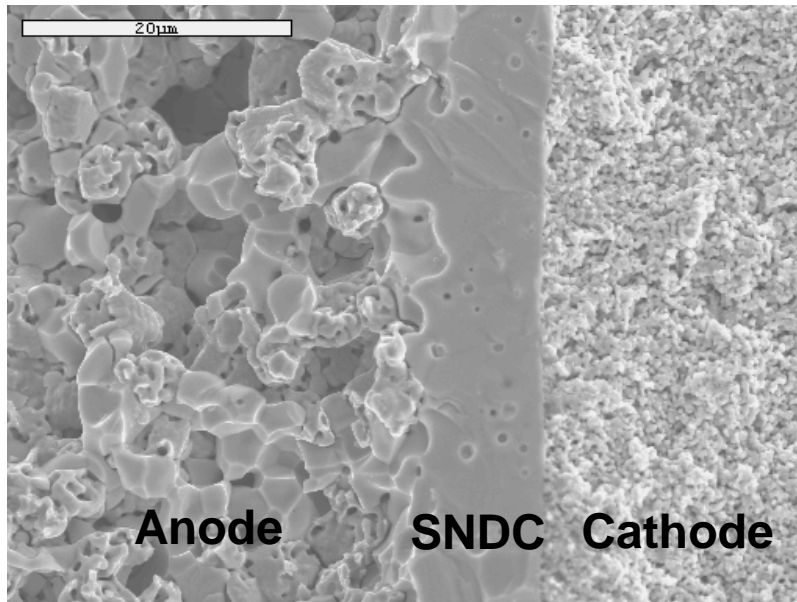


Figure 5-3. FE-SEM images of the cross-section view of the electrodes and electrolyte after operation.

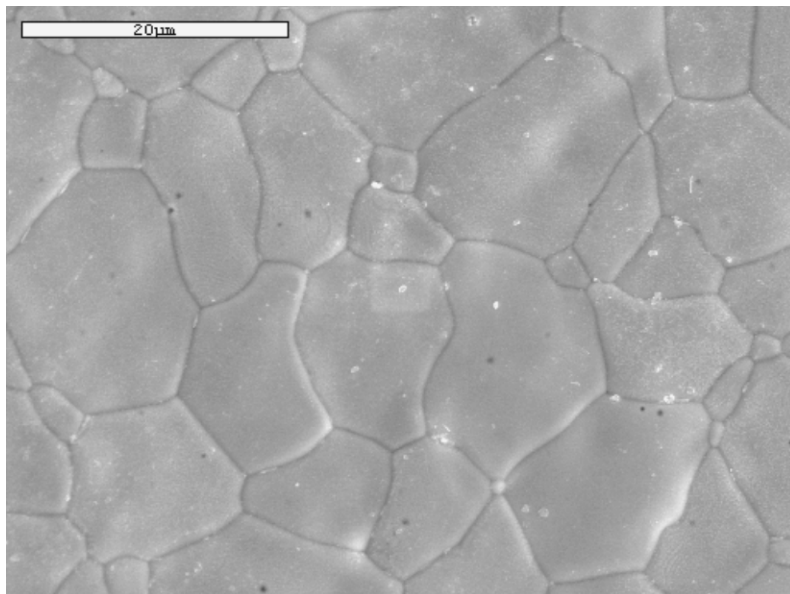


Figure 5-4. FE-SEM image of the surface of the SNDC electrolyte after operation.

Figure 5-3 shows the microstructure of the cross-section of the fuel cell sample, and Figure 5-4 shows the surface of $\text{Sm}_{0.075}\text{Nd}_{0.075}\text{Ce}_{0.85}\text{O}_{2-\delta}$ electrolyte. It can be seen both in the cross-sectional and surface micrographs that the electrolyte is densely sintered except for a few isolated residual pores. From the SEM image, while irregular, the thickness of the SNDC electrolyte is estimated to be $\sim 10 \mu\text{m}$. This suggests that the SNDC electrolyte can be easily deposited with ceramic processes such as colloidal deposition.

Further, the nickel (reduced form of NiO) particles in the anode are large compared to LSCF particles in the cathode. This is mainly due to the large particle size of the NiO starting powder. Although, the hydrogen oxidation in the anode side is kinetically more favorable than oxygen reduction in the cathode side, the significantly large particle size of the Ni near the electrolyte and anode interface can cause high anodic activation polarization at low temperatures. We have previously demonstrated that the anode polarization can be significantly lowered using an AFL between anode and electrolyte layers.^{13,15} In this work, the AFL which can reduce the additional anode polarization caused by the use of large NiO powder was employed. Details on the change in the microstructure for the same anode support using AFL can be found in the previous chapter and elsewhere.^{54,55}

5.4. Power Density

Figure 5-5 shows the I-V characteristics of the SOFC with $\text{Sm}_{0.075}\text{Nd}_{0.075}\text{Ce}_{0.85}\text{O}_{2-\delta}$ electrolyte at temperatures ranging from 500 °C to 650 °C. The OCP values obtained were 0.86, 0.89, 0.93 and 0.96 V at 650 °C, 600 °C, 550 °C and 500 °C, respectively. The obtained OCP values were higher than previous typical OCP values achieved in the cell with GDC as an electrolyte, using similar fabrication route and the same experimental setup (0.8 V at 650 °C).^{54,55}

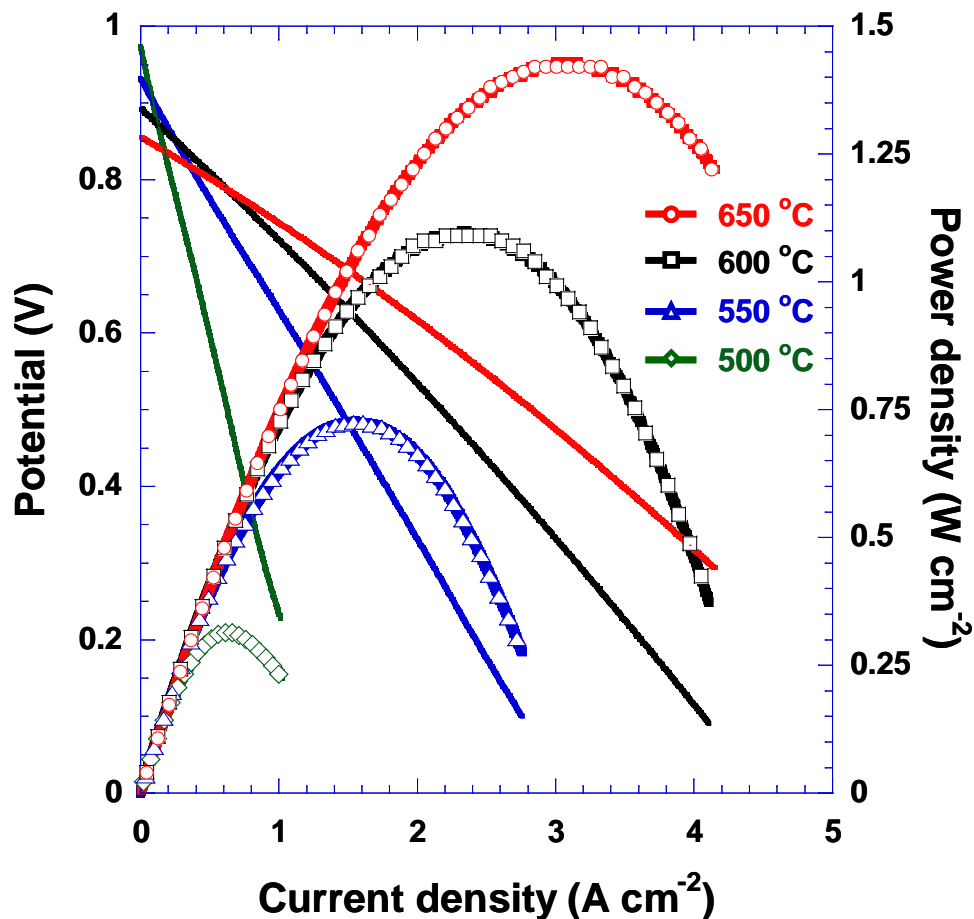


Figure 5-5. The I-V characteristics of the prototype SOFC sample with $\text{Sm}_{0.075}\text{Nd}_{0.075}\text{Ce}_{0.85}\text{O}_{2-\delta}$ electrolyte at various temperatures ranging from 500 to 650 °C in 90 sccm of both dry air and wet hydrogen.

Figure 5-5 also shows the power density as a function of current density. The maximum power densities achieved in the test cell were 1.43, 1.10, 0.73 and 0.32 W/cm^2 at 650 °C, 600 °C, 550 °C, and 500 °C, respectively. For the intermediate temperatures, the obtained power densities were exceptionally high and higher than those obtained from the SOFC samples with 10 μm thick GDC electrolyte (1 W/cm^2 at 650 °C). This could be due in part to the high ionic conductivity of $\text{Sm}_{0.075}\text{Nd}_{0.075}\text{Ce}_{0.85}\text{O}_{2-\delta}$ electrolyte. However, it is important to note that the I-V characteristics and the maximum power density of the SOFC is a function of numerous processing and material variables. For this reason, the potential of $\text{Sm}_{0.075}\text{Nd}_{0.075}\text{Ce}_{0.85}\text{O}_{2-\delta}$

electrolyte cannot be directly compared with that of GDC using I-V characteristics. Comparison between the ionic conductivity of $\text{Sm}_{0.075}\text{Nd}_{0.075}\text{Ce}_{0.85}\text{O}_{2-\delta}$ and GDC electrolyte is reported elsewhere.^{29,36} However, the performance testing results clearly suggest that the $\text{Sm}_{0.075}\text{Nd}_{0.075}\text{Ce}_{0.85}\text{O}_{2-\delta}$ electrolyte material can successfully generate high power density in SOFCs operating in the intermediate temperature range.

5.5. Impedance Analysis

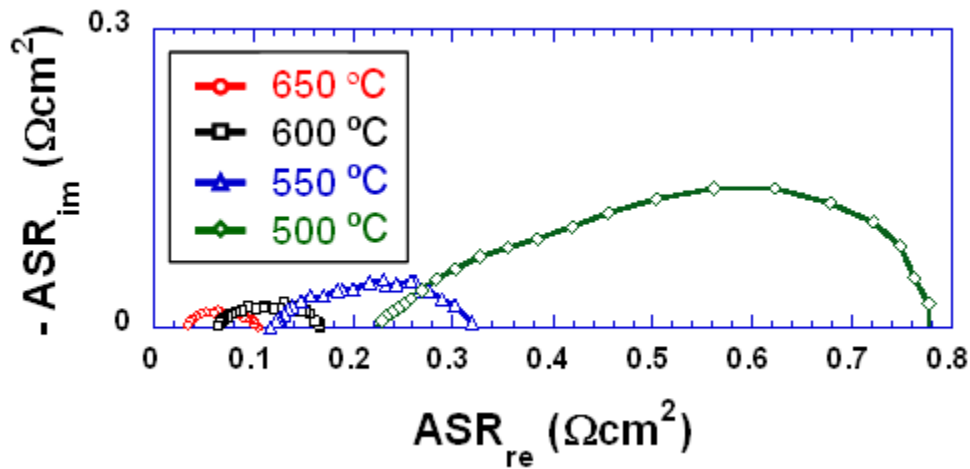


Figure 5-6. Impedance spectrum of the SOFC cell measured at various temperatures ranging from 500 to 650 °C.

Figure 5-6 shows the impedance spectrum of the SOFC at 650 °C, 600 °C, 550 °C and 500 °C. Using impedance spectroscopy, it is possible to separate out the electrode and ohmic contributions to the total ASR value at each temperature. From the high frequency intercept of the impedance spectrum with the real axis, the ohmic ASR value was calculated (after normalizing the resistance to the cathode area of 0.48 cm^2). Electrode ASR was determined from the difference between the low and high frequency intercepts (also after normalizing the resistance to the cathode area). Figure 5-7 shows the electrode and the ohmic ASR values separated from the total ASR at different temperatures. The rapid increase in the total ASR with decreasing temperature is mainly due to the significant increase in the electrode polarization.

This increase in electrode polarization is most likely due to the cathode reaction which is a thermally activated process.⁷¹ In contrast, ohmic ASR values remain relatively small even at lower temperatures.

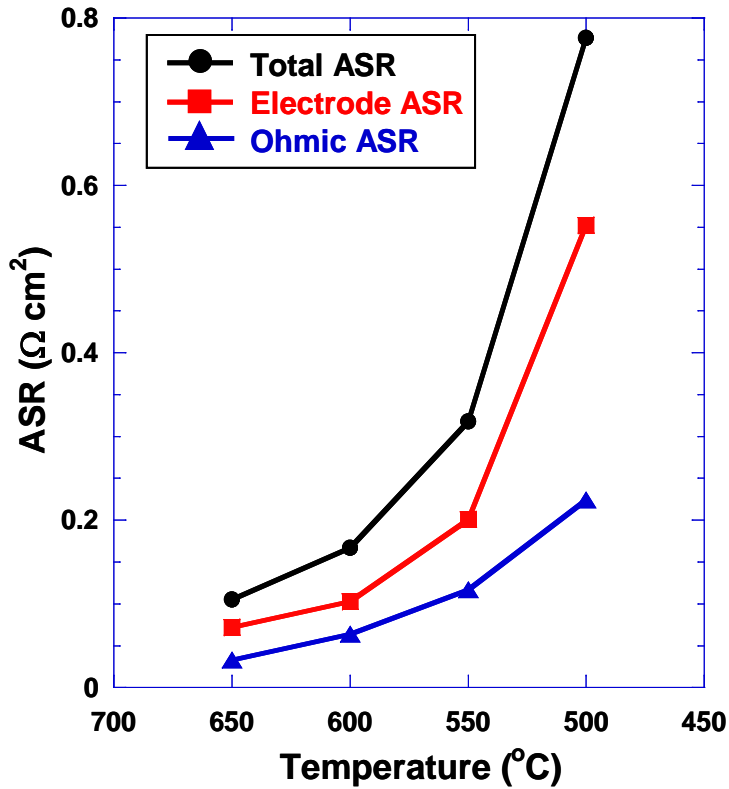


Figure 5-7. ASR values at various temperatures

The total ASR values were also calculated from the gradient of the linearly fitted I-V curves. Table 5-1 shows the comparison between the total ASR values obtained from the impedance measurements and I-V characteristics. Impedance measurements were done under open circuit condition, therefore, while fitting the I-V curve, the region near zero current (0 – 0.2 A/cm²) was taken into account. Both ASR values from the I-V characteristics and the impedance measurement are comparable at all temperatures.

The ohmic and electrode ASR values separated from the total ASR at each temperature are also presented in Table 5-1. At 650 °C the ohmic contribution to the total ASR is 31 %.

With decreasing temperature the ohmic ASR percentage contribution remains relatively small. At 500°C, the ohmic contribution towards the total ASR value is reduced to 29 %. It is obvious that further improvement in the performance of this fuel cell can be done by reducing the electrode ASR especially for lower operating temperatures.

Table 5-1. Comparison between the total ASR obtained from I-V characteristic and impedance measurement. The ohmic contribution towards the total ASR is also shown.

Temperature (°C)	ASR _{I-V} (Ωcm^2)	ASR _{Impedance} (Ωcm^2)	ASR _{Electrode} (Ωcm^2)	ASR _{Ohmic} (Ωcm^2)
650	0.106	0.105	0.072	0.033
600	0.166	0.167	0.103	0.064
550	0.323	0.318	0.201	0.117
500	0.783	0.776	0.552	0.224

We believe the electrode ASR is mostly cathode ASR at this point by following reasons: First, the high activation energy of the oxygen reduction reaction results in higher resistance from the cathode at low temperatures. Secondly, with the recently-developed novel AFL, the anode polarization from hydrogen oxidation reaction caused by use of relatively large particles of Ni at the anode-electrolyte interface is effectively removed by 60 %. However, due to the limitation of the two-point impedance measurement, it is difficult to deconvolute the contribution from each of the electrodes.

It is also well known that introducing a highly ionic conducting phase in an electrode composite also enhances the performance of SOFCs.³⁵ Since $\text{Sm}_{0.075}\text{Nd}_{0.075}\text{Ce}_{0.85}\text{O}_{2-\delta}$ exhibits higher ionic conductivity than GDC, it is expected that replacing GDC with $\text{Sm}_{0.075}\text{Nd}_{0.075}\text{Ce}_{0.85}\text{O}_{2-\delta}$ will further improve SOFC performance and is the subject of future work.

CHAPTER 6
ESB/GDC BILAYER ELECTROLYTE FOR IT-SOFC

6.1. Co-pressing Procedure

It has been demonstrated that a YSZ electrolyte and LaSrMgO_3 cathode can generate the maximum power density of 2 W/cm^2 at $800 \text{ }^\circ\text{C}$.⁵ This chapter is dedicated to reproduction of the same level power densities at IT ranges.

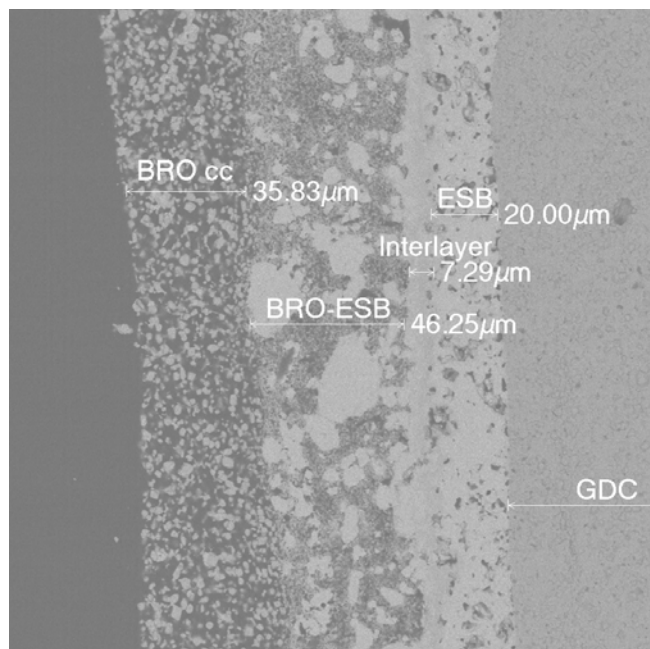


Figure 6-1. Back scattered image showing the cross-section of the GDC (50 μm) and ESB (20 μm) bilayer electrolyte with BRO7-ESB composite cathode and Ni-GDC anode after cell testing. BRO_{cc} refers to a pure $\text{Bi}_2\text{Ru}_2\text{O}_7$ current collector.

Figure 6-1 shows the microstructure of the co-pressed sample. Great effort was made to reduce the thickness of the electrolyte while spreading GDC powder on NiO-GDC anode support for higher performance. However, the minimum thickness obtained by co-pressing route was $\sim 50 \mu\text{m}$. Also, as seen in the Figure 6-1, the thickness of GDC throughout the cell is not uniform. This is one limitation of the co-pressing method used for this study. Electrolyte uniformity can be improved by spray coating GDC onto the anode support prior to pressing, distributing a thin

layer of GDC particles across the surface.⁶ Alternatively, foamy GDC powder can be used to better control GDC thickness while spreading across the surface.⁷² However, in this work, the co-pressing approach was not further studied as it is not suitable for mass production. Rather, it was used for proof-of-concept purposes. More practical SOFC fabrication routes involving tape-cast anodes and thin electrolyte deposition is discussed later in this article.

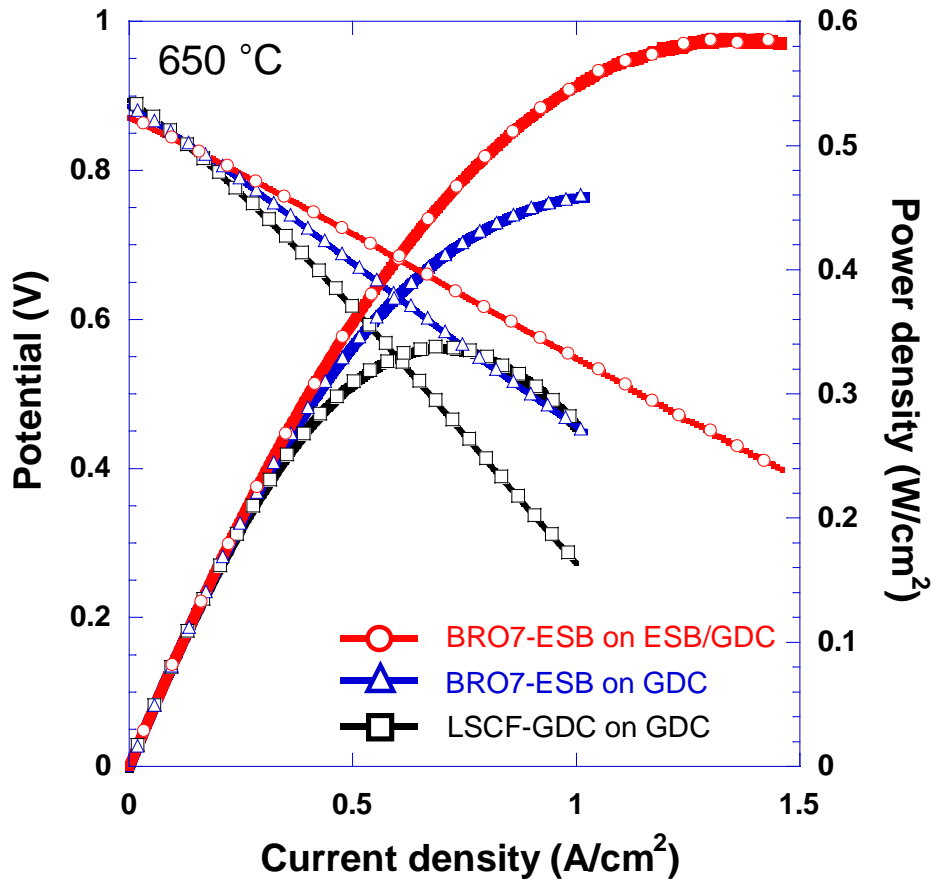


Figure 6-2. I-V characteristics of three co-pressed samples at 650 °C using 30 sccm of wet hydrogen and dry air. The result shows that BRO7-ESB cathode has lower ASR than LSCF-GDC cathode on a single layer GDC electrolyte. The performance of the BRO7-ESB cathode was further improved by using a bilayer electrolyte resulting in 588 mW/cm².

Figure 6-1 reveals that ESB layer is porous while co-pressed GDC is very dense. The porous nature of the ESB layer is a result of the screen printing of coarse powder synthesized by the solid state process. The ESB layer thickness was ~20 μm, resulting in a total bilayered

electrolyte thickness greater than 70 μm . Hence a substantial portion of the total cell resistance is expected to be attributable to the electrolyte ohmic resistance.

The results of current-voltage testing at 650 $^{\circ}\text{C}$ are shown in Figure 6-2 as well as in Table 6-1. Figure 6-2 shows that BRO7-ESB performs better than LSCF-GDC composite cathode on the same GDC electrolyte. The total cell ASR and maximum power density is 0.43 Ωcm^2 and 460 mW/cm^2 for BRO7-ESB and 0.62 Ωcm^2 and 338 mW/cm^2 for LSCF-GDC, respectively. Since the anode supports and the electrolytes were all prepared at the same time, resistances due to the anode and electrolyte are expected to be similar for both cells, so the improvement can be attributed mainly to the cathode.

Table 6-1. Details of co-pressed cell.

Cell Type	OCP (V)	ASR (Ωcm^2)	Maximum Power Density (W/cm^2)
LSCF-GDC on GDC	0.91	0.62	338
BRO7-ESB on GDC	0.90	0.43	460
BRO7-ESB on ESB/GDC	0.87	0.32	588

The cell utilizing a bilayer electrolyte had significantly better performance compared with the other cells - 588 mW/cm^2 maximum power density and 0.32 Ωcm^2 ASR - despite the added resistance caused by inserting an ESB layer between the GDC and the cathode. This is partly due to a degree of catalytic activity present at the surface of the ESB electrolyte, and the role the cathode/electrolyte interface plays in the cathode resistance, as discussed previously.⁴⁴⁻⁴⁸

This co-pressing study demonstrated that lower ASRs can be achieved using BRO7-ESB cathodes and using bilayer electrolytes. However, an increase in OCP for the bilayer sample was not observed. This should not be an undermining result to the bilayer concept. A series of studies have already shown that an ESB layer can increase the low GDC OCP.^{8,40-42} Note that these studies were all conducted using thick GDC pellets and thick layers of ESB, which can block leakage current relatively easily. The main reason for the low bilayer OCP can be seen in the

microstructure. As seen in Figure 6-1, the screen printed ESB layer didn't produce a dense membrane. Porous ESB requires higher thickness to block electronic leakage current from GDC and even with a thickness of 20 μm , the ESB layer could not accomplish this. The next section discusses ESB synthesis by co-precipitation in order to reduce particle size and thus reduce porosity.

Further, there may be some stability issues at this temperature as post-mortem SEM analysis reveals formation of an interlayer between the cathode and the ESB layer (Figure 6-1). The nature and formation mechanism of this interlayer is not known at present, and may likely also be due to the porous nature of the ESB layer as an interlayer was not observed for samples with more dense ESB layers, discussed below. It is clear that these cathodes have potential for use in lower temperature SOFCs. We emphasize that the bilayer electrolyte increased the maximum power density by 74% and lowered the ASR by 49%.

6.2. Colloidal Route

Co-pressing produced high OCP (~ 0.9 V) due mostly to high GDC density and thickness. However, co-pressing is not a practical fabrication route. To overcome the limitations of co-pressing, spray coating of GDC onto tape-cast anode substrates was performed. This process reduced the entire sample thickness from 2~3 mm to ~ 400 μm . GDC electrolyte thickness was controlled to 10 ~ 20 μm . According to Kim et al.,⁶³ a thick anode support frequently exhibits high anode concentration polarization. Reduction in thickness significantly reduces ASR resulting in higher power density. Details on tapecasting anode and GDC electrolyte deposition have already been described.⁶⁷

Figure 6-3 shows the GDC thickness is ~ 20 μm . Due to the mixed ionic-electronic conducting behavior of ceria electrolytes the OCP decreases as thickness decreases.⁶² Therefore,

the OCP of this cell is only 0.68 V (Figure 6-5) compared to 0.91 V with the co-pressed sample under same conditions.⁵⁵

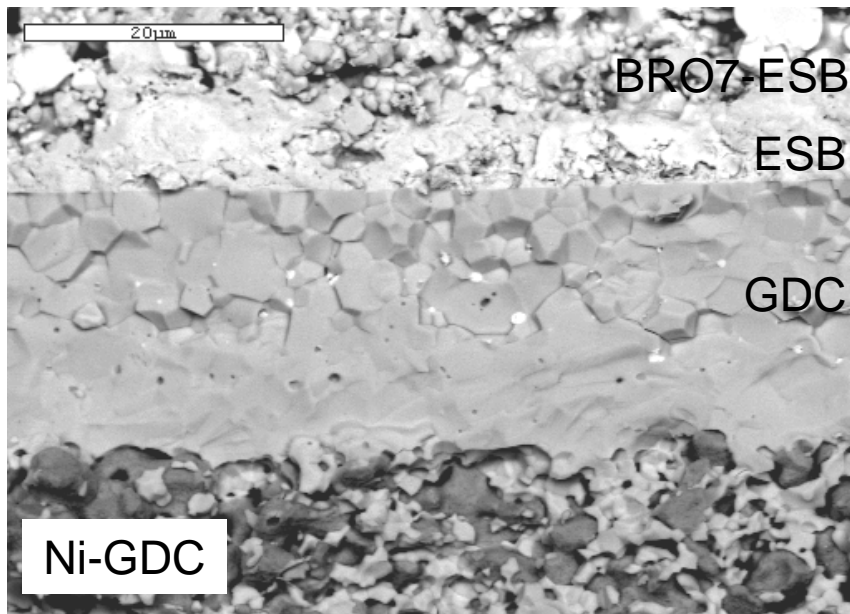


Figure 6-3. Backscatter image of the cross-section of the bilayer sample produced by colloidal deposition. Note that there is the unclear interface between the BRO7-ESB cathode and the ESB layer.

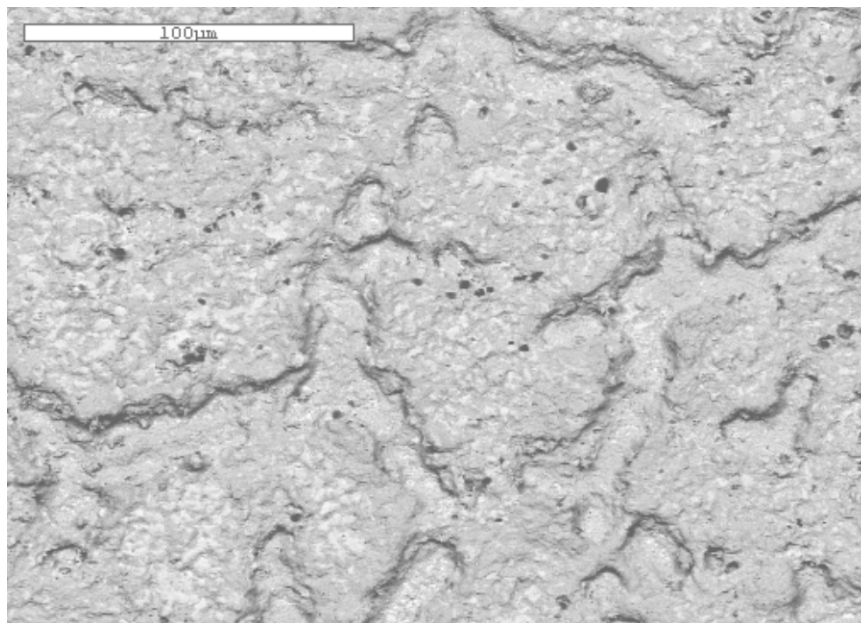


Figure 6-4. Backscatter images of bilayer samples showing the surface view of the ESB layer produced by colloidal deposition. Note the high degree of roughness and porosity of the ESB layer.

Figure 6-4 shows the surface microstructure of ESB deposited on the GDC. Note that the magnifications are different. The ESB surface is rough and porous. At this point it is clear that further improvement in ESB deposition is required. However, we present this preliminary co-precipitation ESB study because the result shows the nature of the bilayer electrolyte.

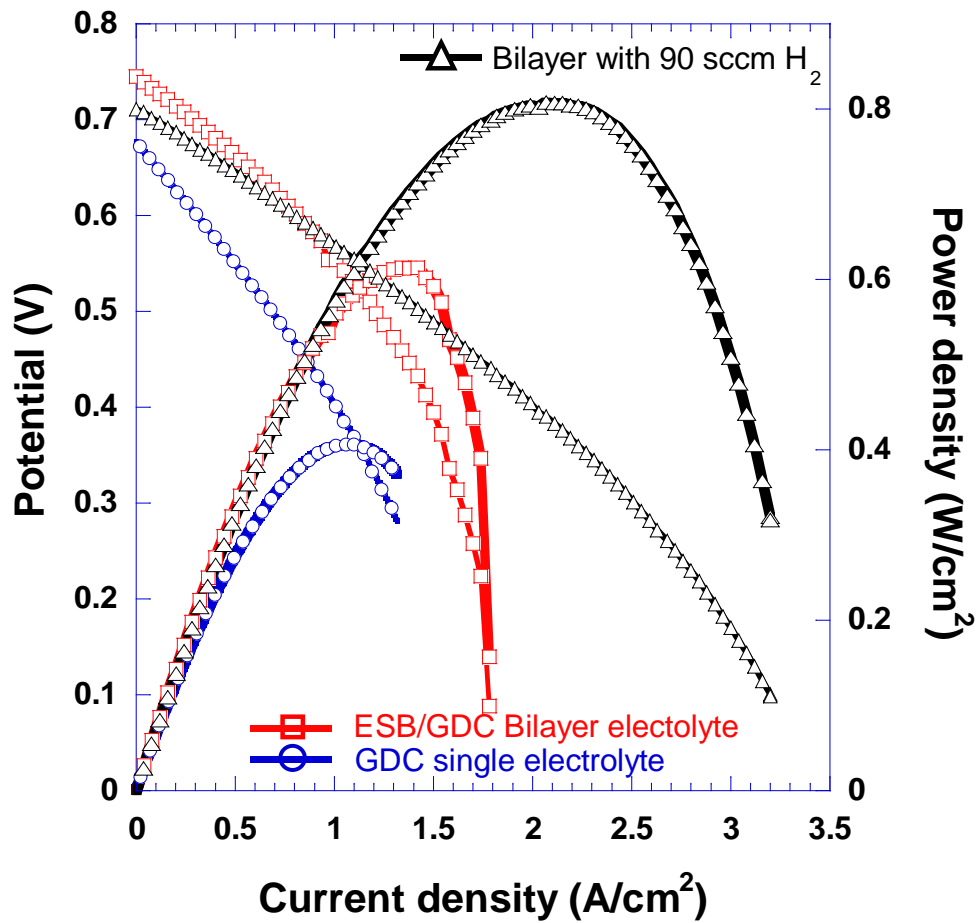


Figure 6-5. The I-V characteristics of the samples with GDC single layer and ESB/GDC bilayer electrolyte at 650 °C. The bilayer electrolyte improved the maximum power density from 407 to 614 mW/cm² using 30 sccm of air and wet hydrogen. The maximum power density of the bilayer sample was further improved to 808 mW/cm² using 90 sccm of wet hydrogen. The Lower OCP of 90 sccm sample is due to asymmetric flow-rate; the air flow-rate was maintained at 30 sccm.

At 650 °C the single layer SOFC resulted in 407 mW/cm² even though spray-coated GDC produced low OCP (Figure 6-5). High flow rates can substantially improve cell performance (~200 sccm are frequently used.), so care must be used with comparing cell ASR and maximum

power density values. Considering the low gas flow-rate of 30 sccm this result is quite good, and the low ASR ($0.237 \Omega\text{cm}^2$) can be attributed to reduced electrolyte and anode thicknesses.

The ESB/GDC bilayer was prepared and tested at this stage, and was shown to successfully blocked some portion of electronic conduction resulting in a higher OCP of 0.75 V (Figure 6-5). Considering the fact that ESB is almost a purely ionic conductor⁷³ the bilayer OCP is still low. However, the 0.07 V increase in OCP is significant and supports the bilayer concept.

With increased OCP the bilayer electrolyte sample resulted in a maximum power density of 614 mW/cm^2 . This 51 % increase in the maximum power density is not only due to higher OCP but also due to the lower ASR. Though the GDC electrolyte used for bilayer sample ($\sim 20 \mu\text{m}$) was thicker than that for the single layer GDC sample by $10 \mu\text{m}$, the I-V curve shows that the bilayer cell exhibits a lower ASR resulting in higher performance using a BRO7-ESB cathode. As seen in Figure 6-5, when H_2 flow-rate was increased to 90 sccm (air was maintained at 30 sccm), the maximum power density and the ASR was 808 mW/cm^2 and $0.133 \Omega\text{cm}^2$, respectively. Note that the asymmetric flow-rate to the cathode and the anode resulted in lower a lower cell OCP, indicating an external gas leak.⁵⁵

Table 6-2. Details of tapecast cell without AFL.

Cell Type	OCP (V)	ASR (Ωcm^2)	Maximum Power Density (W/cm^2)
GDC single layer	0.68	0.237	407
ESB(colloidal)/GDC	0.75	0.158	614

Table 6-2 summarizes the preliminary results obtained by colloidal deposition of ESB prepared by co-precipitation. The bilayer showed a 0.07 V increase in the OCP and a 33 % decrease in the ASR resulting in a 51 % improvement in maximum power density. Though these results are promising, the microstructure of ESB shows that further improvements in film

deposition are required. Therefore, an alternate deposition technique, PLD, was employed to confirm that bilayer electrolytes can produce high performance.

6.3. Cold PLD

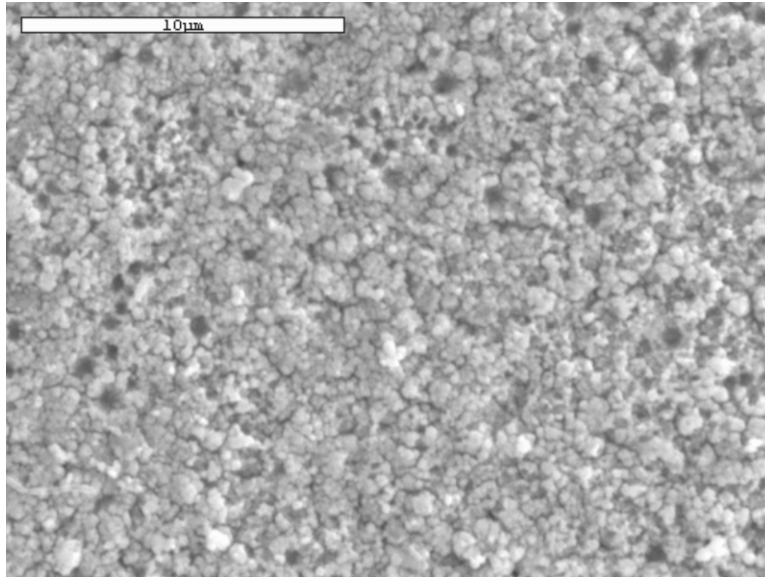


Figure 6-6. As-deposited ESB layer on the GDC electrolyte.

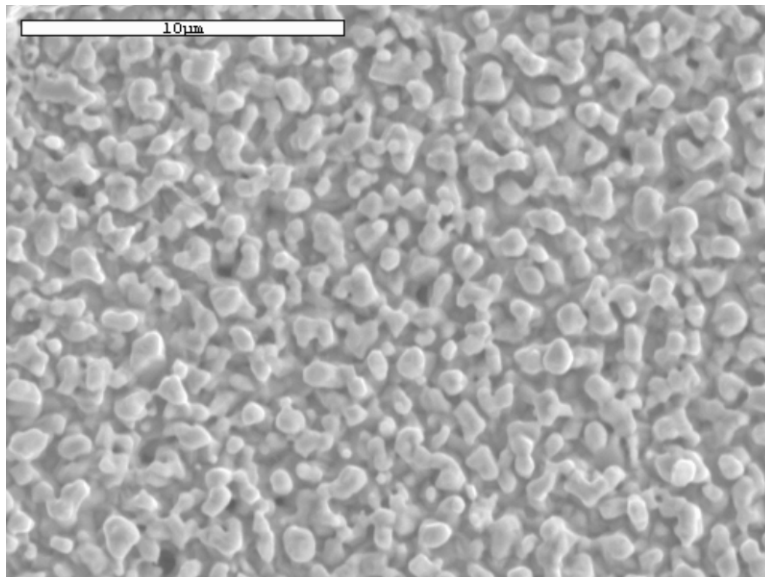


Figure 6-7. ESB layer after heat treatment at 700 °C for 4h.

Figure 6-6 shows the as-deposited ESB layer on sintered GDC layer. As seen in this figure ESB precursors are not densely nor uniformly deposited. Typically, PLD is used to deposit

ultrathin, high quality, oriented films on a semiconductor substrate. In this study PLD parameters are set for an unusually fast deposition rate so that the layer can grow micro-level thickness. This fast deposition rate resulted in a porous and lumpy layer. The poor quality of ESB was not improved after heat treatment resulting in porous and rough ESB (Figure 6-7). The SEM images shows that the electrolyte surface is fully covered by ESB, and in fact no pin holes showing the underlying GDC electrolyte were observed. However, the layer is not sufficiently dense enough to block electronic current from GDC from cross-sectional view (Figure 6-8). It is easier to grow a thick and dense ceramic membrane with unusually fast deposition rate by heating the substrate during PLD, and this will be addressed in the following section. However, the poor quality of ESB was still tested because, while the ESB layer may not increase the OCP, it may to decrease the ASR as discussed above.

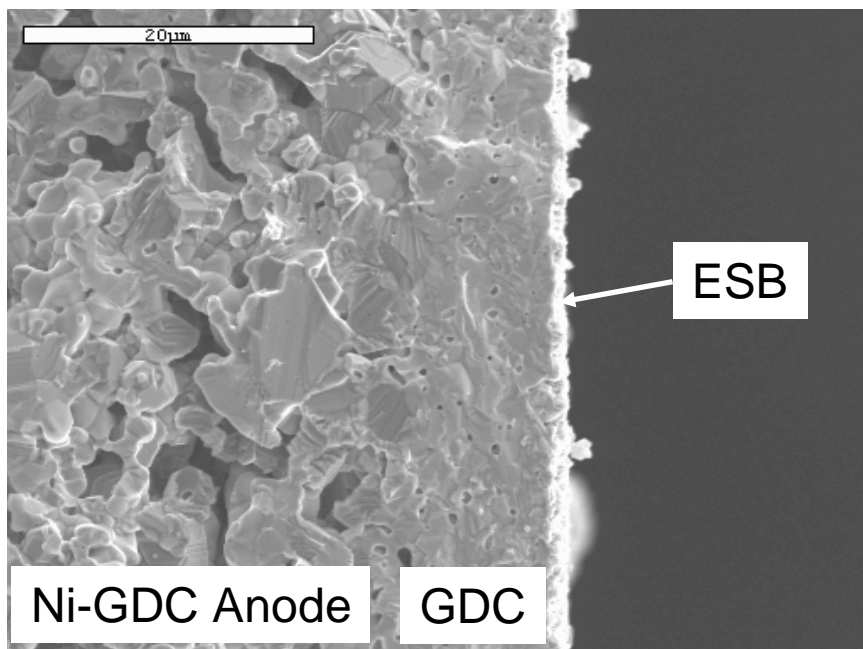


Figure 6-8. Cross-section image of the cell with the ESB layer by cold PLD after heat treatment at 700 °C, 4h.

Figure 6-9 shows XRD data of ESB/GDC bilayer samples prepared by cold PLD. As-deposited ESB on GDC produced GDC peaks and no additional peaks. Instead, it shows a broad

amorphous background probably from the ESB precursor. Thus a calcinations step was performed on these samples in order to yield the fluorite phase for the ESB layer. ESB fluorite peaks appear after heat treatment at 890°C for 4h which is typical sintering temperature and time for solid state ESB fabrication. The cubic fluorite ESB formation was confirmed even at lower temperature, 700 °C for 4h, by PLD deposition.

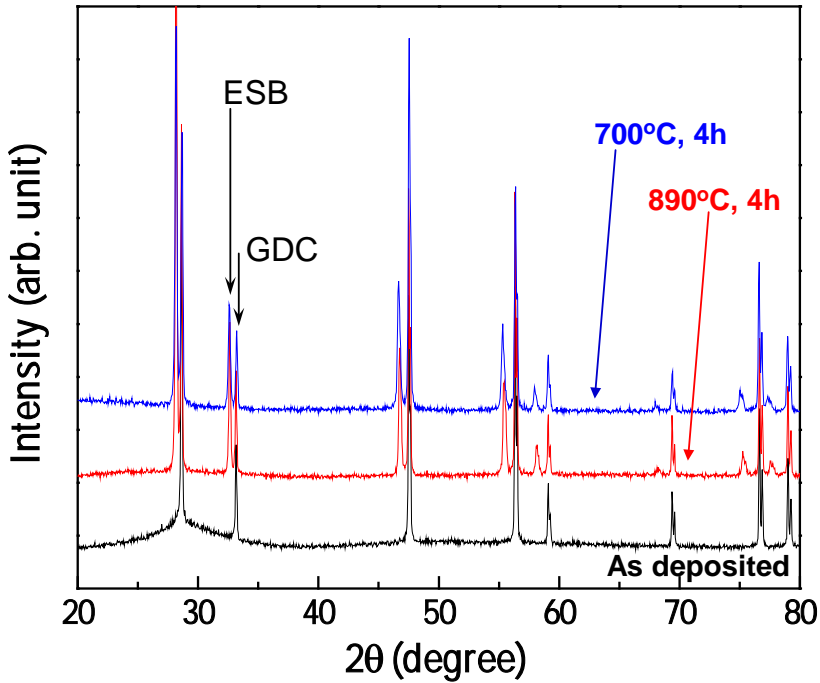


Figure 6-9. XRD patterns of bilayer samples depending on heat treatment conditions. The bilayer sample with as-deposited ESB shows only GDC peaks.

As mentioned in the previous section, spray coating of GDC onto tapecast anode produced low OCP (Figure 6-5). Improvement in GDC single layer fabrication was made by a simple step involving the application of an AFL to the pre-sintered anode substrate surface. Details on the application and mechanism of improvement in performance by the addition of this AFL have been discussed previously in the chapter 4. Figure 6-10 shows that the OCP has been increased slightly to 0.72 V and that the maximum power density has reached 1.03 W/cm² at 650 °C using the AFL.

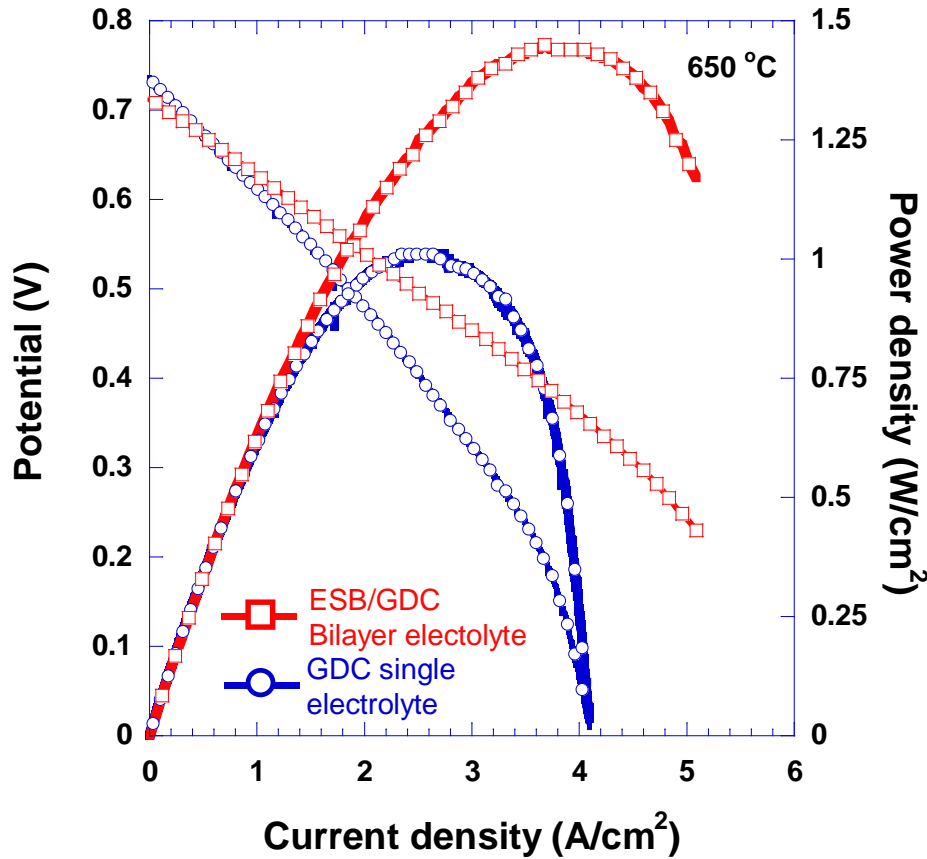


Figure 6-10. I-V characteristics of the samples with GDC single layer and ESB/GDC bilayer electrolyte at 650 °C using 90 sccm of air and wet hydrogen.

Figure 6-10 shows the improvement in performance achieved for the bilayer cell over the single layer GDC cell. As expected from the microstructure and minimal thickness of the ESB layer, the OCP was not improved by the bilayer. However, the maximum power density was improved to 1.45 W/cm². We can derive the total cell ASR, ASR_{IV}, by taking a slope of the I-V curves near the open circuit region. These values are tabulated in Table 6-3. The table shows that ASR_{IV} was reduced from 0.125 to 0.084 Ωcm² when using a bilayer electrolyte. The bilayer cell exhibited a 44 % increase in the maximum power density and a 33 % reduction in the ASR.

Table 6-3. Details of tapecast cell with AFL. ASR unit is Ωcm².

Cell Type	Total ASR _{IV}	Total ASR _{Impedance}	Electrode ASR	Ohmic ASR
GDC Single layer	0.125	0.126	0.064	0.062
ESB(Cold PLD)/GDC	0.084	0.084	0.044	0.040
ESB(Hot PLD)/GDC	0.075	0.079	0.033	0.046

The effect of the bilayer electrolyte on ASR was further investigated with impedance spectroscopy (Figure 6-11). The total ASR obtained from impedance spectroscopy was labeled as $ASR_{Impedance}$ and detailed values of various ASR are also listed in Table 6-3. First, we emphasize that the ASR_{IV} produced by a Solartron 1287 and the $ASR_{Impedance}$ by Par-stat are in good agreement within 1% showing high credibility of the data. The result shows that the bilayer reduced the total ASR of the cell from 0.126 to 0.084 Ωcm^2 . The bilayer reduced both ohmic and electrode ASR 35 % and 31 %, respectively.

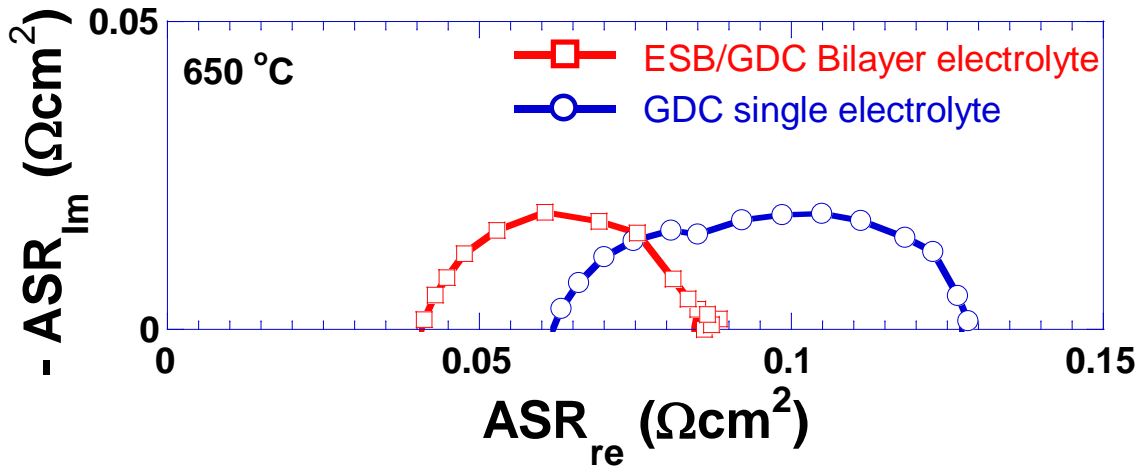


Figure 6-11. Impedance spectra of the samples with GDC single layer and ESB/GDC bilayer electrolyte at 650 °C using 90 sccm of air and wet hydrogen.

It should be noted here that the ohmic ASR is lower in a bilayer sample than in the single layer sample. Equation (6-1) predicts that the lower ohmic ASR using higher ESB thickness for a given total bilayer thickness. However, in this study, the total thickness is not fixed. Rather, the ESB layer is added to the 10 μm GDC layer and should be regarded as an added ohmic resistance. This was the case for every bilayer sample measured. One possibility is that ESB penetrates into the GDC grain boundaries, resulting in lower grain boundary resistances.⁴³ However, further study is needed to resolve this matter.

6.4. Hot PLD

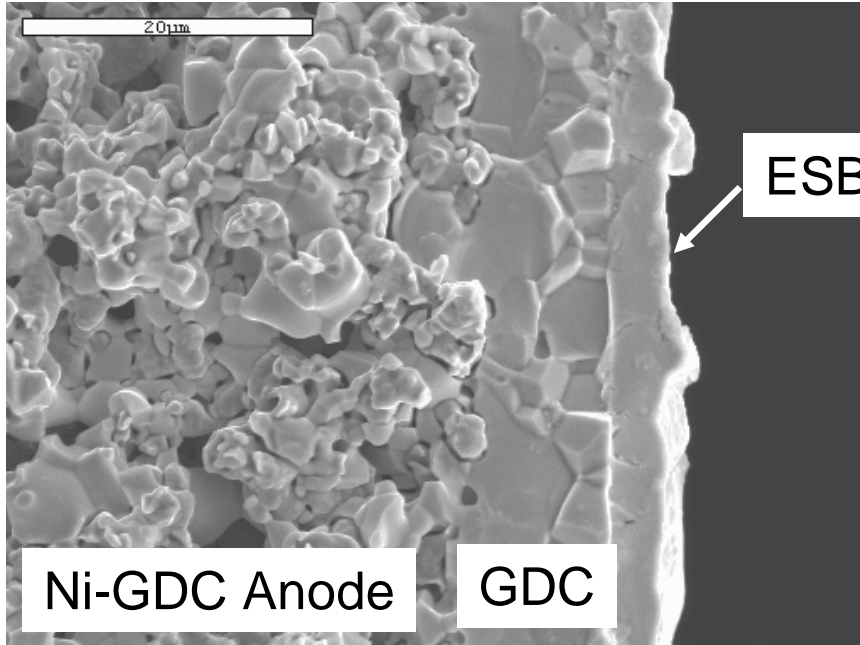


Figure 6-12. The bilayer microstructure with the ESB by Hot PLD.

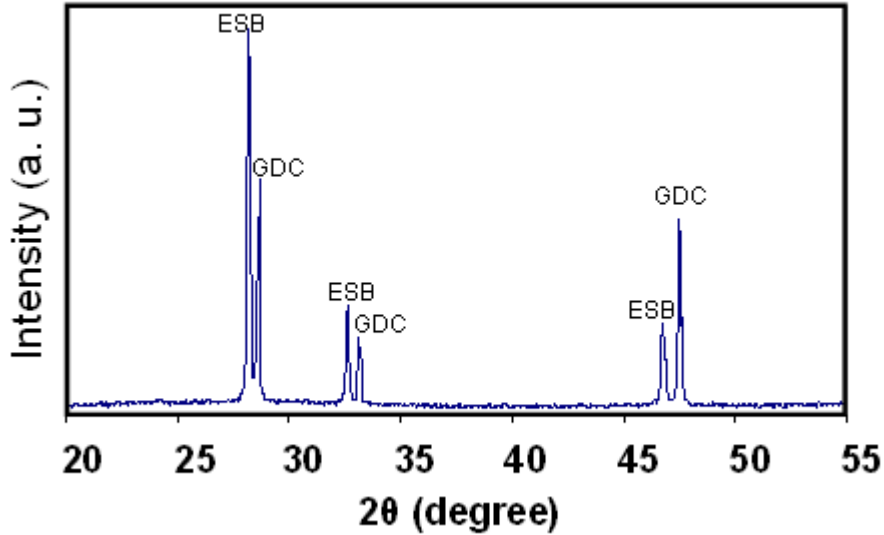


Figure 6-13. XRD pattern of the bilayer sample.

A poor quality ESB film was formed from cold PLD as a result of the very fast PLD deposition rate, which is crucial for attaining micron-thick films. Figure 6-12 shows that the quality of the ESB film was substantially improved by heating the substrate (GDC electrolyte on

the anode) to 630 °C during PLD. It is due to an increase in the sticking coefficient of ablated molecules during PLD. The ESB membrane thickness was ~ 4 μm achieving a 0.4 thickness ratio of ESB to GDC (GDC electrolyte is ~ 10 μm in Figure 6-12). An additional advantage of hot PLD is that an ESB calcination step is not necessary. Figure 6-13 shows that cubic fluorite ESB has formed on the GDC layer without additional heat treatment step.

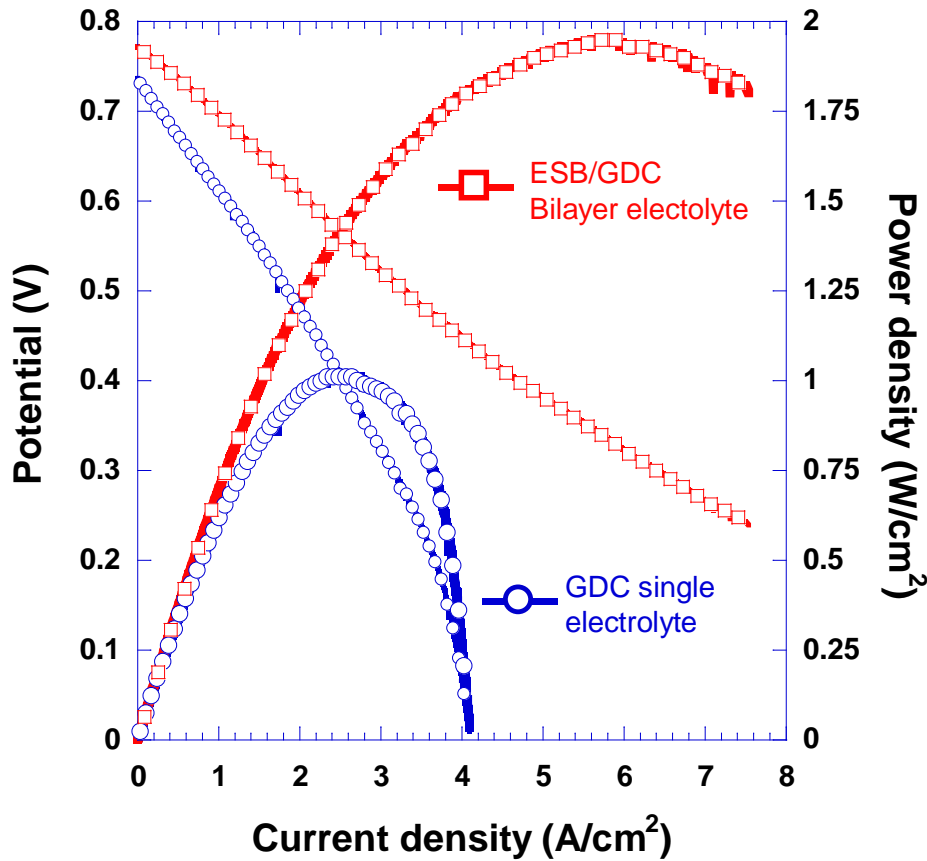


Figure 6-14. I-V characteristics of the samples with GDC single layer and ESB/GDC bilayer electrolyte at 650 °C using 90 sccm of air and wet hydrogen.

Figure 6-14 shows the I-V characteristics of both GDC single layer and ESB/GDC bilayer samples at 650 °C. The bilayer electrolyte and BRO7-ESB cathode increased the maximum power density from 1.03 to 1.95 W/cm² (93 % increase). The slope of I-V curves shows that the bilayer electrolyte achieved an ASR of 0.075 Ωcm²; a 40 % reduction compared with the single layer sample. The increase in OCP from 0.72 to 0.77 V also contributed to the dramatic

improvement in power density. The OCP of the hot PLD sample, 0.77 V, is higher than that of cold PLD sample, 0.71 V. This indicates that the increase in OCP is a function of layer densities and thickness and that hot PLD resulted in denser ESB layer.

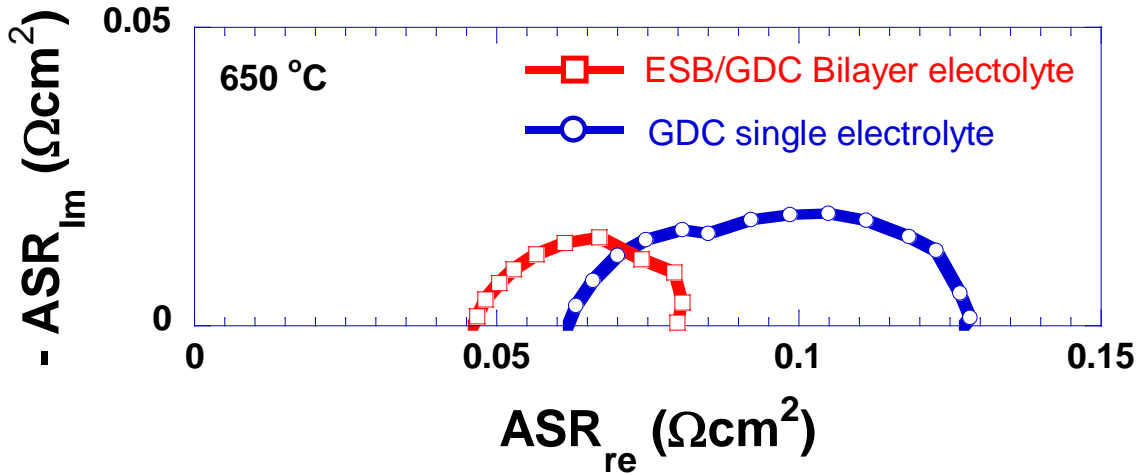


Figure 6-15. Impedance spectra of the samples with GDC single layer and ESB/GDC bilayer electrolyte at 650 °C using 90 sccm of air and wet hydrogen.

Figure 6-15 shows the effect of a bilayer electrolyte on ASR measured by impedance spectroscopy, and the values are given in Table 6-3. Again, the total $ASR_{Impedance}$ matches well with the ASR_{IV} within 5%. Table 6-3 shows the reduction in total $ASR_{Impedance}$ is due to a 48% reduction in the electrode ASR and a 26 % reduction in the ohmic ASR. As was the case for the cold PLD sample, the hot PLD sample also produced lower ohmic ASR than the single layer. The thickness of the GDC layer was $\sim 10 \mu\text{m}$ for both cold and hot PLD sample. However, the reduction in ohmic ASR is more significant in the sample prepared from cold PLD compared with hot PLD. This is most likely due to the fact that the ESB layer was much thicker in the hot PLD (Figure 6) resulting in a proportionally larger electrolyte resistance. Due to the rough nature of the ESB layer produced by cold PLD, the thickness was difficult to characterize. It is safe to assume that cold PLD only provide very thin and porous ESB interlayer. However, thicker ESB

should still be ideal for high power density since it significantly reduced the electrode ASR and increased the cell OCP. The OCP and the ohmic ASR depend strongly on the ESB quality.

Table 6-4. Summary of GDC single layer vs. ESB/GDC bilayer results.

Cell Description	Anode Support Fabrication	GDC Fabrication	ESB Fabrication	GDC Single Layer*	ESB/GDC bilayer*
Co-press	Co-pressed	Co-pressed	Screen print	0.338	0.588
Colloidal	Tape cast	Spray coat	Drop coat	0.407	0.614
Cold PLD	Tape cast with AFL	Spray coat	Cold PLD	1.03	1.45
Hot PLD	Tape cast with AFL	Spray coat	Hot PLD	1.03	1.95

*Maximum power density at 650 °C (W/cm²).

At this point, even with the high performance result, it is hard to demonstrate the full potential of the electrochemical performance of the bilayer electrolyte, mainly due to low OCP of the thin ESB layers. It is obvious that a thin and dense electrolyte is the key to higher OCP and lower ASR, and with it the bilayer electrolyte is expected to present even higher performance. Table 6-4 summarizes the fabrication technique used for the GDC and ESB layers and the maximum power density obtained for each sample.

CHAPTER 7 CONCLUSIONS

First a simple and effective fabrication method to produce an AFL on an anode surface prepared by tape casting was proposed and tested. Without addition of pore formers to the anode we were able to produce reasonably high power density. The high anodic polarization generated by using large NiO as anode catalyst was successfully reduced using an AFL fabricated by the proposed method. The AFL can be deposited by various colloidal techniques. In this study spray-coating was employed to deposit the AFL since spray-coating was also used to deposit the electrolyte, which means continuous procedure from the electrolyte coating to the AFL coating.

Two-point impedance measurements revealed that the AFL affects the electrode ASR and the ohmic ASR. The fully sprayed AFL reduced the total ASR from 0.218 to 0.087 Ωcm^2 and the electrode ASR from 0.114 to 0.036 Ωcm^2 . The maximum power density is increased from 407 to 994 mW/cm^2 at 650 °C by use of the Full-AFL.

The dramatic increase in the maximum power density is not only due to the lower ASR but due to the higher OCP by the AFL. In this study, the low OCP across the GDC electrolyte was improved by 0.12 V. The fact that the ohmic resistance was reduced by 51 % also supports this conclusion. It should be noted here that increases in cell OCP is not the typical purpose of the AFL. Rather, this can occur when the GDC electrolyte coating is not optimized. In this case, a simple AFL step can help increase the low OCP by helping improve the quality of the GDC coating.

Two different single layer AFLs were studied: a GDC AFL and a Ni-GDC composite AFL. The result shows that GDC AFLs have larger electrode ASR values but have higher OCPs. We assume that the smooth and homogeneous surface that the GDC AFL provides is ideal for colloidal deposition of GDC electrolyte. A Ni-GDC AFL is ideal in terms of decreasing

electrode ASR but not for increasing OCP. A multilayer approach was proposed to combine the advantages of these two single layer AFLs. The so-called AFML successfully achieved the relatively high OCP of the GDC AFL and the low electrode ASR of the Ni-GDC AFL resulting in the highest observed maximum power density of 1.10 W/cm² at 650 °C.

The next work was to test the performance of SOFCs based on a novel co-doped ceria electrolyte material under real operating conditions. The anode – supported SOFC was fabricated, with Sm_{0.075}Nd_{0.075}Ce_{0.85}O_{2-δ} electrolyte deposited on NiO-GDC composite anode using colloidal processing. Previously developed AFL was applied in fabrication of SNDC based SOFCs at the interface of SNDC electrolyte and NiO-GDC anode. The microstructure results show a dense ceramic electrolyte of thickness ~ 10 μm deposited on the porous anode. The anode microstructure consists of fine GDC grains with coarse Ni particles.

The current-voltage characteristics were measured at various temperatures, using 90 sccm of dry air and wet hydrogen in cathode and anode sides, respectively. At 650 °C, a maximum power density of 1.43 W/cm² was achieved. The total ASR of the cell was 0.105 Ωcm² at 650 °C resulting in the exceptionally high power density. The impedance analysis revealed that the decrease in power density at lower temperatures is mainly due to the electrode overpotential. The ohmic ASR remains relatively low at most temperatures contributing only ~ 30 % to the total ASR.

The last study examined the incremental improvement in SOFC performance comprised of components prepared from a wide range of techniques—from pressed anodes to tape-cast anodes, from GDC single-layer electrolytes to ESB/GDC bilayer, and from LSCF-GDC composite cathodes to optimized BRO7-ESB composites. GDC single-layer electrolyte based SOFCs were prepared from four different fabrications and exhibit maximum power densities

ranging from 0.338 to 1.03 W/cm², at 650 °C. At each fabrication stage, an ESB layer was applied to form a bilayer electrolyte. ESB was deposited by a range of techniques including colloidal deposition and PLD. The result confirms that depending on a fabrication route the bilayer electrolyte can reduce the total ASR 33~49 % and increase the maximum power density 44~93 %.

A bilayer ESB (hot PLD)/GDC electrolyte produced an exceptionally high power density of 1.95 W/cm² at 650 °C. The results herein show that utilization of a bilayer ESB/GDC electrolyte can reduce total cell ASR by 49 % and increase the maximum power density by 93%, giving credence to its use in practical SOFC applications, particularly at reduced operating temperatures. Further improvement in colloidal deposition of thin, dense ESB layers is expected to increase OCP and yield even higher power densities.

APPENDIX A STACK CELL APPLICATIONS

SOFCs have gained attention for many years as clean energy conversion devices. Due to high operating temperature and high efficiency, the most suitable SOFC application is believed to be stationary applications. To be able to generate reasonably high voltage and power for practical applications, stacks of a large number of highly efficient individual cells are required. Figure A-1 shows research activities toward fabrication of SOFC stacks applicable to the industry. Though these are the most advanced SOFCs, there are many obstacles still preventing successful commercialization of SOFCs, such as long term stability, low fabrication cost, and high efficiency, etc.

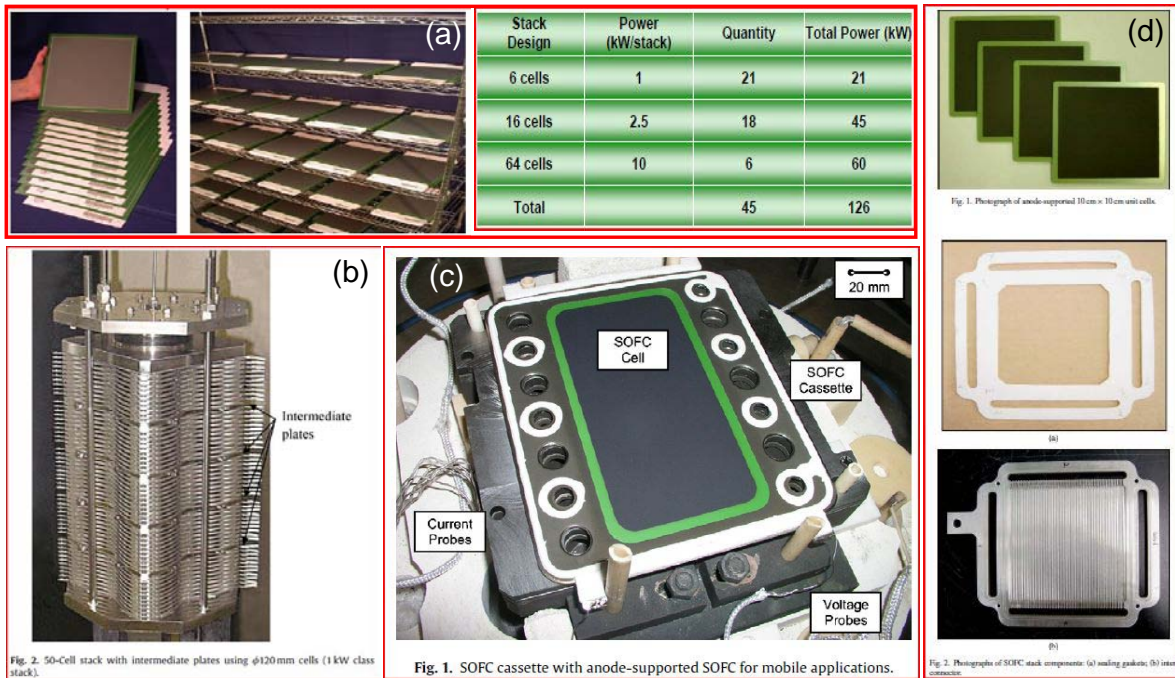


Figure A-1. SOFC Stack cell development in many countries. (a) Fuel Cell Energy, Inc.⁷⁴ in the U.S. (b) NTT Energy⁷⁵ in Japan. (c) German Aerospace Center, DLR⁷⁶ in Germany. (d) KIST⁷⁷ in South Korea.

Recently, the Florida Institute of Sustainable Energy (FISE) was built at the University of Florida to research SOFCs that can operate at lower temperatures with various fuels, such as

hydrogen, biofuels, ethanol, diesel and so on. Recently FISE was successful in development of a novel AFL, application of a new co-doped ceria, high performance using ESB/GDC bilayer electrolyte, ESB compatible low ASR cathodes, use of JP8 and other hydrocarbon fuels and so on. After a progressive series of successes, a maximum power density of $2\text{W}/\text{cm}^2$ at the IT range was achieved. Since these results were based on tapecast anode supports, scale-up to larger size should be relatively easy.

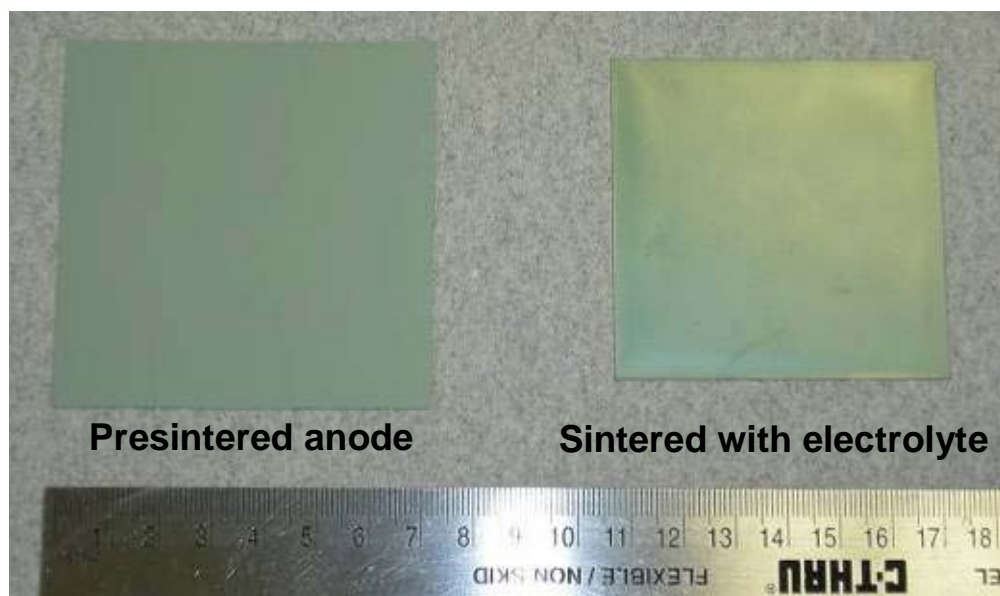


Figure A-2. Planar SOFC sample with 6 cm x 6 cm in size with possible active area of 30 cm^2 . The sample consists of NiO-GDC anode, GDC electrolyte by spin coating, and GDC AFL.

Figure A-2 shows 6 x 6cm planar cell with possible active area of 30 cm^2 (5.5 cm x 5.5 cm). These cells used the same NiO-GDC anode tapes as the previously tested button cells. Instead of punching out circular supports, a square 7.5 cm x 7.5 cm anode tape was cut out assuming 15% lateral shrinkage. After presintering, previously developed GDC AFL was applied using precursor solution and GDC electrolyte was applied by spin coating method (Chemat technology Inc.). Detailed process on tapecasting and AFL deposition can be found in the chapter 3 of this dissertation.

Figure A-3 shows the microstructure of the planar SOFC sample. From the surface and cross-sectional view a few pores were observed, but they were mostly isolated. Figure A-3 (c) shows the back-scatter image of an anode cross-section by tapecasting. As expected large NiO particles were observed, and they were surrounded with well dispersed micro-sized GDC particles. Judging from the microstructural images, we can conclude that scale-up to 30 cm² was successfully achieved. However, the most convincing test for a SOFC is I-V measurement.

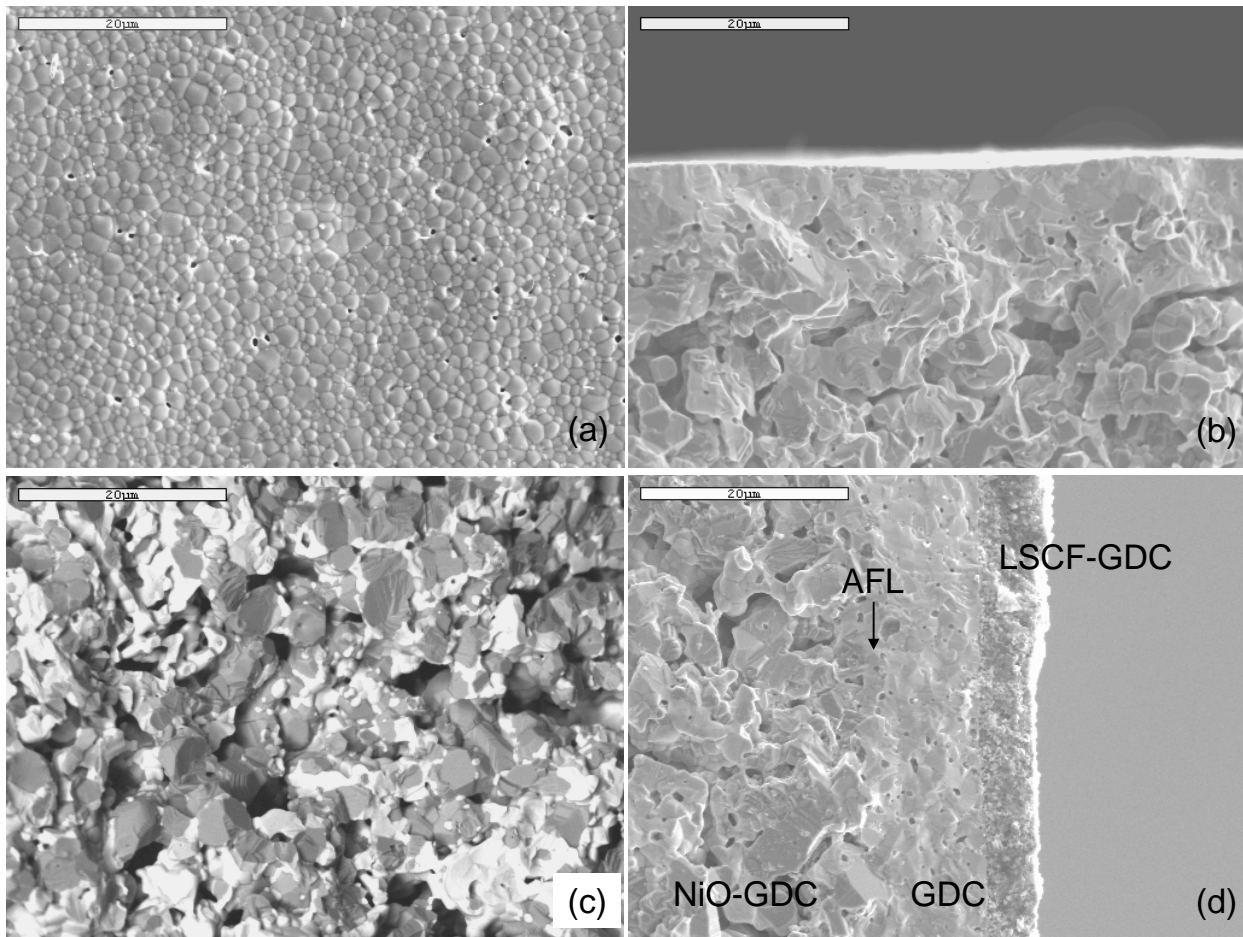


Figure A-3. Microstructure of planar SOFC sample (a) surface view. (b) cross-section of GDC on NiO-GDC anode. (c) backscattered image of anode cross-section. (d) cross-section of the planar cell with brush painted LSCF-GDC composite cathode before test.

Even though FISE has the capability of measuring large sized SOFC samples, the setup is not done yet. In the mean time, a circular button was taken out from the planar sample. The

button cell was mechanically polished to 1 inch in diameter, and LSCF-GDC composite cathode was applied as described in chapter 3. Figure A-3 shows the cross-sectional view of the sample. Note that brush painting is not a reproducible technique and is therefore not applicable for larger cells. It was only applied to the button cell for this experiment. A better deposition technique using screen printing is currently being developed for future cells.

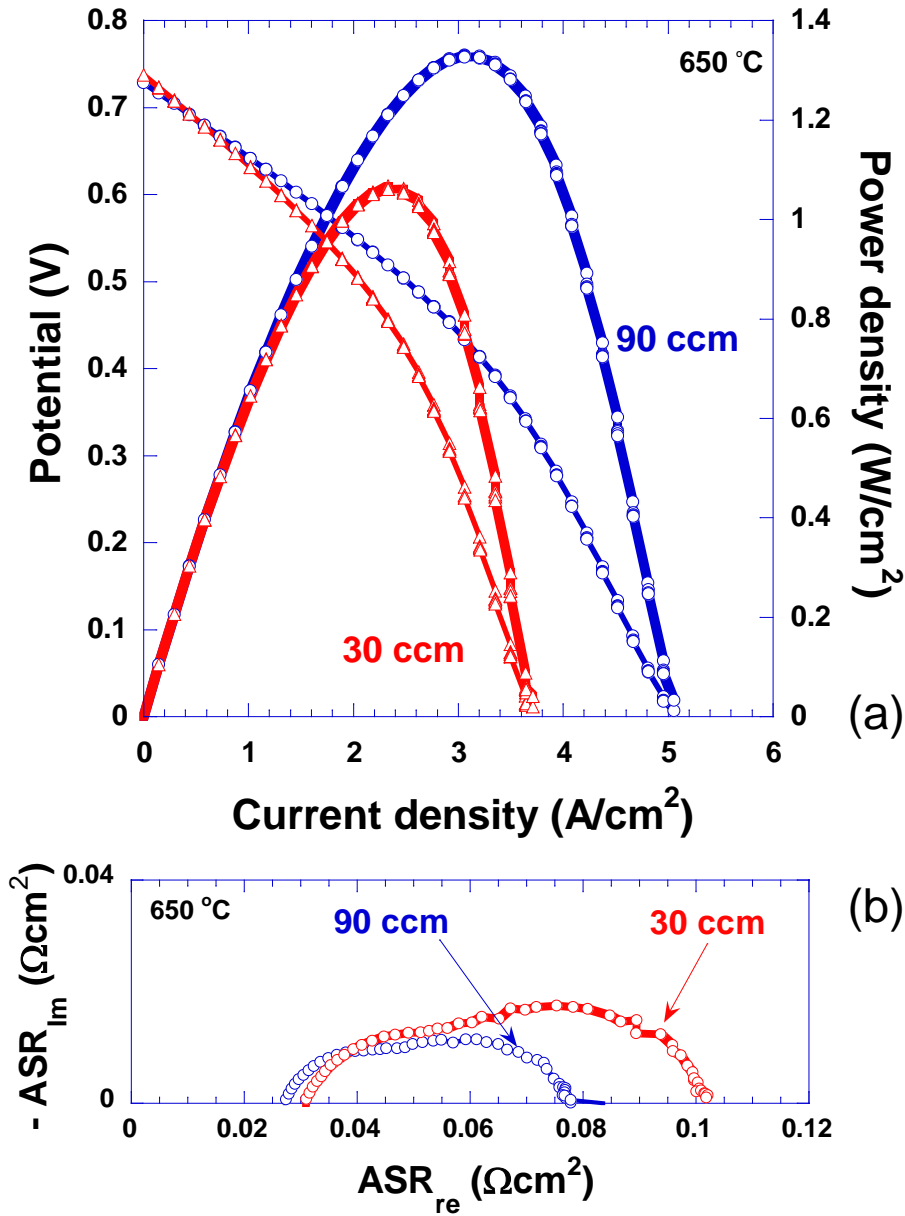


Figure A-4. I-V characteristics (a) and impedance spectra (b) of a button cell taken from a large stack cell. 30 and 90 sccm symmetric flow-rates were used for hydrogen and air.

Figure A-4 shows the I-V characteristics and impedance data of the SOFC sample at 650 °C. Since the planar cells will eventually be used in a stack, which has different testing environment in terms of fuel and oxidant flow, both 30 and 90 sccm flow-rates were tested. The OCP showed a typical partial GDC AFL value (chapter 4). The maximum power densities were 1.07 and 1.33 W/cm² for 30 and 90 sccm, respectively. Simple comparison with the result for the partial AFL reported in chapter 4, shows that the performance of the SOFC was enhanced. Figure A-4 also shows impedance spectra for 30 and 90 sccm. It indicated that the reduction in the ASR due to higher gas flow-rate is mainly due to reduction in gas conversion limitations. However, further study is required to analyze impedance data to determine the processes ascribed to each semicircle.

The button-cell test confirmed that the fabrication of the planar cell for a stack application resulted in a high quality SOFC samples, satisfying high efficiency requirements for actual applications. In order to test the planar cells under real stack operating conditions, a better technique for uniform cathode deposition over a large area should be developed. The initial choice was the spray coating, which was well studied for the electrolyte deposition previously. Figure A-5 shows a stack cell that has spray-coat LSCF-GDC cathode.

Recently we found that the spray-coating of LSCF-GDC cathode is a good cathode deposition method without any delamination or cracking found. However, to prevent accumulation of slurry at the center of the cell, a large spray diameter is required. To deposit a thick and laterally continuous cathode with that large target area, too much slurry was wasted. More recent results on screen printed cathodes demonstrated a thick cathode can be achieved with good uniformity. Currently, the application of screen printed cathodes using an automated screen printer at FISE is being investigated.

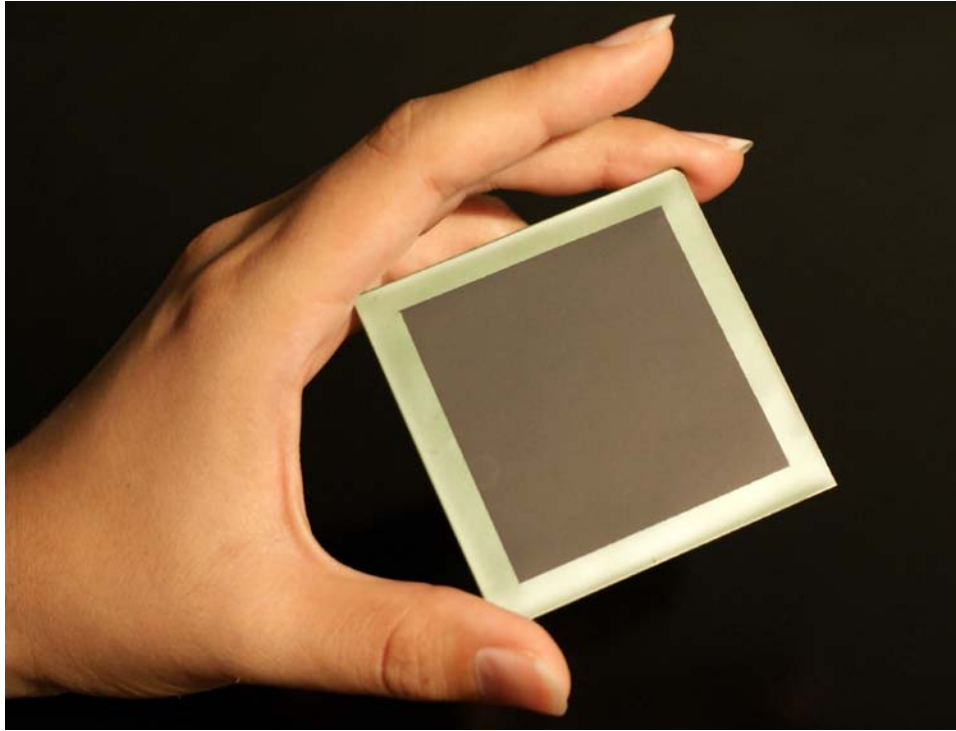


Figure A-5. 6 cm x 6cm SOFC planar cell with NiO-GDC anode, GDC electrolyte, GDC AFL, and 30 cm² LSCF-GDC cathode.

At the University of Florida, alternative electrolytes have been developed with higher ionic conductivities, such as Dy and W doped bismuth oxide²⁸ and Sm and Nd doped ceria. The application of these new materials into an actual fuel cells and stacks with bilayer electrolyte configuration shown in chapter 6, with novel molecular AFLs and optimized Bi₂Ru₂O₇ composite cathode, will likely demonstrate an exceptionally high performance. I believe that this dissertation made a significant contribution to realization of highly efficient SOFC fabrications.

APPENDIX B REPRODUCIBILITY AND STABILITY

The SOFC performance results in this dissertation were exceptional. However, the length of time in processing and testing trials required to achieve these good results was not discussed. Also, it would be difficult for an inexperienced SOFC researcher to reproduce the same level of power density. Similarly, this dissertation did not cover stability issues, which is a crucial factor for real-world applications. This chapter is designed to describe the multitude of failures that have occurred over the past 2 years, and how there are still problems that need to be solved.

1. Slow Progress toward High Performance

It should be noted here that the previous chapters of this dissertation deal with results that were relatively reproducible and reliable. This section deals with the results that were gathered when reproducible and stable operation was not achieved. So, most results presented in this section should not be referenced for any scientific matters.

The anode of the first cell was prepared by uniaxial pressing of a mixture of NiO (J.T.Baker) and GDC (Rhodia) powder. GDC electrolyte slurry was prepared without plasticizer, and the dispersant and binder quantity was not optimized. The composition is given in the following subsection. The GDC electrolyte was dip coated onto the anode and LSCF-GDC cathode was brush painted on the electrolyte. The first test resulted in 7 mW/cm^2 at $650 \text{ }^\circ\text{C}$ with an OCP of 0.55 V . The main problem of having extremely low power density is that it is difficult to determine the main polarization mechanisms. Also, unstable OCP allows only a limited number of tests at a limited temperature range. At that time, impedance measurements were not employed for the performance testing, which would separate ohmic and non-ohmic resistances giving better information regarding the dominant polarization mechanism.

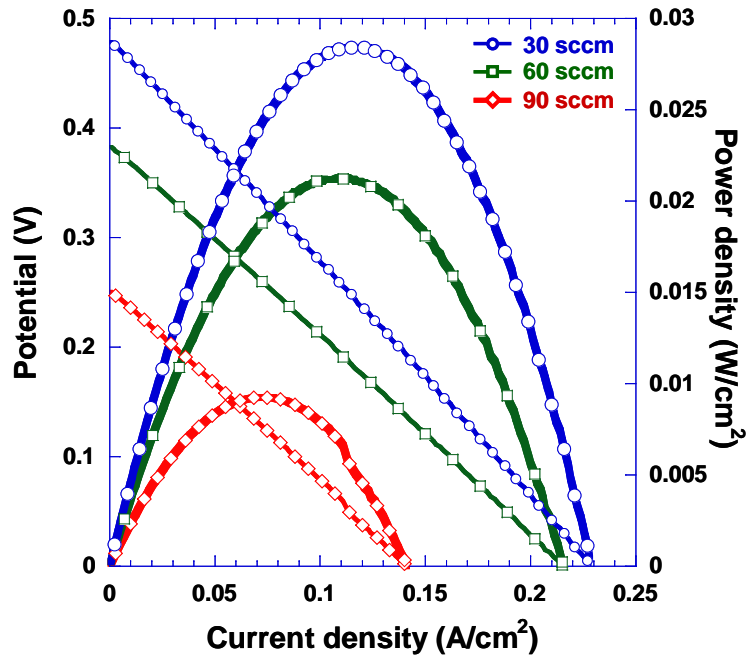


Figure B-1. I-V characteristics of the sample after 6 months of studying. Increasing H_2 from 30 to 90 sccm dramatically decreased the OCP and the power density indicating external gas leak.

Figure B-1 shows that, even after studying similar cells more than 6 months, the results were very poor at 650 °C. In this figure three main problems were observed: low OCP, high resistance and external gas leak. The OCP of 0.5 V was a normal value at that time mainly due to the porous nature of the electrolytes developed. The porosity of the electrolyte was so great that large NiO grains were commonly observed in the electrolyte, which will reduce to Ni metal during operation conducting electrons through the electrolyte (Figure B-4 (b)). Also, while maintaining the air flow-rate at 30 sccm, and increasing H_2 flow-rate from 30 to 90 sccm yielded a significant drop in OCP indicating a large external gas leak. Finally, the ASR estimated from the I-V curve is $\sim 4 \Omega\text{cm}^2$, which is extremely high value at 650 °C.

1.1 Electrolyte Particle Size Effect

The first step toward the pursuit of higher performance involved selecting the right powder from various particle sizes. Three different GDC powders were obtained from different

companies (Nextech, Rhodia and Anan) and the mean particle size was measured by a Beckman Coulter LS13320 particle size analyzer: 304.7 ± 12.3 nm for GDC (Nextech), 278.2 ± 29.1 nm for GDC (Rhodia) and 236.0 ± 8.4 nm for GDC (Anan). Figure B-2 shows the I-V curves of the three samples with three different GDC powders. It is hard to conclude that simply changing particle size from 304.7 to 236.0 nm increases the power density 165 % especially when the reproducibility of the performance was questionable. However, it is obvious that decreasing particle size increased the OCP and increased the maximum power density.

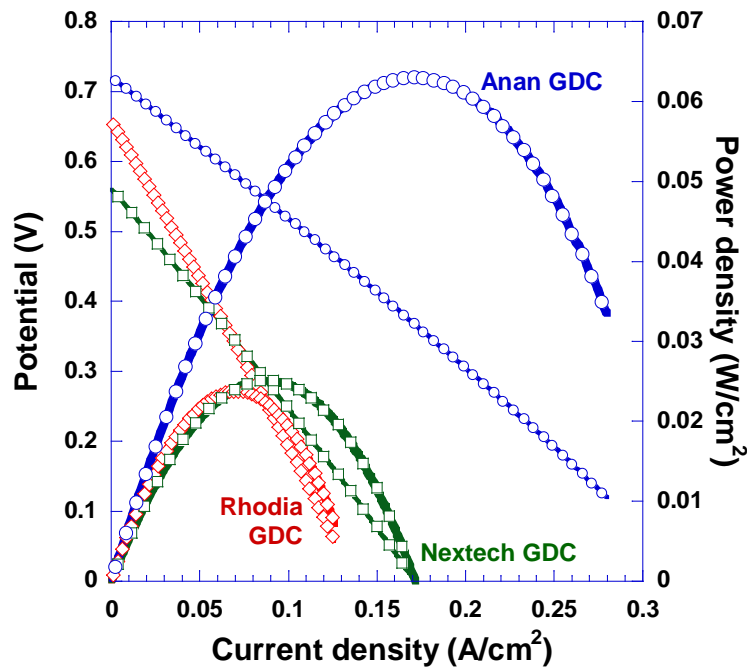


Figure B-2. I-V characteristics of GDC powders from three different companies at 650 °C.

The same trend for particle size effect was observed in the SNDC electrolyte tests. Chapter 5 only presented SNDC powder made from co-precipitation. Changing SNDC synthesis route from solid state to co-precipitation yielded smaller particle size and therefore a major change in the microstructure was achieved, as seen in Figure B-3 (a) and (b). Note that Figure B-3 (b) shows the SNDC deposition on the GDC AFL, which, as described previously, provides a better

surface for colloidal deposition. However, the significant change in microstructure of the electrolyte is evident.

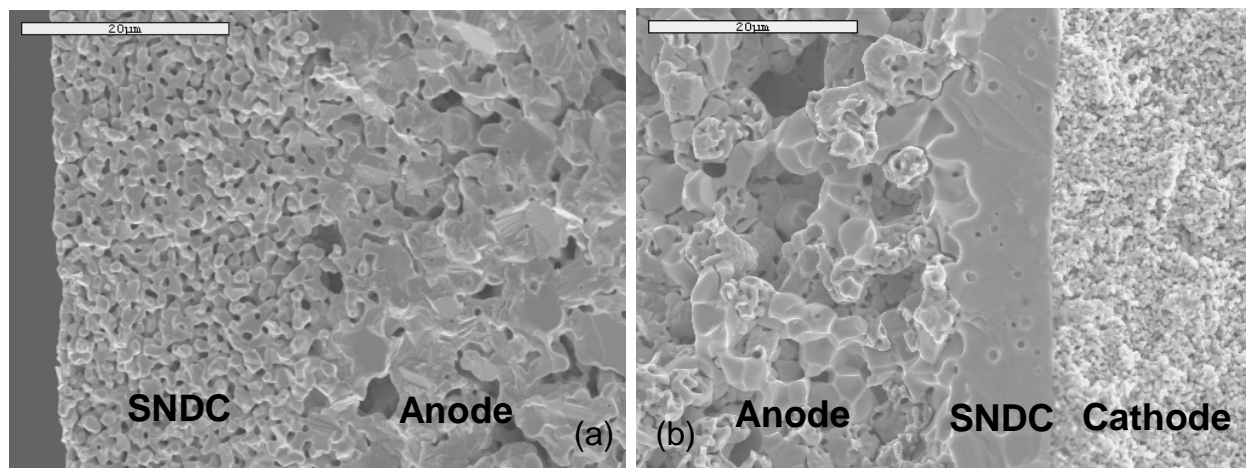


Figure B-3. (a) SNDC synthesis by solid state route. (b) SNDC synthesis by co-precipitation route.

1.2. Slurry Composition

Figure B-4 (a) and (b) shows surface and cross sectional views of the GDC electrolyte on the NiO-GDC anode. Note that the magnifications are different in the figure. As seen in Figure B-4 (b), large NiO grains are found in the GDC electrolyte. This NiO penetration was a frequent problem before better electrolyte quality was achieved. The initial GDC electrolyte slurry composition was as following: GDC (10 g), Corn oil (0.3g) and PVB (1g) and ethanol 50cc. The initial composition was not taken from any literature and judged purely by eye. To achieve the change in microstructure from (a) and (b) to (c) and (d), it took more than 2 years of trial-and-error experimentation. Among many trials, no systematic research was taken to optimize the slurry composition mainly due to instability of the performance and therefore any reasonable conclusion on each component's concentration effect was hard to establish. However, the final composition is given in Chapter 3 of this dissertation with addition of DBP as plasticizer. A thorough study is not presented here, but in general PVB prevents delamination of the film,

dispersant reduces agglomerates in the slurry, and DBP prevents crack formation during the drying process of the green body.

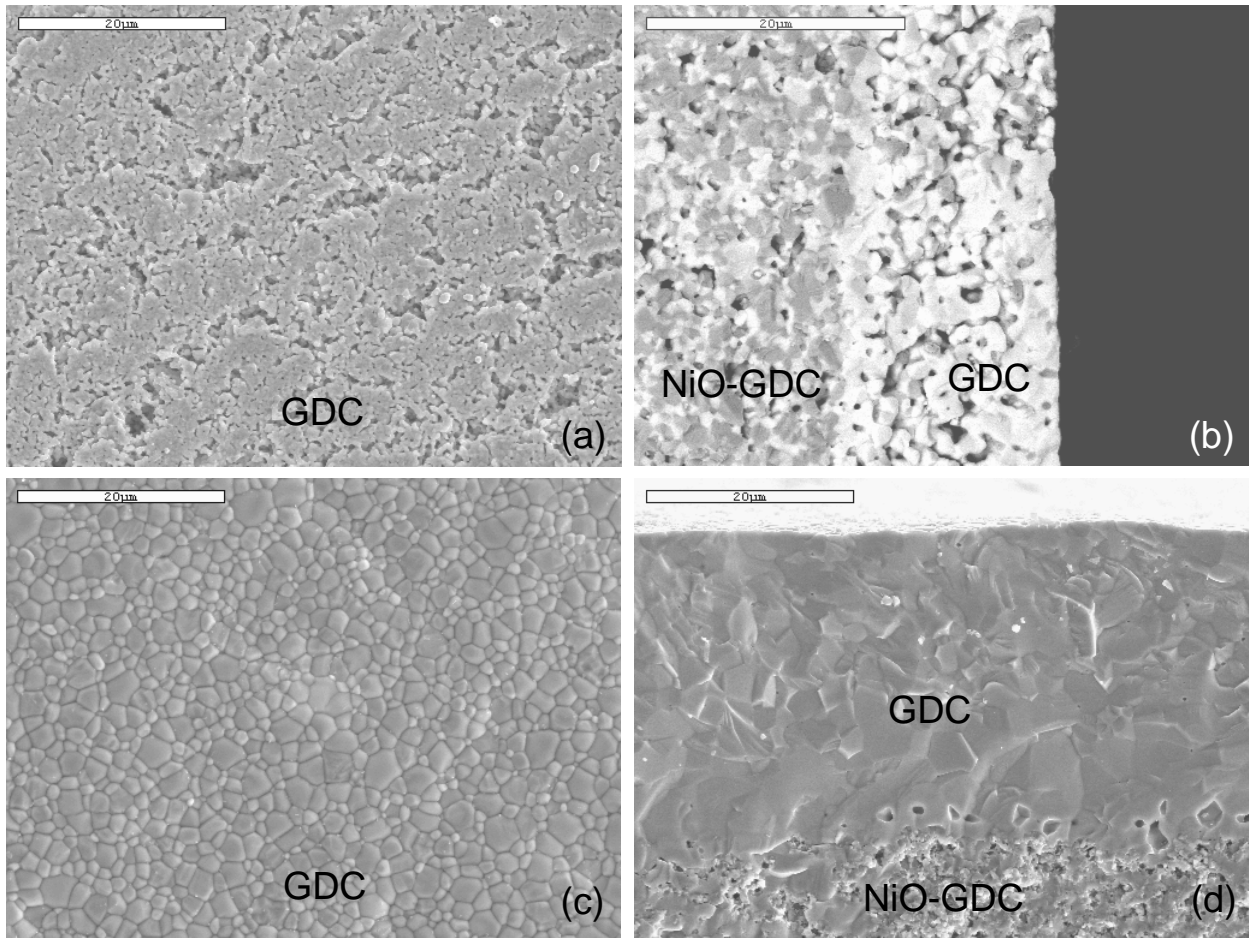


Figure B-4. (a) Surface of the GDC electrolyte. (b) Back-scattered cross-sectional image of the GDC electrolyte on NiO-GDC anode. (c) Surface of the GDC electrolyte with higher density. (d) Cross-sectional image of the GDC electrolyte with higher density.

It should be noted that the use of extensive amounts of these three organic components yields an excellent green body and, sometimes even after sintering, the film looks dense. However, I-V testing still shows either low OCP or high ohmic resistance in this case. The typical microstructure of this type of sample is given in Figure B-5. The sample in the Figure B-5 looked shiny and transparent. In general shininess means fewer defects in the film, light scattering can be used as a qualitative estimation method of electrolyte density. Samples with

extensive amounts of organic compounds emit a greater volume of fumes around 400 °C during sintering, and it is likely that full densification is difficult to achieve since the green body loses such a large fraction of its volume. The total amount of organic compound has been limited less than ~10 wt% throughout the studies in this dissertation. A better electrolyte was achieved by particle size optimization and the slurry composition study, but the poor performance with very low OCP was not solved to this point.

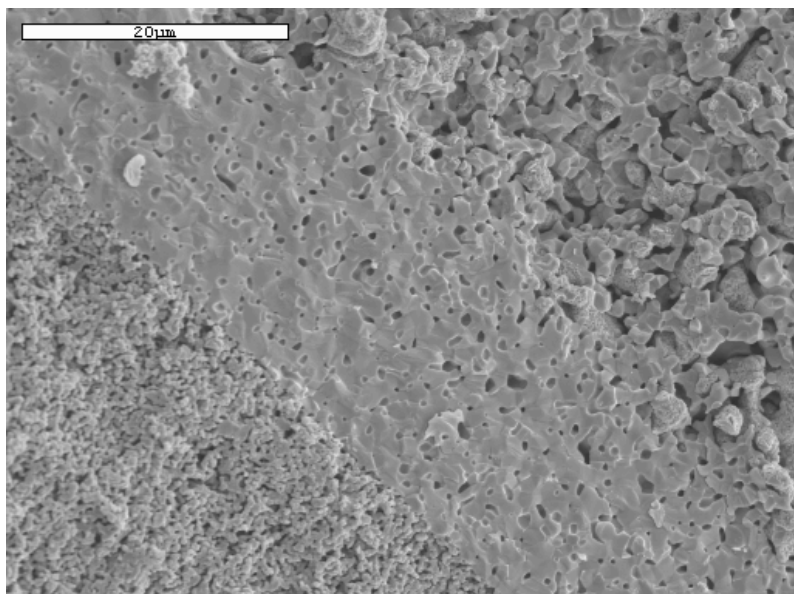


Figure B-5. A sample looking acceptable from visually inspection can have poor performance and porous microstructure.

1.3. Co-pressing

The first significant improvement in terms of performance was made by changing the fabrication route to co-pressing. This involves pressing the anode with a uniaxial press followed by spreading the electrolyte powder on top by opening the cap of the die, and co-pressing the anode-electrolyte bilayer again. Details on co-pressing method are present in Chapter 3. The major disadvantage of this method is that the anode and the electrolyte thicknesses can not be reduced, which is not suitable for achieving high performance. However, Figure B-6 shows the I-V curves of the co-pressed sample. The maximum power density values achieved was much

lower than what would be considered acceptable for publication but the major contribution that the co-pressing route provided was a high and stable OCP. The co-pressed cells still exhibited external gas leak ranging from 2.5 to 5 sccm using 30 sccm of inlet gas. However, high and stable OCP enabled study of the effect of flow-rate on performance.

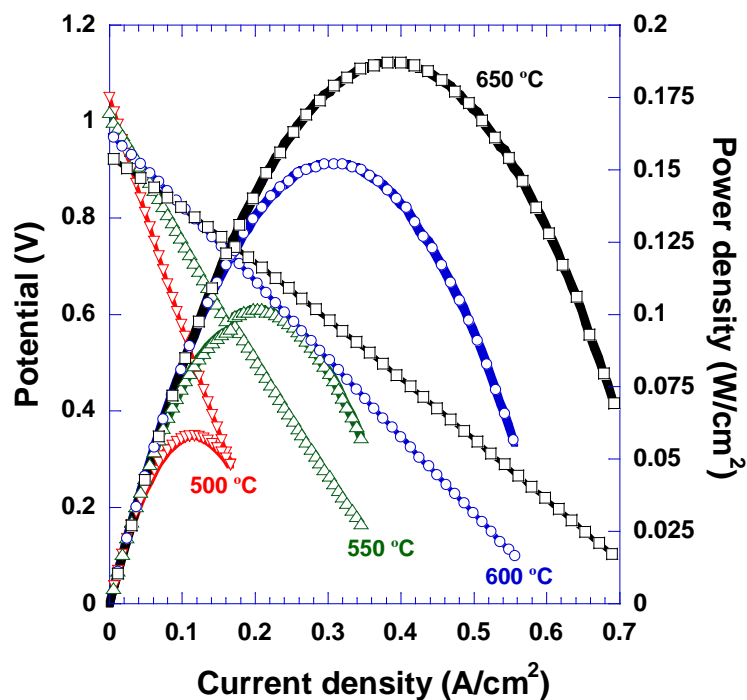


Figure B-6, I-V curves of the co-pressed sample at various temperatures using 90 sccm dry air and wet hydrogen.

Figure B-7 shows the H₂ and air flow-rate on the I-V curves at 650 °C. The result shows that changing in the gas flow-rate on the cathode side does not give a significant change in performance, while changing the flow rate on the anode side yielded a substantial change in performance. From this result it can be concluded that the gas flow through a thick and dense anode pellet is a significant problem. While co-pressing resulted in an in-house record high performance of 187 mW/cm² at 650 °C and further improvement on performance is possible, further study was not performed mainly because of the inherent limitation of the pressing method. At that time we decided to move on to tapecasting the anode support, where thin anodes

and electrolytes are more feasible. The details on the anode tapecasting were covered in Chapter 3 of this dissertation.

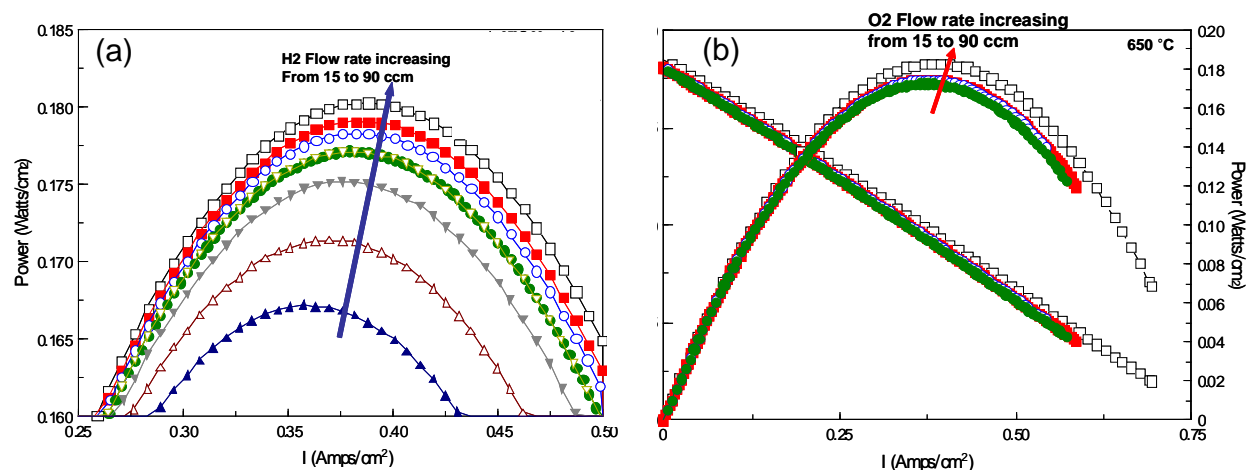


Figure B-7. (a) Change in the power density with increasing H₂ flow-rate from 15 to 90 sccm with 30 sccm of air. (b) Change in the power density with increasing air flow-rate from 15 to 90 sccm with 30 sccm of H₂.

1.4. Spray Coating

Though a high performance SOFC using dip-coating method is possible, it takes for a researcher long time to make a good coating by dip-coating based process. Many times, when equipment for fabrication is limited, experiments at a university lab scale rely heavily on the experience of the researcher. At this point, art is a more dominant factor in the result than science. While experiments relying on devoted human skill can be reproducible, still difference between batches are not avoidable in general. Also, the transfer of knowledge of the same technique is not easy. Frequently, detailed descriptions on an experiment don't promise good reproducibility by other researchers. Therefore, advanced processing requires minimal change in performance between batches and should be independent of the researcher conducting the study. In an effort to have a better and reproducible method, spray coating was introduced. While dip-coating and drop coating requires a human hand to deposit the slurry and to remove the excess

slurry on the surface, spray coating utilize spray time and air pressure to deposit and substrate temperature to remove the excess slurry. Figure B-8 shows a custom-made spray coating setup in a hood, which was used for deposition of GDC electrolytes used in Chapters 4 and 6 of this dissertation.

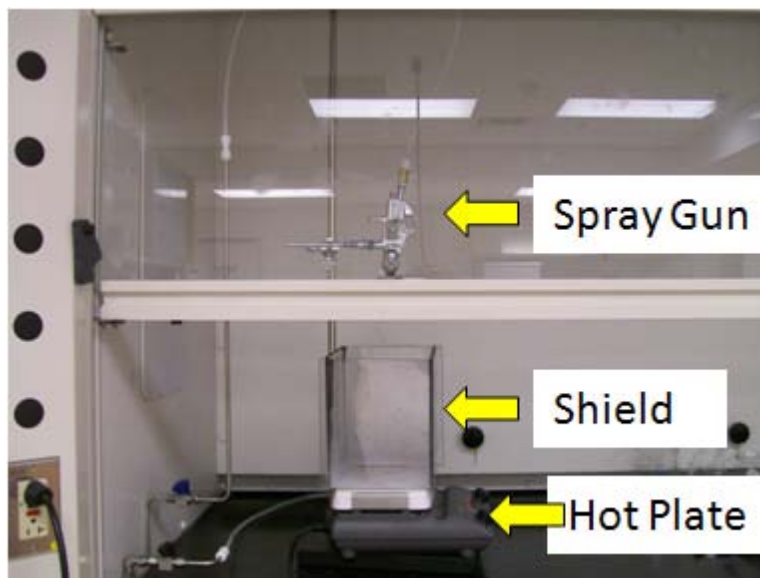


Figure B-8. A custom made spray coating setup.

1.5. Reproducibility

It took more than 2 years and 126 pressed and tested samples before achieving 0.3 W/cm^2 at $650 \text{ }^\circ\text{C}$. Including non-tested samples, roughly more than 200 pressed samples were fabricated. The 127th tested sample is the first tapecast SOFC with dip-coated GDC electrolyte and it resulted in the maximum power density over 0.3 W/cm^2 . However, it took less time to achieve 1 W/cm^2 at the same temperature. So far, 55 tapecast samples were tested and the 26th tapecast sample achieved 1 W/cm^2 . Figure B-9 shows that high performance was reproduced for 3 consecutive samples though they were not fabricated for reproducibility test which requires all experimental parameters kept the same. The repeatable high performance means most experimental parameters were in good control. Also, the fact that less time was required to

achieve the next break-through supports this idea. For example, the maximum power density of 2 W/cm^2 presented in Chapter 6 was achieved by making 1 sample of ESB/GDC bilayer electrolyte. However, the stability of this cell was poor and did not last even 24 hours. Reproducibility comes from good control in experimental parameters and repeatable fabrication methods, but the stability of the SOFC is another subject that requires extensive study.

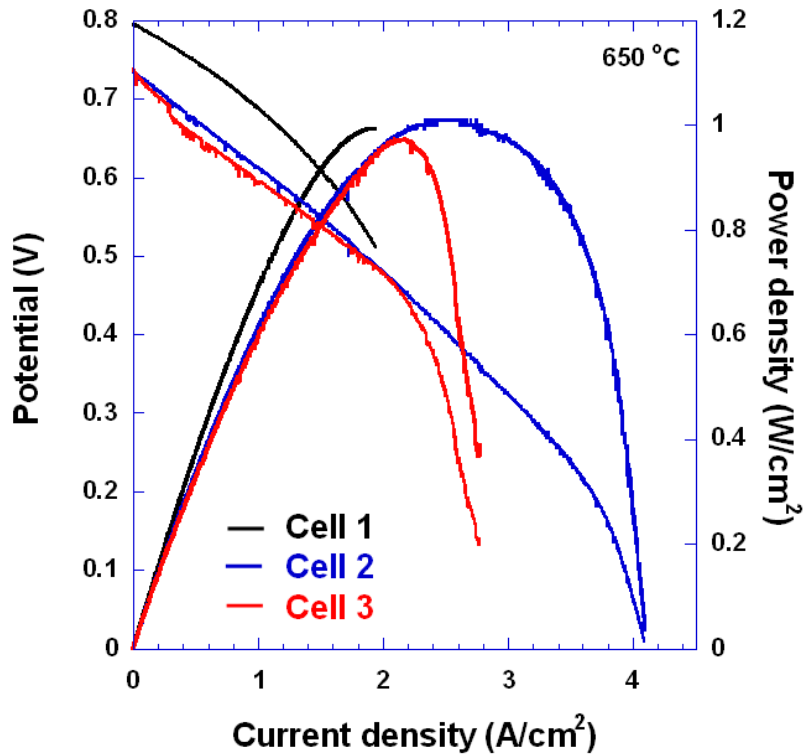


Figure B-9. I-V curves from three consecutive three cells showing reproducibility of high performance at $650 \text{ }^\circ\text{C}$. In each experimental parameters are different, but high performance was reproduced.

2. Future Work

This subsection deals with the important issues that haven't been solved. In order to solve the problems listed here, thorough research over a long time span is required.

2.1. Sealing and Leak

By measuring the gas flow-rate of the inlet and the outlet of the SOFC testing apparatus, one can quantify the gas leak. GDC based cells (GDC electrolyte on NiO-GDC anode) with P571

(Aremco) ceramabond usually exhibit leakage ranging from 2.5 to 5 sccm using 30 sccm of inlet gas. Seal testing with various glass o-rings was previously studied by James Rhodes.⁷⁸ However, no gas tight seal was achieved for GDC based cells from any glass o-rings used in the above study, and the gas leakage was comparable to that observed for ceramabond. In this dissertation ceramabond was used because the maximum curing temperature is 372 °C, whereas glass o-rings require furnace temperatures usually above 800~900 °C for 1~3 hours. 5 sccm of gas leak corresponds to 17% hydrogen gas loss to the cathode side, which is significant and may in fact lower the P_{O_2} of the cathode side.

The CTE for ceramabond P571 is $12.6 \times 10^{-6}/^{\circ}\text{C}$ and the CTE for GDC is $12.7 \times 10^{-6}/^{\circ}\text{C}$. However, since GDC is a thin membrane and only a small volume portion of the sample, the cell CTE will be dominated by the anode, which is cermet of NiO and GDC. Mismatches in CTE between the sealant and the sample can be a problem. However, it should be noted here that the same ceramabond (and even various glass o-rings) was used for YSZ based cells (YSZ electrolyte on NiO/YSZ anode) and in the case of YSZ based cells, no external gas leakage was detected. So, it is obvious that sealing GDC based samples is much more difficult. Also, typically no gas leak is observed at the start of H_2 flow to the anode, but the gas leak gradually increases with time. This indicates that changes in the sample when exposed to reducing conditions may in fact cause the leak.

According to Bishop et al., the chemical expansion of GDC is almost the same order of thermal expansion.⁷⁹ I believe the chemical expansion from the bottom of the anode progressing toward the electrolyte is the main problem. This was confirmed by the fact that GDC based samples do not exhibit leakage when Ar gas, which has P_{O_2} of 10^{-6} (Airgas), is used on the fuel side. To address this problem, Ag-paste (DAD87, Shanghi RISR) used commonly for I/C circuits

and Ag conductor paste (9907, ESL) were applied and compressed by the same ceramic tube from the cathode side, but the preliminary test confirmed the same level of leakage. At this point no solution has been suggested. To solve this problem a compliant sealant is required.

Compressive sealing using metallic o-rings can be a solution, but much study is required since each company has large number of pastes depending on purpose of use.

While gas-tight seal hasn't been available, the application of the ceramabond for reduced leakage was studied. Ceramabond 1 powder P571 and a solvent, L571 were mixed in a 1.5 to 1 wt% ratio and applied to the sample. Then one curing step at 94 °C for 1 hour was applied as per the company instructions. Ceramabond 2 consists of the same P571 and L571 mixture applied to the sample. However, after standing at room temperature for 2 hours, the liquid component was applied onto the ceramabond surface. Then a 3-step cure was conducted at 94, 260 and 374 °C for 2 hour each. The external gas leak was reduced from 5 to 2.5 sccm with Ceramabond 2.

Figure B-10 shows Ceramabond 1 and Ceramabond 2 produced different results in I-V characteristics at all temperatures. However, it should be noted that ceramabond 2 steal has 8.3 % gas leak, and this is a problem that needs to be resolved.

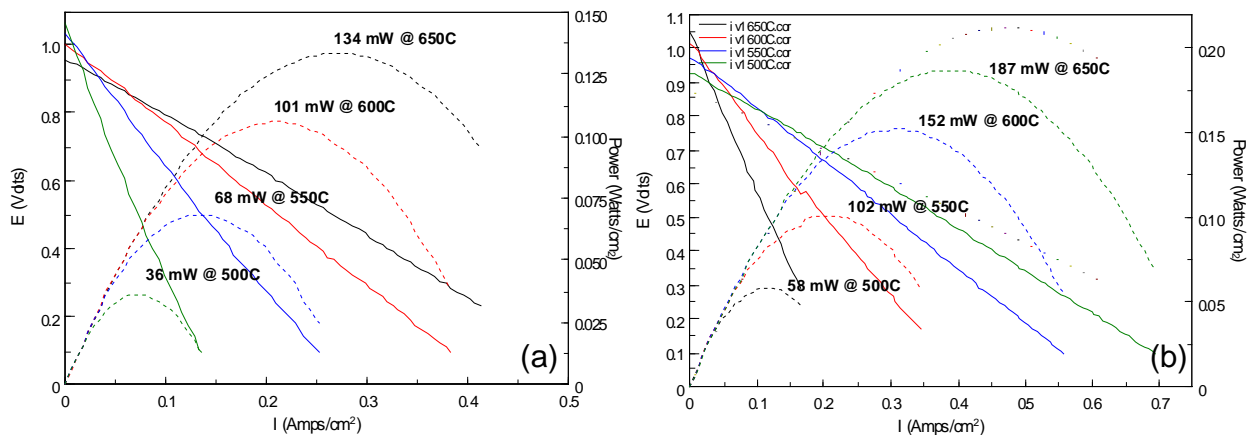


Figure B-10. Effect of ceramabond 1 (a) and ceramabond 2 (b) on the I-V characteristics.

2.2. Long Term Stability

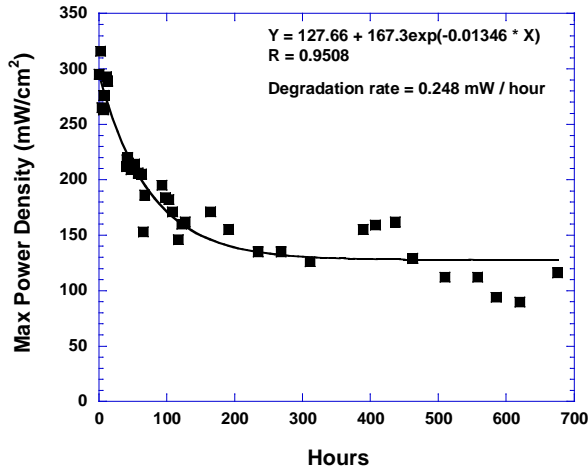


Figure B-11. Maximum power density of a SOFC without AFL for 700 hours at 550 °C.

An earlier tape cast anode supported SOFC without AFL was tested at 550 °C and the initial maximum power density was 316 mW/cm² at 0.41 V. The cell voltage of 0.41 V was maintained potentiostatically and the maximum power densities were monitored for 700 hours at the same temperature. Figure B-11 shows a rapid degradation in cell performance for the first 200 hours of operation followed by stabilization at 130 mW/cm². The total degradation rate of the maximum power density over 700 hours was 0.248 mW/hour.

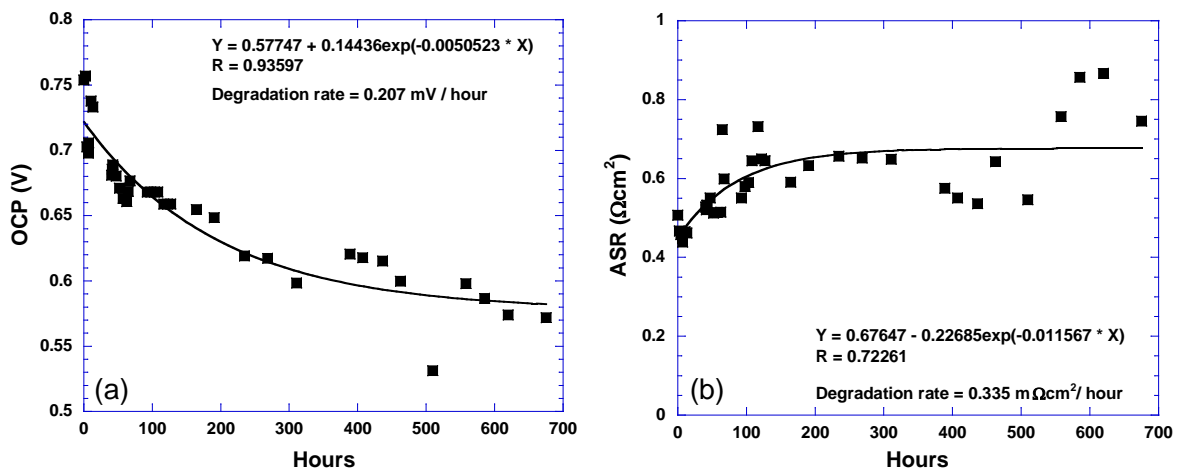


Figure B-12. (a) The OCP values and (b) the ASR values at 0.41 V for 700 hours.

Figure B-12 shows that the main cause of the power degradation was a decrease in OCP. The degradation rates of the OCP and the ASR were 0.207 mV/hour and 0.335 mΩcm²/hour, respectively. However, the OCP values decrease continuously with time while the ASR tends to level off and did not contribute that much to the performance degradation. The decrease in OCP is most likely due to gas leakage. Since this was an early cell before development of the AFL, electrolyte density was poor. So, internal leakage is quite likely resulting in a decrease in OCP with time. In addition, the observed variability in OCP with flow rate confirmed we had external sealing issues. In fact to apply SOFCs developed in this dissertation to practical fields, not only long-term stability but also thermal cycling and red-ox cycling test are necessary, which has neither been discussed nor presented in this dissertation. It is certain that application of AFL and multilayered AFL would improve the stability of the sample, but extensive long-term studies are required to attack all obstacles.

2.3. Critical Flaws

Critical flaws in this section mean unusual spots or region of poor electrolyte quality. Sometimes, this kind of defect can be observed by the naked eye, if it is large enough. This kind of defect can be formed when large agglomerates in the colloidal slurry are not broken. Since agglomerates densify more readily than the rest of the film, cracks form around agglomerates.⁸⁰ Also, dust in the electrolyte green body can cause these defects to form. Critical flaws can be reduced but hardly removed completely because of the limitation of simple colloidal processing. The number of critical flaws increases with the active area of the cell. For example, if we assume the number of critical flaws of current technique is 1/cm², a sample with a 0.5 cm² active area in a button cell has a 50-50 chance of existing in a region with a critical flaw. However, a cell with an active area of 30 cm², for example, should statistically contain 30 critical flaws, and hence a very low probability of containing zero critical flaws.

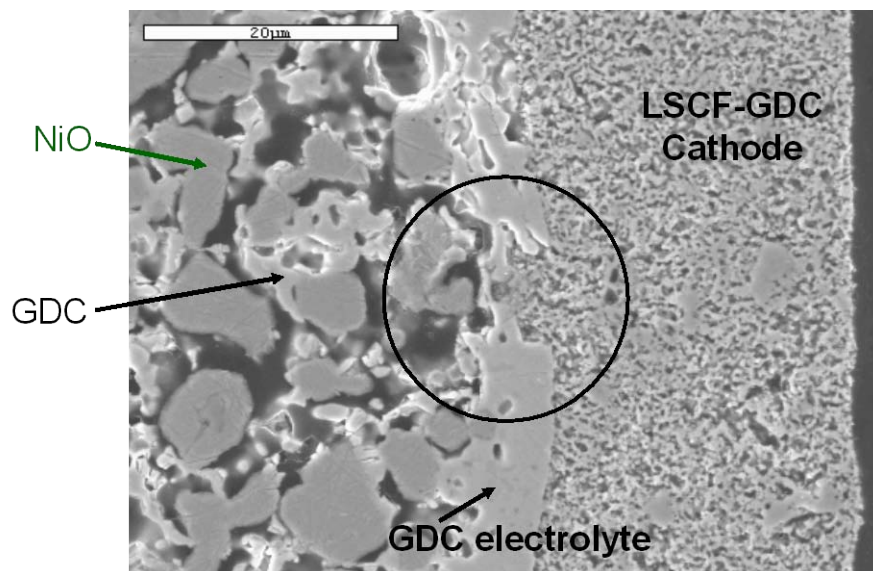


Figure B-13. Unusually porous region in the GDC electrolyte where other area is dense.

A sudden drop in OCP soon after H₂ flow to the anode has been frequently observed during many I-V measurements over the past 4 years, and we believe this is due to critical flaws in the electrolyte. Also, chronic decreases in OCP are in part due to this type of defect. It is believed the critical flaws open up due to chemical expansion from the anode and lose gas tightness. When this happens during the I-V measurement, the sample fails before a day and sometimes even less than 1 hour. A better technique in stabilizing the GDC colloidal slurry is required. No measurements of the isoelectric point of the GDC particles used in this study have been measured and therefore pH of the solution was not optimized accordingly. Currently the addition of 1 wt% of inorganic dispersant to the slurry has been the only way to stabilize the slurry. Additionally, maintaining a clean lab environment is very important during deposition in order to minimize dust exposure to the green body.

LIST OF REFERENCES

- 1 M. Inman, Nature Reports Climate Change, 18 (2009).
- 2 K. Donaldson, P. W. Hadoke, N. A. Boon, W. MacNee, F. R. Cassee, T. Sandström, A. Blomberg, D. E. Newby, and N. L. Mills, Nature Clinical Practice Cardiovascular Medicine **6**, 36 (2008).
- 3 A. Atkinson, S. A. Barnett, R. J. Gorte, J. T. S. Irvine, A. J. Mcevoy, M. Mogensen, S. C. Singhal, and J. Vohs, Nature Materials **3**, 17 (2004).
- 4 N. Minh, General Electric Energy, Hybrid Power Generation Systems in http://www.netl.doe.gov/publications/proceedings/04/seca-wrkshp/seca-wrkshp04.html#Industrial_Teams (2004).
- 5 S. d. Souza, S. J. Visco, and L. C. D. Jonghe, J. electrochem. Soc. **144**, L36 (1997).
- 6 Q. L. Liu, K. A. Khor, and S. H. Chan, J. Power Sources **161**, 123 (2006).
- 7 Z. Shao and S. M. Haile, Nature **431**, 170 (2004).
- 8 E. D. Wachsman, Solid State Ionics **152-253**, 657 (2002).
- 9 Q. L. Liu, K. A. Khor, S. H. Chan, and X. J. Chen, *J. Power Sources* **162**, 1036 (2006).
- 10 C. Torres-Garibay, D. Kovar, and A. Manthiram, *J. Power Sources* **187**, 480 (2009).
- 11 M. D. Gross, J. M. Vohs, and R. J. Gorte, *Journal of The Electrochemical Society* **154**, B694 (2007).
- 12 N. Ai, Z. Lu, J. Tang, K. Chen, X. Huang, and W. Su, *J. Power Sources* **185**, 153 (2008).
- 13 K. F. Chen, X. J. Chen, Z. Lu, N. Ai, X. Q. Huang, and W. H. Su, *Electrochimica Acta* **53**, 7825 (2008).
- 14 N. Ai, Z. Lu, K. F. Chen, X. Q. Huang, X. B. Du, and W. H. Su, *J. Power Sources* **171**, 489 (2007).
- 15 A. A. E. Hassan, N. H. Menzler, G. Blass, and M. E. Ali, *Adv. Eng. Mater.* **4**, 125 (2002).

- 16 Z. R. Wang, J. Q. Qian, S. R. Wang, J. D. Cao, and T. L. Wen, *Solid State Ionics* **179**,
1593 (2008).
- 17 P. Holtappels, C. Sorof, M. C. Verbraeken, S. Rambert, and U. Vogt, *Fuel Cells* **06**, 113
(2006).
- 18 N. T. Hart, N. P. Brandon, M. J. Day, and N. Lapena-Rey, *J. Power Sources* **106**, 42
(2002).
- 19 Y. Liu, C. Compson, and M. L. Liu, *J. Power Sources* **138**, 194 (2004).
- 20 S. W. Zha, Y. L. Zhang, and M. L. Liu, *Solid State Ionics* **176**, 25 (2005).
- 21 M. Ni, M. K. H. Leung, and D. Y. C. Leung, *Chem. Eng. Technol.* **30**, 587 (2007).
- 22 X. Xu, C. Xia, G. Xiao, and D. Peng, *Solid State Ionics* **176**, 1513 (2005).
- 23 B. C. H. Steele, *Solid State Ionics* **129**, 95 (2000).
- 24 B. C. H. Steele and A. Heinzl, *Nature* **414**, 345 (1990).
- 25 S. M. Haile, *Acta Materialia* **51**, 5981 (2003).
- 26 B. C. H. Steele, *Nature* **400**, 12 (1999).
- 27 B. C. H. Steele, *Solid State Ionics* **75**, 157 (1995).
- 28 D. Jung, K. Duncan, and E. D. Wachsman, submitted to *Solid State Ionics*.
- 29 S. Omar, E. D. Wachsman, and J. C. Nino, *Applied Physics Letters* **91**, 144106 (2007).
- 30 P. J. Gellings and H. J. M. Bouwmeester, *The CRC handbook of Solid state
electrochemistry* (CRC press, Inc., 1997).
- 31 J. S. Ahn, M. A. Camaratta, D. Pergolesi, K. T. Lee, H. Yoon, B. W. Lee, D. W. Jung, E.
Traversa, and E. D. Wachsman, Submitted to *J. Electrochem. Soc.* (2009).
- 32 J. Nowotny, T. Bak, M. K. Nowotny, and C. C. Sorrell, *Advances in Applied Ceramics*
104, 154 (2005).

- 33 M. Mogensen and T. Lindegaard, 1993 (The electrochemical society), p. 484.
- 34 T. Kenjo, S. Osawa, and K. Fujikawa, *J. Electrochem. Soc.* **138**, 349 (1991).
- 35 E. P. Murray and S. A. Barnett, *Solid State Ionics* **143**, 265 (2001).
- 36 S. Omar, E. D. Wachsman, and J. C. Nino, *Solid State Ionics* **178**, 1890 (2008).
- 37 S. Omar, E. D. Wachsman, and J. C. Nino, *Solid State Ionics* **177**, 3199 (2006).
- 38 K. Eguchi, T. Setoguchi, T. Inoue, and H. Arai, *Solid State Ionics* **52**, 165 (1992).
- 39 B. C. H. Steele, *Solid State Ionics* **86-88**, 1223 (1996).
- 40 E. D. Wachsman, G. R. Ball, N. Jiang, and D. A. Stevenson, *Solid State Ionics* **52**, 213 (1992).
- 41 E. D. Wachsman, P. Jayaweera, N. Jiang, D. M. Lowe, and B. G. Pound, *J. Electrochem. Soc.* **144**, 233 (1997).
- 42 J. Y. Park and E. D. Wachsman, *Ionics* **11-2**, 15 (2006).
- 43 J. Y. Park and E. D. Wachsman, *J. Am. Ceram. Soc.* **88**, 2402 (2005).
- 44 B. A. Boukamp, K. J. d. Vries, and A. J. Burggraaf, *Non-Stoichiometric Compounds: Surfaces, Grain Boundaries and Structural Defects* (1989).
- 45 J. C. Boivin, C. Pirovano, G. Nowogrocki, G. Mairesse, P. Labrune, and G. Lagrange, *Solid State Ionics* **113-115**, 639 (1998).
- 46 B. A. Boukamp, *Solid State Ionics* **136-137**, 75 (2000).
- 47 M. Dumelie, G. Nowogrocki, and J. C. Boivin, *Solid State Ionics* **28-30**, 524 (1988).
- 48 I. C. Vinke, K. Seshan, B. A. Boukamp, K. J. d. Vries, and A. J. Burggraaf, *Solid State Ionics* **34**, 235 (1989).
- 49 M. A. Camaratta and E. D. Wachsman, *Solid State Ionics* **178**, 1411 (2007).
- 50 M. A. Camaratta and E. D. Wachsman, *Solid State Ionics* **178**, 1242 (2007).

- 51 A. Jaiswal and E. D. Wachsman, *J. Electrochem. Soc.* **152**, A787 (2005).
- 52 M. A. Camaratta and E. D. Wachsman, *J. Electrochem. Soc.* **155**, B135 (2008).
- 53 Y. J. Leng, S. H. Chan, and K. A. Khor, p. 1110.
- 54 J. S. Ahn, H. Yoon, and E. D. Wachsman, *ECS Trans.* **11**, 99 (2008).
- 55 J. S. Ahn, H. Yoon, K. T. Lee, M. A. Camaratta, and E. D. Wachsman, Submitted to *Fuel Cells* (2009).
- 56 J. Larminie and A. Dicks, *Fuel Cell Systems Explained* (Wiley).
- 57 D. R. Gaskell, *Introduction to the Thermodynamics of Materials* (Taylor & Francis Books, Inc., 2003).
- 58 J. Newman and K. E. Thomas-Alyea, *Electrochemical systems*, 3rd Ed. ed. (Wiley, New Jersey, 2004).
- 59 A. J. Bard and L. R. Faulkner, *Electrochemical Methods. Fundamentals and Applications*, 2nd Ed. ed. (Wiley, New York, 2001).
- 60 S. H. Chan, K. A. Khor, and Z. T. Xia, *J. Power Sources* **93**, 130 (2001).
- 61 H. Zhu and R. J. Kee, *J. Power Sources* **117**, 61 (2003).
- 62 K. L. Duncan and s. E. D. Wachsman Submitted to *J. Electrochem. Soc.*
- 63 J.-W. Kim, A. V. Virkar, -. Z. F. K, K. Mehta, and S. C. Singhal, *J. Electrochem. Soc.* **146**, 69 (1999).
- 64 K. J. Yoon, P. Zink, S. Gopalan, and U. B. Pal, *J. Power Sources* **172**, 39 (2007).
- 65 J. C. Amphlett, R. M. Baumert, R. F. Mann, B. A. Peppley, P. R. Roberge, and T. J. Harris, *J. Electrochem. Soc.* **142**, 1 (1995).
- 66 J. C. Amphlett, R. M. Baumert, R. F. Mann, B. A. Peppley, P. R. Roberge, and T. J. Harris, *J. Electrochem. Soc.* **142**, 9 (1995).

- 67 J. S. Ahn, S. Omar, H. Yoon, J. C. Nino, and E. D. Wachsman, submitted to *J. Power Sources* (2008).
- 68 S. B. Adler, *J. Electrochem. Soc.* **149**, E166 (2002).
- 69 J. Winkler, P. V. Hendriksen, N. Bonanos, and M. Mogensen, *J. Electrochem. Soc.* **145**, 1184.
- 70 A. Pramanick, S. Omar, J. C. Nino, and J. L. Jones, *J. App. Crystall.*, in Press (2009).
- 71 M. Godickemeier, K. Sasaki, L. J. Gauckler, and I. Riess, *Solid State Ionics* **86-8**, 691 (1996).
- 72 S. Zha, A. Moore, H. Abernathy, and M. Liu, *J. Electrochem. Soc.* **151**, A1128 (2004).
- 73 P. Shuk, H. D. Wiemhofer, U. Guth, W. Gopel, and M. Greenblatt, *Solid State Ionics* **89**, 179 (1996).
- 74 H. Ghezal-Ayagh, in *9th Annual SECA Workshop* (Pittsburgh, PA, 2008).
- 75 M. Yokoo, Y. Tabata, Y. Yoshida, H. Orui, K. Hayashi, Y. Nozaki, K. Nozawa, and H. Arai, *J. Power Sources* **184**, 84 (2008).
- 76 M. Lang, C. Auer, A. Eismann, P. Szabo, and Norbert Wagner, *Electrochimica Acta* **53**, 7509 (2008).
- 77 H. Y. Jung, S.-H. Choi, H. Kim, J.-W. Son, J. Kim, H.-W. Lee, and J.-H. Lee, *J. Power Sources* **159**, 478 (2006).
- 78 J. M. Rhodes, Thesis, University of Florida, 2005.
- 79 S. R. Bishop, K. L. Duncan, and E. D. Wachsman, *Electrochim. Acta* **54**, 1436 (2009).
- 80 C. Lu, W. L. Worrell, C. Wang, S. Park, H. Kim, J. M. Vohs, and R. J. Gorte, *Solid State Ionics* **152-153**, 393 (2002).

BIOGRAPHICAL SKETCH

Jin Soo Ahn was born in Seoul, Korea in 1976. After graduating from Un-nam High School in Seoul, Korea, in 1995, He studied in the department of ceramic engineering at Yonsei University in Korea. During his studies, he was enlisted in the Republic of Korea Army (ROKA) as a computer in a mortar team in 1996, and finished military service in 1998. Then, he returned to the Yonsei University and received his Bachelor of Science degree in ceramic engineering, in February 2002. He entered the Michigan State University as a graduate student in August 2002, and received the Master of Science in materials science and engineering, in summer 2004. Finally he entered the University of Florida in 2004 and joined in Dr. Wachsman's group, and received his Ph.D. from the University of Florida in the spring of 2009. Since then, he has been working on my graduate research in the field of "solid-state ionics", with a specialty in "fabrication and characterization of SOFCs".